Multi-Scale Dynamics and Rheology of Mantle Convection with Plates

Thesis by

Laura Alisic

In Partial Fulfillment of the Requirements

for the Degree of

Doctor of Philosophy

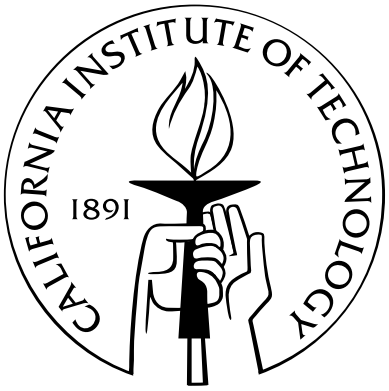

California Institute of Technology

Pasadena, California

2012

(Defended April 16$^{\text{th}}$, 2012)

"I do not know what I may appear to the world,

but to myself I seem to have been only like a boy playing on the sea-shore,

and diverting myself in now and then finding a smoother pebble or a prettier shell

than ordinary, whilst the great ocean of truth lay all undiscovered before me."

— *Sir Isaac Newton*

Acknowledgements

16+ million compute hours. 122,880 compute cores. 7.2 terabytes of stored data. 6 notebooks. 5.5 years of work. These are some numbers to illustrate the effort that went into this thesis. But the real effort came from my PhD advisor, collaborators, and colleagues.

First of all, I would like to thank my advisor, Prof. Michael Gurnis, who has been a great source of inspiration and encouragement. Over the past 6 years, he has patiently taken the time to teach me how to tackle a scientific problem, how to think about and analyze numerical modeling results, and how to convey these results to peers. The latter should, after all, be the ultimate goal of a scientist. Second, I would like to thank the members of my Thesis Advisory Committee and Thesis Examination Committee for their insights and ideas: Professors Rob Clayton, Jennifer Jackson, Mark Simons, and Jean-Philippe Avouac.

This work would not have been possible without the vision, expertise, and hard work of several collaborators. The group led by Prof. Omar Ghattas in the Institute for Computational Engineering and Sciences at the University of Texas at Austin leads the pack in developing new-generation computational tools and algorithms. With the development and benchmarking of the mantle convection code `Rhea`, I have learned a tremendous amount about computational science and software development from, in particular, Georg Stadler, Carsten Burstedde, and Lucas Wilcox. The most recent component of this thesis is the modeling of past plate motions in close collaboration with Prof. Dietmar Müller's EarthByte group at the University of Sydney,

especially Kara Matthews, Nico Flament, and Maria Seton, and with Dan Bower at Caltech.

Throughout my PhD, many fruitful and stimulating scientific discussions with Dan Bower, Alejandro Soto, Erin Burkett, and Francisco Ortega have helped me more than I can say. Additionally, the technical and practical support from various people has been essential: Donna Mireles and Viola Carter in the Seismolab; Mike Black and Dian Buchness in the Department of Geological and Planetary Sciences at Caltech; and the support staff at the Texas Advanced Computing Center.

Last, and definitely not least, I would like to thank my family: my parents and my sister Eva. From a young age onward, they encouraged me to learn, explore, and be the best I can. And albeit at a distance during the past 6 years, they have provided me with an endless supply of support and a listening ear, and always showed great interest in what I was doing so far away. They give me more than anyone could ask for. A heartfelt Thank you, with a capital T.

Abstract

Fundamental issues in our understanding of plate and mantle dynamics remain unresolved, including the rheology and state of stress of plates and slabs; the coupling between plates, slabs and mantle; the small-scale dynamics in subduction zones; the flow around slabs; and the cause of rapid changes in plate motions. To address these questions, models of global mantle flow with plates are computed using adaptive finite elements, and compared to a variety of observational constraints. These dynamically consistent instantaneous models include a composite rheology with yielding, and incorporate details of the thermal buoyancy field. Around plate boundaries, the local mesh size is 1 km, which allows us to study highly detailed features in a globally consistent framework. Models that best fit plateness criteria and plate motion data have strong slabs with high viscosities around 10^{24} Pa s, and stresses of $\sim$ 100 MPa. We find a strong dependence of global plate motions, trench rollback, net rotation, plateness, and strain rate on the stress exponent in the nonlinear viscosity; the yield stress is found to be important only if it is smaller than the ambient convective stress. Due to strong coupling between plates, slabs, and the surrounding mantle, the presence of lower mantle anomalies affect plate motions. The flow in and around slabs, microplate motion, and trench rollback are intimately linked to the amount of yielding in the subducting slab hinge, slab morphology, and the presence of high viscosity structures in the lower mantle beneath the slab. The lateral flow around slabs is generally trench-perpendicular, induced by the strongly

coupled downward motion of the subducting slabs, and therefore our models do not account for the trench-parallel flow inferred from shear-wave splitting analysis. Flow models before and after the plate reorganization around 50 Ma are not able to reproduce the rapid change in Pacific plate motion from northwest to west that is associated with the bend in the Hawaiian-Emperor chain, despite a nonlinear rheology and the incorporation of detailed reconstructed paleo plate boundaries and age grids. In these models at 55 and 45 Ma, slab age is an important factor in the slab pull, determining the coupling between plates and slabs and between upper and lower mantle sections of slabs. The overall dynamics appear to be dominated by the characteristics of slab remnants in the lower mantle. Subducting slabs affect lateral flow in the upper mantle on a much smaller scale, and therefore we conclude that it is unlikely that the slabs in the western Pacific are responsible for the slowing of sub-Pacific flow after the initiation of their subduction around 50 Ma.

Contents

List of Figures

List of Tables

Chapter 1

Introduction

Portions originally published in:

Stadler, G., Gurnis, M., Burstedde, C., Wilcox, L. C., Alisic, L., & Ghattas, O. (2010). The dynamics of plate tectonics and mantle flow: From local to global scales. *Science*, 329, 1033–1038.

1.1 Modeling Mantle Convection With Plates

Mantle convection and associated plate tectonics are principal controls on the thermal and geological evolution of the Earth. These processes are central to our understanding of the origin and evolution of tectonic deformation, the evolution of the thermal and compositional states of the mantle, and ultimately the evolution of the Earth as a whole. Plate creation and motion largely governs the loss of heat from the solid Earth (*Davies*, 1999), and the strength of plates may control the energy dissipation and hence heat loss over geological time (*Conrad and Hager*, 1999b). However, despite the central importance of plate dynamics, there are fundamental uncertainties on the forces resisting and driving plate motions.

Although there is consensus that the 1–10 cm/yr motion of plates is driven largely by the thermal buoyancy within subducted slabs (*Hager and O'Connell*, 1981) and perturbed by upper mantle solid-solid phase transitions (*Billen*, 2008) and cooling of oceanic lithosphere from ridge to trench, the importance of the aseismic extension of slabs within the lower mantle

(*Lithgow-Bertelloni and Richards*, 1998) remains unresolved. The strength of subducted slabs likely regulates the velocity of plate tectonics. This strength is usually described by viscosity, where yielding (defined by a yield stress) and other weakening processes can limit the viscosity locally. The vast majority of available negative buoyancy driving plates is within the transition zone and lower mantle, and if slabs are strong, then this force can be coupled directly into the edges of oceanic plates at trenches (*Zhong and Gurnis*, 1995). However, if the oceanic lithosphere is strong during initial subduction as it bends below the trench, then the dissipation within the narrow high-viscosity slab could limit plate velocity (*Conrad and Hager*, 1999a). Although the importance of plate margin and slab strength has been studied in two- and three-dimensional Cartesian models aimed at understanding the physics of subduction (*Zhong et al.*, 1998; *Cizkova et al.*, 2002; *Schellart*, 2004; *Faccenna et al.*, 2007; *Billen*, 2008) and in limited regional models that assimilate observed structure (*Billen et al.*, 2003; *Jadamec and Billen*, 2010), the incorporation of realistic rheologies into models with narrow slabs and plate boundaries has remained an elusive goal of global geodynamics. Whether slabs are weak or strong remains unresolved; previous numerical modeling efforts used slab and plate viscosities varying from 10^{21} to 10^{26} Pa s (*Billen*, 2008).

With the incorporation of strong slabs and realistic treatment of plate margins, the ability to observationally constrain models would increase substantially. Observations constraining the deformation of slabs will prove useful in global models: examples include the strain rate and state of stress within slabs from deep focus earthquakes (*Isacks and Molnar*, 1971) and the kinematics of slab rollback in subduction zones with present-day back-arc extension (*Dewey*, 1980). Large fractions of the Earth's surface ($\sim$ 15% globally) do not follow a rigid plate tectonic model but undergo deformation close to trenches and further from plate margins (*Gordon and Stein*, 1992). Some oceanic plates are deforming diffusively within their interiors, espe-

cially the Indo-Australian plates (*Gordon et al.*, 1998). The rich array of geodetic, topographic, gravitational, and seismic observations from local to regional scales constrains these deformations and could validate global dynamics if we are able to capture the commensurate scales in models with realistic rheologies.

Arguably, the biggest limitation on current progress is not observational, but computational: solution of models that incorporate realistic rheologies and local geological structure has been prohibitive historically, due to limitations in numerical methods and computational resources. Taken as a whole, current generation models poorly exploit the observational constraints on present-day deformation. For example, models of plate motion do not use observations of deformation at plate margins and interiors because numerical simulation of global mantle convection down to the scale of faulted plate boundaries has been intractable due to the wide range of time and length scales involved. Using adaptive mesh refinement (AMR) on highly parallel computers has allowed us to incorporate realistic rheologies and fine-scale observations in global mantle convection simulations, and in turn reach fundamental conclusions on the forces driving the plates and the energy dissipation throughout the solid earth by intimately linking these models to observations.

1.2 Parallel Adaptive Mesh Refinement

Capturing the large viscosity variations occurring at plate boundaries requires a mesh with about 1 km local resolution. A spacing of up to 1 km is needed in order to have a narrow weak shear zone of a few kilometers, as the development of weak shear zones of width Δw during plate failure depends on the mesh spacing Δd: $\Delta w \sim 2\Delta d$ to $4\Delta d$ (*Gurnis et al.*, 2004). Such a small mesh spacing also allows for a smooth geometry in the bending part

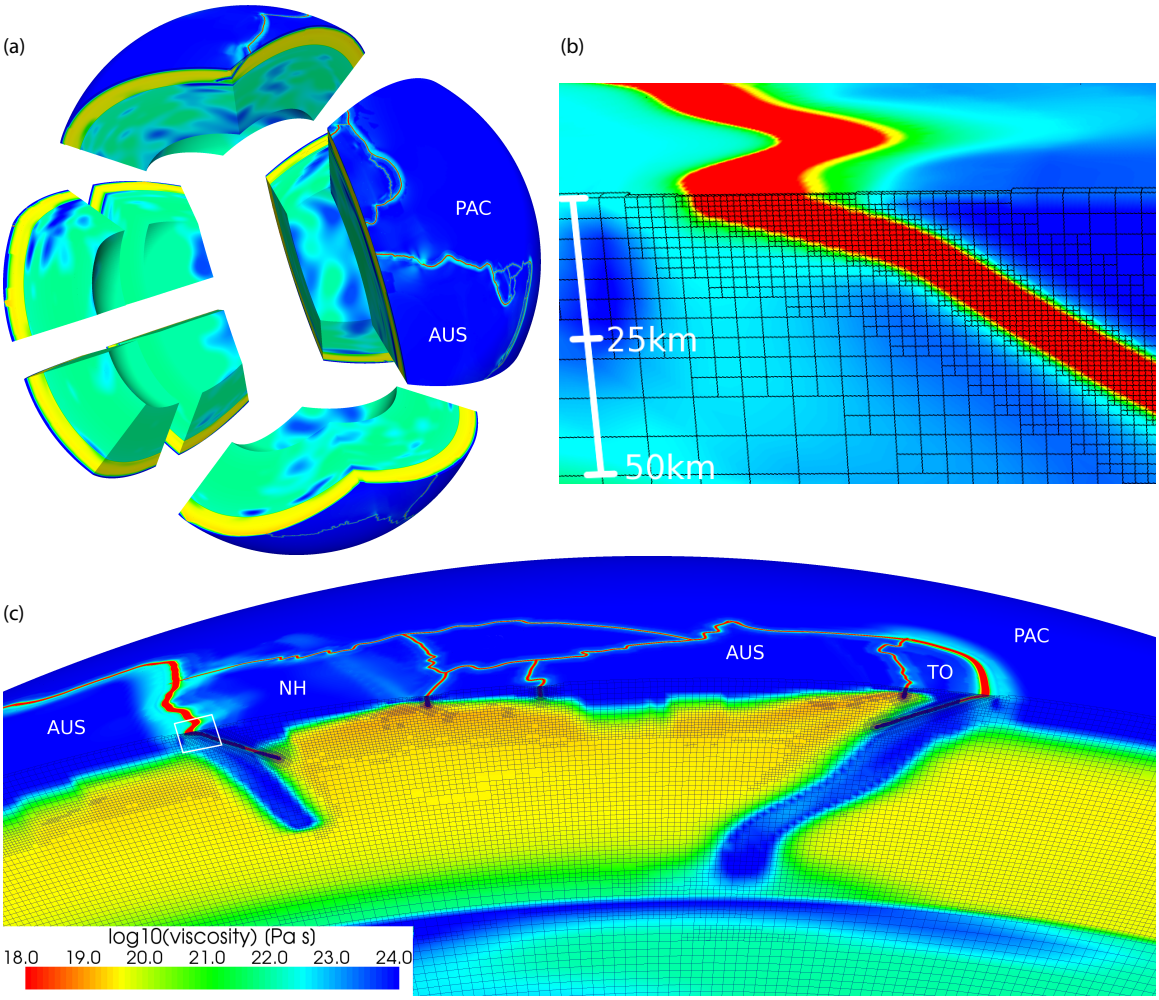

Figure 1.1. (a) Splitting of the Earth's mantle into 24 warped cubes. Each cube is identified with an adaptively subdivided octree whose octants are the mesh elements. The effective viscosity field is shown; the narrow low-viscosity zones corresponding to plate boundaries are seen as red lines on the Earth's surface. (b) Zoom into the hinge zone of the Australian plate (as indicated by the box in (c)) showing the adaptively refined mesh with a finest resolution of about 1 km. (c) Cross-section showing the refinement that occurs both around plate boundaries and dynamically in response to the nonlinear viscosity, with plastic failure in the region from the New Hebrides to Tonga in the southwest Pacific. Plates labeled: Australian (AUS), New Hebrides (NH), Tonga (TO), and Pacific (PAC).

of the subducting plate, and avoids a step pattern in the plate boundary that could affect the deformation pattern within the slab hinge. Furthermore, the gradient in viscosity permitted across an element is limited for reasons of numerical stability, and therefore refinement down to a (sub)kilometer scale is required to resolve the many orders of magnitude viscosity gradient between weak plate boundaries and the adjacent stiff plates. A globally uniform mesh with 1 km spacing would require $\sim 10^{12}$ mesh elements, beyond both the capacity of contemporary supercomputers and the reach of numerical solution methods. With AMR, we achieve this high resolution near plate boundaries, while using a coarser 5 km resolution within thermal boundary layers (including the oceanic lithosphere) and 15–50 km resolution for the rest of the mantle, thereby saving a factor of over 10^3 compared to a uniform mesh. The resulting reduction in problem size to a few hundred million elements is critical to making the simulations tractable on petascale supercomputers.

However, scaling AMR to thousands of processors is a challenge (*Diachin et al.*, 2006). Adaptively refined meshes entail irregular and dynamically changing topological mesh relations, while solution on parallel computers makes it necessary to store just a small part of the mesh on each processor. These mesh partitions must be changed after each refinement and coarsening step to ensure that the computational load on individual processors is balanced. Scalable algorithms for these mesh operations as well as numerical solution of the mantle flow equations have been developed in the AMR finite element framework `p4est` (*Burstedde et al.*, 2008a, 2009a,b). These parallel AMR algorithms are based on a forest of adaptive octrees, in which multiple warped cubes are joined to represent general geometries. The spherical shell used to represent the mantle is composed of 24 cubes (Figure 1.1). Each cube is adaptively subdivided using an octree data structure, which allows for fast algorithms to manage the mesh adaptivity and to construct the mesh connectivity information required in numerical simula-

tions. These algorithms, which have scaled to over 200,000 processor cores, are applicable to a broad spectrum of multiscale scientific and engineering problems that require high resolution in localized (possibly dynamically evolving) regions, such as near fronts, discontinuities, material interfaces, reentrant corners, and boundary and interior layers.

1.3 Thesis Overview

In this thesis, the described developments in parallel AMR techniques are used in dynamic global mantle convection computations with the application code `Rhea` to address the following questions:

1. **What is the rheology of plates, slabs, and the surrounding mantle?** How strong are plates and slabs? How weak are plate boundaries? How much weakening occurs in plates that are bending into subduction zones?

2. **What is the coupling between plates, slabs, and the surrounding mantle?** Are slabs able to act as stress guides, i.e., are stresses fully transmitted between plates and slabs? How much stress is transmitted to the surrounding mantle? Where does dissipation of energy take place?

3. **What is the importance of lower mantle structure for plate tectonics?** Does the presence of lateral viscosity variations in the lower mantle affect plate motions? Do cold, high-viscosity structures attached to slabs speed up or slow down subduction?

4. **Can we predict regional dynamics in global convection models?** Can we model the various observed behaviors of trenches, ranging between retreating (rolling back), stationary, and advancing? Can we correctly predict microplate motions? What are the

characteristics of flow around subducting slabs, what is the relative importance of trench-perpendicular and trench-parallel flow?

5. **What is the effect of regional geometry versus rheology on modeled quantities?** Are velocities, viscosity, strain rate, and state of stress in slabs governed primarily by the implemented rheology law, or by the morphology of plate boundaries and slabs, or both?

6. **What caused rapid change in plate motions in the geologic past (i.e., plate reorganizations)?** Could a change in mantle flow pattern or a change in plate boundary force be responsible; i.e., is this a mantle-driven or a plate-driven process? Can we predict such changes in plate motions with dynamic flow models?

In Chapter 2, we investigate how stress drop determined for large-magnitude deep earthquakes and strain rates in subducting slabs can constrain the strength of these slabs (question 1). We focus on two regions, containing the M_W 8.3 Bolivia and M_W 7.6 Tonga events in 1994, and determine for which yield stresses the minimum stress from stress drop estimates and minimum strain rate estimates from seismicity are satisfied.

Chapter 3 further explores this concept by testing the global models with an ensemble of model constraints, both globally and regionally, while examining a significantly larger model parameter space for the yield stress, stress exponent, and the scaling factor used to convert velocity anomalies in seismic tomography to temperature. The constraints include fit to plate motions, plateness, net rotation, the state of stress and strain rate in plates and slabs, as well as microplate motion and trench rollback. We address questions concerning plate and slab strength, coupling between the various parts of the domain including the effect of lower mantle structure on plate motions, and study slab dynamics and trench rollback in detail (questions

1–5).

We then move from the present-day Earth to its past. In Chapter 4, we address the causes and effects of the plate reorganization occurring around 50 Ma (question 6). To this end, we compute instantaneous models just before and after the reorganization using reconstructed plate boundaries and age grids, and study changes in velocities, state of stress, and strain rates at the surface as well as in the interior of the mantle. Reconstructed plate velocities form the major constraint on these models. The rheology determined in the present-day models presented in the previous chapters are used. This work is still ongoing, and is a close collaboration with Kara Matthews and the EarthByte group at the University of Sydney. The Sydney group is primarily responsible for the plate reconstructions, whereas the setup and computation of the dynamic flow models as well as their analysis is my contribution.

In Chapter 5, the findings in this thesis are summarized and put into context of our current understanding of mantle dynamics and plate tectonics, revisiting the set of questions posed in this chapter, and possible future directions in this work are presented.

The computational methods used in `Rhea` and its library `p4est` are described in detail in the Appendix, along with a suite of code benchmarks. This chapter is the result of close collaboration with Georg Stadler at the Institute for Computational Engineering and Sciences (ICES), University of Texas in Austin, and Carsten Burstedde (previously at ICES, now at Universität Bonn), who have been the principal driving force behind the development of `p4est` and `Rhea`. My responsibility in this joint effort has been designing, setting up, running, and analyzing the majority of the benchmark experiments, with the exception of the manufactured solution and the mid-oceanic ridge example.

Chapter 2

Slab Stress and Strain Rate as Constraints on Global Mantle Flow

Originally published in:

Alisic, L., Gurnis, M., Stadler, G., Burstedde, C., Wilcox, L. C., & Ghattas, O. (2010). Slab stress and strain rate as constraints on global mantle flow. *Geophysical Research Letters*, 37, L22308.

2.1 Abstract

Dynamically consistent global models of mantle convection with plates are developed that are consistent with detailed constraints on the state of stress and strain rate from deep focus earthquakes. Models that best fit plateness criteria and plate motion data have strong slabs that have high stresses. The regions containing the M_W 8.3 Bolivia and M_W 7.6 Tonga 1994 events are considered in detail. Modeled stress orientations match stress patterns from earthquake focal mechanisms. A yield stress of at least 100 MPa is required to fit plate motions and matches the minimum stress requirement obtained from the stress drop for the Bolivia 1994 deep focus event. The minimum strain rate determined from seismic moment release in the Tonga slab provides an upper limit of $\sim$ 200 MPa on the strength in the slab.

2.2 Introduction

An essential component of mantle convection models with plates is the strength of the subducting slabs and their influence on the dynamics of the convective system. The stronger slabs are, the more they could exert an important force on plate motions, acting as stress guides. Regional studies using the geoid concluded that the viscosity in the slabs is 100 to 1000 times higher than in the surrounding mantle (*Moresi and Gurnis*, 1996), and could not exceed 10^{23} Pa s in order to fit geoid highs over subducted slabs (*Billen et al.*, 2003). Also, studies of plate bending indicate that the plate viscosity must be between 50 and 200 times the mantle viscosity in order to fit dissipation constraints (*Conrad and Hager*, 1999a). Torque balance models of the Pacific and Australian plate suggested that the best fit to observed rotation poles was obtained with an effective lithosphere viscosity of 6×10^{22} Pa s (*Buffett and Rowley*, 2006). In contrast, with time-dependent generic models of slab dynamics, strong slabs are inferred (*Billen and Hirth*, 2007), in concordance with experimentally found temperature dependence of the effective viscosity of olivine (*Hirth and Kohlstedt*, 2003). Using a composite rheology with a nonlinear component (*Billen and Hirth*, 2007) allows for localization of strain, and hence localized strain weakening in the hinge of a subducting slab. In this way, slabs can be strong and still subduct with relative ease. Global models addressing slab pull show that strong slabs provide the best fit to observed plate motions, exerting slab pull forces that account for approximately half of the total driving forces on plates (*Conrad and Lithgow-Bertelloni*, 2002).

The state of stress indicated by earthquake focal mechanisms and their stress drop, in selected cases, provide additional constraints on the strength of slabs. The stress drop estimates for large moment magnitude deep earthquakes form a lower limit of the stress that the slab must sustain. Here the state of stress of slabs is studied in globally consistent dynamic models

of mantle convection with plates, while incorporating a composite rheology. We address two study areas, covering the locations of the Bolivia, M_W 8.3, 1994 and the Tonga, M_W 7.6, 1994 earthquakes. These earthquakes were chosen because they putatively represent end member types of deep earthquakes. The Bolivia earthquake experienced a large stress drop of 114 MPa, a rupture propagation of only 1 km/s, few aftershocks, and was located in a region with scarce seismicity (*Kanamori et al.*, 1998). In contrast, the Tonga earthquake had a low stress drop ($\sim$ 1.6 MPa), fast rupture propagation of 3–4 km/s, and many aftershocks in a region with abundant seismicity (*Wiens and McGuire*, 1995).

2.3 Model Setup and Solution

The dynamics of instantaneous mantle convection are governed by the equations of conservation of mass and momentum. Under the Boussinesq approximation for a mantle with uniform composition and the assumption that the mantle deforms viscously, the nondimensionalized form of these equations is (e.g., *Schubert et al.* (2001)):

$$\nabla \cdot \mathbf{u} = \mathbf{0}, \tag{2.1}$$

$$\nabla \mathbf{p} - \nabla \cdot \left[\eta(T, \mathbf{u}) \left(\nabla \mathbf{u} + \nabla \mathbf{u}^{\top}\right)\right] = \mathrm{Ra}\, T\, \mathbf{e}_r, \tag{2.2}$$

where $\mathbf{u}$, $\mathbf{p}$, η, and T are the velocity, pressure, viscosity, and temperature, respectively; $\mathbf{e}_r$ is the unit vector in the radial direction. Ra is the Rayleigh number, $\mathrm{Ra} = \alpha\rho_0 g \Delta T D^3/(\kappa\eta_0)$, where α, ρ_0, η_0, and κ are the reference coefficients of thermal expansion, density, viscosity, and thermal diffusivity (see Table 3.1). ΔT is the temperature difference across a mantle with thickness D, and g is the gravitational acceleration.

We solve these equations with finite elements using a code (`Rhea`) that exploits Adaptive Mesh Refinement (AMR) (*Burstedde et al.*, 2008a). Rhea is a new generation mantle convection code, using forest-of-octree-based adaptive meshes. With `Rhea`'s adaptive capabilities we create local resolution down to $\sim$ 1 km around plate boundaries, while keeping the mesh at a much coarser resolution away from small features. The global models in this study have approximately 200 million elements, a reduction of a factor $\sim$ 5000 compared to a uniform mesh of the same high resolution (*Stadler et al.*, 2010).

A composite formulation of Newtonian (diffusion creep) and non-Newtonian (dislocation creep) rheology is implemented along with yielding. Plate boundaries are modeled as narrow weak zones with a defined viscosity reduction of several orders of magnitude. A generalized viscosity law for the Earth's mantle is used:

$$\eta = \Gamma(\mathbf{x}) \left(\frac{d^p}{A \, {C_{OH}}^r} \right)^{\frac{1}{n}} \dot{\varepsilon}_{\mathrm{II}}^{\frac{1-n}{n}} \exp\left(\frac{E_a + PV_a}{nRT} \right), \tag{2.3}$$

where η is viscosity in Pa s, d grain size in μm, C_{OH} water content in parts per million of silicon, n the stress exponent, and $\dot{\varepsilon}_{\mathrm{II}}$ the second invariant of the strain rate tensor in s^{-1}. E_a is the activation energy in J/mol, P lithostatic pressure in Pa, V_a activation volume in m^3/mol, R the gas constant, and T the temperature in K. $\Gamma(\mathbf{x})$ is a reduction factor used to define weak zones, and is set to between 10^{-5} and 5×10^{-3} in plate boundaries and to 1 elsewhere. The parameters A, n, r, and p are determined experimentally (*Hirth and Kohlstedt*, 2003). The composite viscosity (*Billen and Hirth*, 2007) is obtained by combining diffusion creep (η_{df}) and dislocation creep (η_{ds}) using a harmonic mean. Then, a yield criterion with yield strength

σ_y is imposed to obtain an effective viscosity:

$$\eta_{\text{comp}} = \frac{\eta_{df}\eta_{ds}}{\eta_{df} + \eta_{ds}}, \tag{2.4}$$

$$\eta_{\text{eff}} = \min\left(\frac{\sigma_y}{\dot{\varepsilon}_{\text{II}}}\ ,\ \eta_{\text{comp}}\right). \tag{2.5}$$

The yielding law is only applied if the local temperature is lower than the yield temperature T_y. See Table 3.2 for a summary of the parameter values used in the presented models.

Since plate velocities and "plateness" are outcomes, both the full buoyancy field and plate boundary details at a fine scale must be incorporated. The global models are constructed with oceanic plate ages (*Müller et al.*, 2008), a thermal model containing slabs in the upper mantle, and tomography in the lower mantle (*Ritsema et al.*, 2004). Current tomography resolves slabs in the upper mantle poorly, as mantle wedges and slabs typically blur together. However, resolving the slabs as high-viscosity stress guides is critical for correctly predicting plate motions (e.g., *Zhong et al.* (1998)). In order to maximize the slab sharpness, the upper mantle structure was created with slab contours from seismicity (*Gudmundsson and Sambridge*, 1998).

2.4 Results

Computed models predict velocity, viscosity, strain rate, stress magnitude, orientation of the stress axes, and energy dissipation. The models are tested by assessing the plateness of the surface velocity field, and its misfit with inferred surface velocities. The current best model has a yield stress of 100 MPa and stress exponent of 3.0 (*Stadler et al.*, 2010), with deformation highly localized around plate boundaries. Plate interiors and slabs have a viscosity of $\sim 10^{24}$ Pa s. The hinge of subducting plates yields, causing the viscosity in the hinge to drop to ~ 5

$\times 10^{22}$ to 10^{23} Pa s, consistent with estimates of *Billen et al*. (2003) and *Wu et al*. (2008). This global model allows us to study the local state of stress in a globally consistent framework, including Bolivia and Tonga.

First, we consider the region containing the 1994 M_W 8.3 Bolivia event (647 km depth), where Nazca subducts under the South-American plate at $\sim$ 8 cm/year (*Bird*, 2003). High strain rates are found exclusively in the trench, indicating highly localized deformation at the plate boundaries (Figure 2.1a). The Bolivia 1994 earthquake experienced a minimum frictional stress of 55 MPa and a static stress drop of 114 MPa (*Kanamori et al*., 1998). This provides an estimate of the minimum stress needed in the slab. There are several other deep earthquakes with large predicted stress drops in the same region, including the 1970 Colombia (M_W 8.3) earthquake with a stress drop of 68 MPa (*Fukao and Kikuchi*, 1987; *Ruff*, 1999). The modeled slab allows for these stress drops, and shows ambient stresses that are almost everywhere equal to the yield stress, 100 MPa (Figure 2.1c). Locally, the stress is even greater, namely where the temperature is higher than the yield temperature. The modeled state of stress in the nominal model is in good agreement with earthquake focal mechanisms (Figures 2.1b and d). The stress axes indicate downdip tension in the hinge and shallow to intermediate depths in the slab, and compression in the deeper parts. This transition from tension to compression around 300 km depth is consistent with the focal mechanisms of *Isacks and Molnar* (1971).

The second case study focuses on the northern Tonga region, containing the 1994 M_W 7.6 earthquake. This is a highly complex area with several microplates and rapid trench rollback (*Bird* (2003); Figure 2.2a). The strain rate again indicates that the deformation almost exclusively occurs at plate boundaries. An additional constraint here is the estimate of a minimum average slab strain rate of 5×10^{-16} s^{-1}, determined from seismic moment release

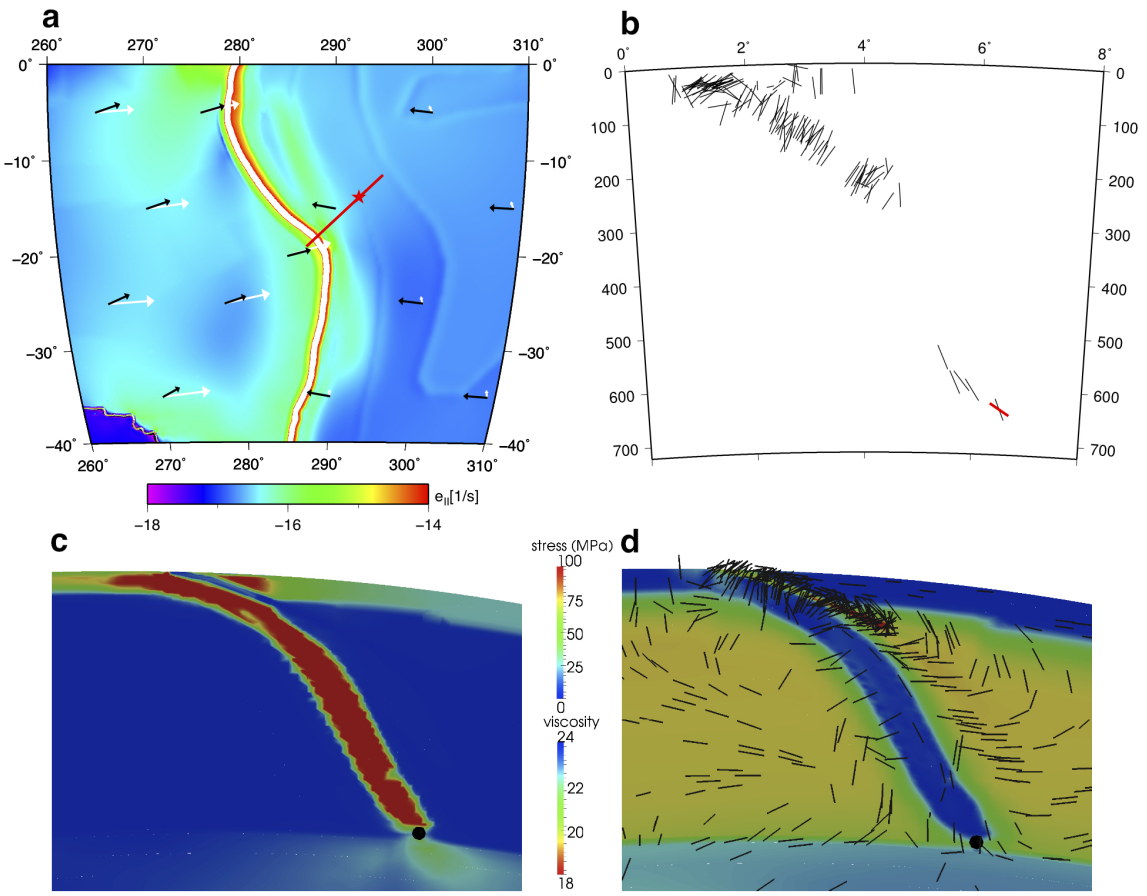

Figure 2.1. Bolivia region. (a) Map with plate motions in a no-net-rotation reference frame. Black arrows: Rhea model prediction; white arrows: Nuvel1-NNR plate motion model by *Argus and Gordon* (1991). Background color: second invariant of the strain rate. Red star: location of the Bolivia 1994 earthquake. Red line: location of the studied cross-section. (b) Cross-section with compressional axes from focal mechanisms of earthquakes with magnitude larger than 5.0 and within 100 km of the cross-section. Red axis: Bolivia 1994 event. (c) Cross-section of the stress magnitude. Black sphere: location of Bolivia 1994 event. (d) Cross-section of viscosity with compressional axes plotted with unit length.

(*Bevis*, 1988; *Holt*, 1995; *Nothard et al.*, 1996). In our nominal model, the strain rate is around or above this minimum in most of the slab, except in the plates and parts of the thicker slab interior (Figure 2.2c). The volume average of the strain rate in the slab is 7.6×10^{-16} s^{-1}, and satisfies the minimum condition. Focal mechanisms of earthquakes in this area (Figure 2.2b) show a pattern of mostly compression in the slab, except for the plate hinge and the immediate subsurface of the shallow parts of the slab. The pattern of the compressional stress axes (Figure 2.2d) matches these observations as well as inferences by *Isacks and Molnar* (1971). The gap in seismicity around 300 km depth corresponds to an area with lower strain rates, consistent with the generic models of *Vassiliou et al.* (1984).

Inspection of the stress field in models with different yield stress indicates that the orientation of the stress axes does not depend on the strength of the slab within the range of models tested. It appears that the stress orientations are determined by slab geometry rather than its strength within the range of models tested, since we see large variations in stress regime among slabs in both our models and in observations, as illustrated by the two case studies in this paper.

Global models show that a minimum value of 100 MPa for the maximum yield stress is required to acceptably fit plate motions and plateness arguments (*Stadler et al.*, 2010). A higher yield stress allows for less weakening in the hinge zone, slows the plate down, and causes lower strain rates (Figure 2.3). Studies of seismic moment release indicate that average strain rates in slabs above 175 km depth must be at least 10^{-15} s^{-1}, and below 200 km at least 5×10^{-16} s^{-1} (*Bevis*, 1988; *Holt*, 1995; *Nothard et al.*, 1996). Slab averages below 200 km depth and the value at 50 km depth for models with various yield stresses show that this provides an upper bound on the slab stress between 100 and 200 MPa (Figure 2.3a). The estimated stress drop for the Bolivia event determines a lower bound on the sustained slab

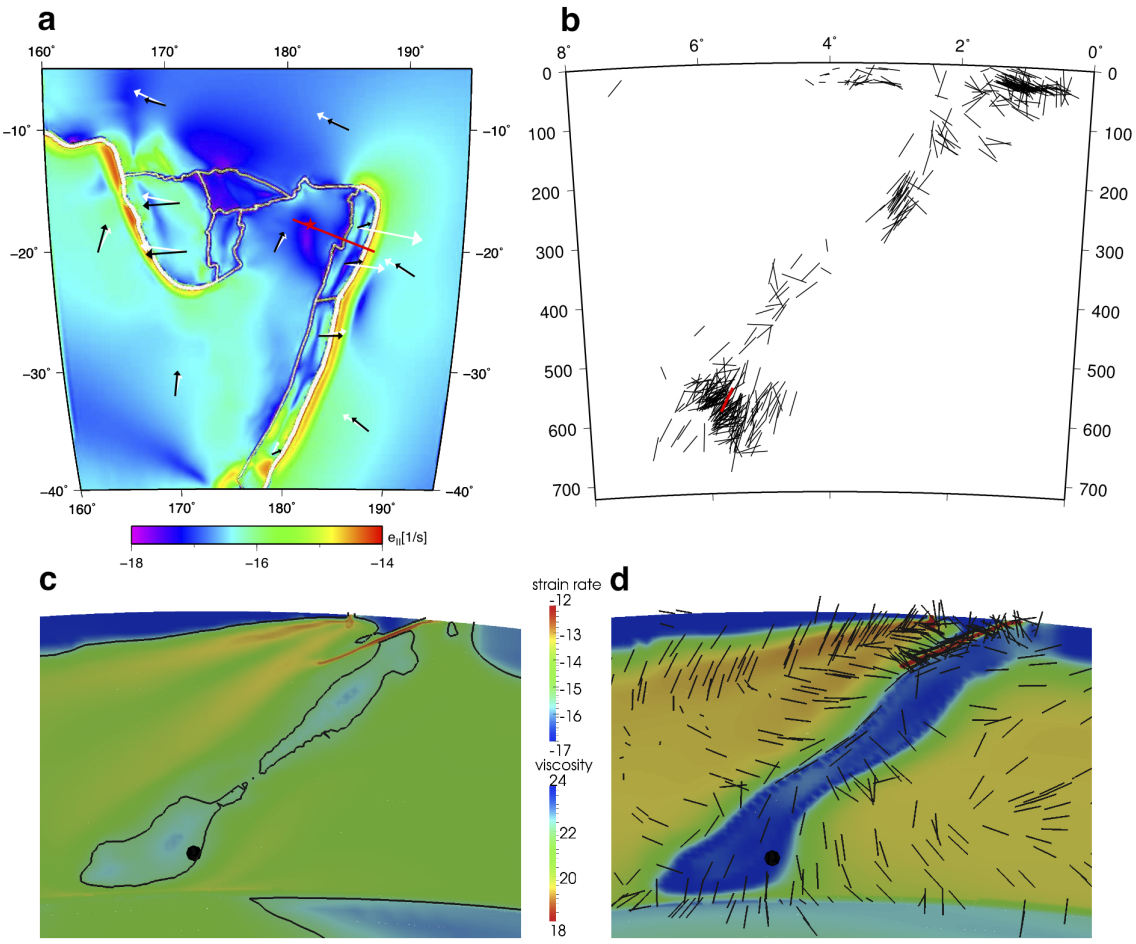

Figure 2.2. Tonga region. (a) Map with plate motions; see caption of Figure 2.1 for explanation of annotations. (b) Cross-section with compressional axes from focal mechanisms of earthquakes with magnitude larger than 5.0 and within 50 km of the cross-section. Red axis: Tonga 1994 event. (c) Cross-section of the second invariant of the strain rate. Black contour: value of 5×10^{-16} s^{-1}. (d) Cross-section of viscosity with compressional axes plotted with unit length.

stress of 100 MPa (*Kanamori et al.*, 1998) (Figure 2.3b). These requirements strongly limit the acceptable parameter space.

2.5 Discussion and Conclusions

Models with higher yield stress have higher viscosity and therefore higher ambient stress in the slab. For yield stresses larger than 200 MPa, the viscosity in the slab reaches the maximum cutoff value of 10^{24} Pa s, causing the ambient stress in the slab to be lower than the yield stress. Stress in the slab can locally be larger than the yield stress, if the temperature is higher than the yield temperature. The stress orientations do not vary between the models in this paper. However, they are dependent on radial viscosity gradients.

There are some limitations to the models presented. First, the thermal field in the upper mantle does not contain active upwellings. This could be significant in areas where plumes affect regional flow patterns. Second, the parameters used in the viscosity law are mostly established in laboratory experiments (*Hirth and Kohlstedt*, 2003), performed at low pressure and extrapolated to mantle conditions. The behavior of plates and slabs is sensitive to the choice of these parameters. Third, our models are instantaneous and hence do not include the time evolution of slabs, which would provide an additional constraint on the rheology parameters.

Stress drops of earthquakes provide a valuable constraint on the minimum stress sustained in a plate or slab. The actual stress drop on a fault can be highly heterogeneous due to spatial variability of stress and strength on the fault plane. This could result in high local stress drop compared to the average over the fault (*Venkataraman and Kanamori*, 2004). Stress drops are determined from seismic moment and rupture area, and accurately determining the rupture

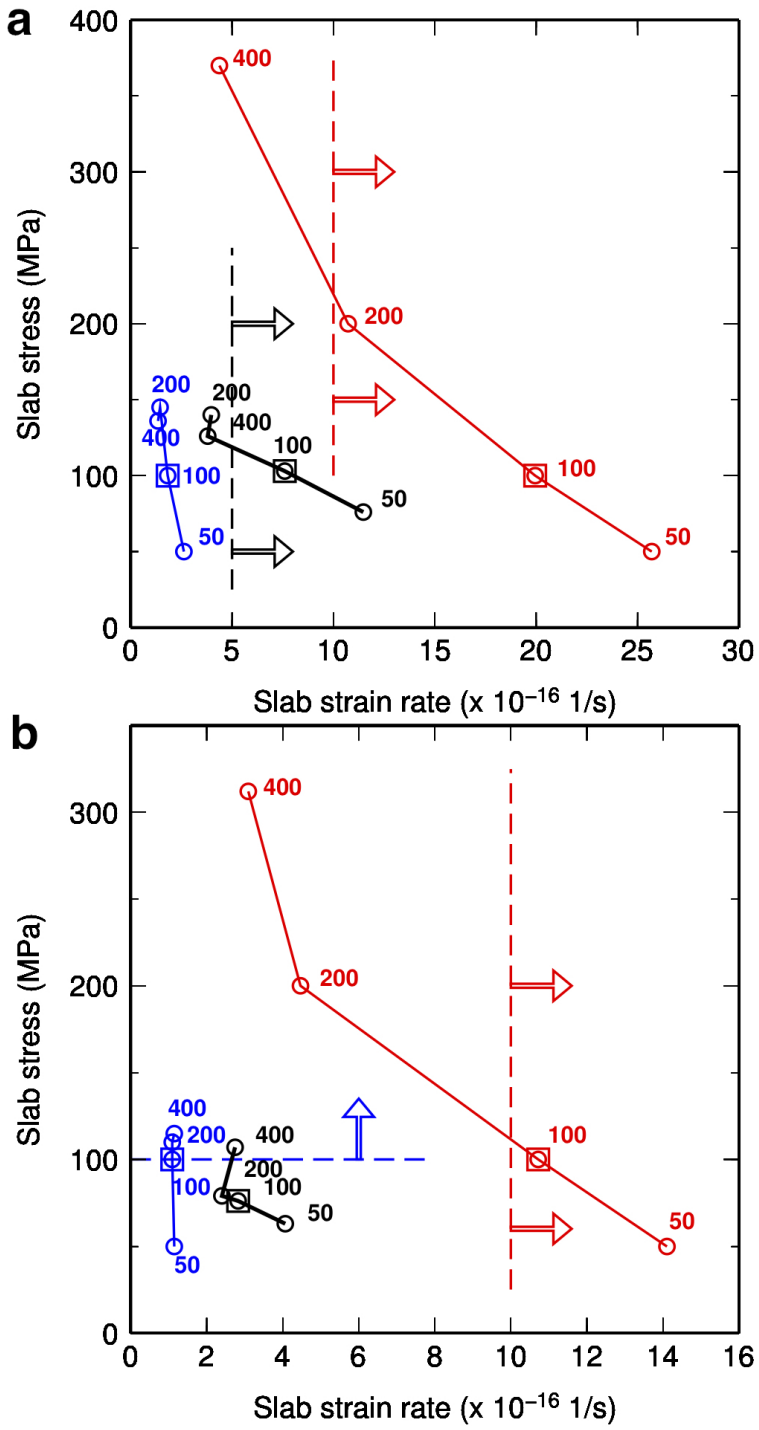

Figure 2.3. (a) Strain rate and stress in the Tonga slab. Black: average in the slab from 200 km depth to the slab tip, where the slab is defined by a viscosity contour of 5×10^{22} Pa s. Blue: value at the center of the slab at 600 km depth. Red: value at the center of the slab at 50 km depth. Square: nominal model. The numbers next to the data points refer to the global maximum yield stress used. Black dashed line: minimum average strain rate of 5×10^{-16} s^{-1} below 200 km; red line: minimum of 10^{-15} s^{-1} in the shallow slab (*Bevis*, 1988). (b) Strain rate and stress in the Bolivia slab; same color coding. Blue dashed line: minimum stress value of 100 MPa required by the stress drop at 600 km depth (*Kanamori et al.*, 1998).

area remains an active field of research (*Venkataraman and Kanamori*, 2004; *Kanamori and Brodsky*, 2004). Also, there is currently also no method available to determine how much higher the actual stress is compared to the stress drop (*Kanamori and Brodsky*, 2004). A recent study of exhumed ultramafic pseudotachylytes suggests that higher stresses could be required in slabs than previously inferred from earthquake inversions; the estimated stress drop determined from the geologic record for deep earthquakes in Corsica is at least 220 MPa, and could be as much as 580 MPa (*Andersen et al.*, 2008).

In our models, the localization of strain in the hinges of subducting slabs causes significant weakening of the material up to 2 orders of magnitude in viscosity. This process allows the rest of the slab to remain strong while still having sufficiently fast moving plates. Pointwise the dissipation of energy in the mantle is highest in the subducting plate hinges, but the integration over this very small volume compared to the rest of the mantle results in only 3%–5% of the total dissipation (*Stadler et al.*, 2010). This is consistent with findings by *Leng and Zhong* (2010).

We have studied the state of stress in slabs in globally consistent dynamic models of mantle convection with plates, and are able to reproduce the general trends in stress orientations in the Bolivia and Tonga case studies, as observed from earthquake focal mechanisms. These models have strong slabs and weak subducting plate hinges, such that the dissipation in the bending areas of plates is small compared to the total dissipation of energy from the mantle. A lower bound on the strength of slabs is provided by the stress drop in strong deep earthquakes. Because models with higher yield stress have lower strain rates in slabs, the minimum average strain rate in slabs determined from seismic moment release gives an upper bound on the strength of the slabs.

Acknowledgements

We thank H. Kanamori and D. Stegman for helpful discussions. This work was partially supported by NSF's PetaApps program (OCI-0749334, OCI-0748898), NSF Earth Sciences (EAR-0426271, EAR-0810303), and the Caltech Tectonics Observatory (by the Gordon and Betty Moore Foundation). Computing resources on TACC's Ranger and Spur systems were provided through the NSF TeraGrid under grant number TG-MCA04N026. The figures in this paper were produced using GMT and Paraview.

Chapter 3

Multi-Scale Dynamics and Rheology of Mantle Convection with Plates

Submitted as:

Alisic, L., Gurnis, M., Stadler, G., Burstedde, C., & Ghattas, O. Multi-scale dynamics and rheology of mantle flow with plates, *Journal of Geophysical Research*.

3.1 Abstract

Fundamental issues in our understanding of plate and mantle dynamics remain unresolved, including the rheology and state of stress of plates and slabs; the coupling between plates, slabs, and mantle; and the flow around slabs. To address these questions, models of global mantle flow with plates are computed using adaptive finite elements, and compared to a variety of observational constraints. The dynamically consistent instantaneous models include a composite rheology with yielding, and incorporate details of the thermal buoyancy field. Around plate boundaries, the local mesh size is $\sim$ 1 km, which allows us to study highly detailed features in a globally consistent framework. Models that best fit plateness criteria and plate motion data have strong slabs with high stresses. We find a strong dependence of global plate motions, trench rollback, net rotation, plateness, and strain rate on the stress exponent in the nonlinear viscosity; the yield stress is found to be important only if it is smaller than the

ambient convective stress. Due to strong coupling between plates, slabs, and the surrounding mantle, the presence of lower mantle anomalies affect plate motions. The flow in and around slabs, microplate motion, and trench rollback are intimately linked to the amount of yielding in the subducting slab hinge, slab morphology, and the presence of high-viscosity structures in the lower mantle beneath the slab.

3.2 Introduction

Significant insight into the forces which govern plate tectonics has been gained through both global and regional studies of mantle convection with plates. Examples are the relation between slab pull and ridge push as driving forces for plate tectonics, the evolution of slabs with plate motions as kinematic boundary conditions, and the effect of radial viscosity variations on plate motions and the state of stress in plates and slabs. However, some of the questions basic to our understanding of the dynamics of the mantle and plates remain unresolved, such as the rheology and state of stress of plates and slabs; the coupling between plates, slabs, and mantle; and the flow around slabs.

Several fundamental issues revolve around the rheology of the mantle and lithosphere; for instance the strength of plates and subducting slabs has not been uniquely determined. In regional studies constrained by the geoid, the viscosity of slabs has been inferred to be 100 to 1000 times higher than in the surrounding mantle (*Moresi and Gurnis*, 1996), and could not exceed 10^{23} Pa s in order to fit geoid highs over subducted slabs (*Billen et al.*, 2003). Torque balance models of the Pacific and Australian plates suggested that the best fit to observed rotation poles was obtained with an effective lithosphere viscosity of 6×10^{22} Pa s (*Buffett and Rowley*, 2006). Studies that address plate bending in generic subduction

zone models indicate that the plate viscosity must be between 50 and 200 times the mantle viscosity in order to reproduce observed ranges of plate velocities (*Conrad and Hager*, 1999a), for which an effective viscosity of 10^{23} Pa s in the bending lithosphere is sufficient (*Conrad and Hager*, 2001). Additionally, studies addressing slab morphology show that slabs must be weak (i.e., with a viscosity of 10^{23} Pa s or less), in order to reproduce observed trench migration (*Zhong and Gurnis*, 1995; *Enns et al.*, 2005; *Stegman et al.*, 2006). *Liu and Stegman* (2011) used Farallon slab morphology from tomography models to constrain rheology of the upper mantle in time-dependent convection models, and inferred an upper mantle slab viscosity of $\sim 5 \times 10^{21}$ Pa s, weakening to 1.5×10^{21} Pa s in the transition zone. In contrast, with time-dependent generic models of slab dynamics, strong slabs are inferred with viscosities of around 10^{24} Pa s (*Billen and Hirth*, 2007), assuming the experimentally determined strong temperature dependence of the effective viscosity of olivine (*Hirth and Kohlstedt*, 2003).

Localized yielding in the hinge of a subducting slab allows slabs to be strong while continuing to move alongside the overriding plate and subduct with relative ease (*Ribe*, 1992). There are several observations supporting localized weakening in hinges of subducting plates. Studies of bending-related faulting in the outer rise of trenches in Middle and South America show a pervasive tectonic fabric with inferred serpentinization in outer trench walls, which qualitatively suggests deformation and weakening of the subducting plate (*Ranero et al.*, 2003; *Grevemeyer et al.*, 2005). Lithospheric earthquakes within the subducting oceanic plate, which are large-magnitude events on faults which completely cut through the lithosphere, provide additional evidence for permanent deformation within a trench (*Kikuchi and Kanamori*, 1995; *Gurnis et al.*, 2000b). Trench-perpendicular profiles of bathymetry in the Peru-Chile trench indicate that the effective elastic thickness of the subducting plate is reduced to $\sim$ 50–65% of the plate's mechanical thickness due to yielding (*Judge and McNutt*, 1991), averaged over the

length scale of plate bending. Gravity measurements within the Kermadec trench allow more localized quantification of this weakening, and show that the flexural rigidity of plates is reduced by 3 to 5 orders of magnitude from the forebulge to the trench axis, which indicates that the subducting plate has little or no elastic strength there (*Billen and Gurnis*, 2005). Using a composite rheology which incorporates both diffusion and dislocation creep with a nonlinear component along with yielding allows for such localization of strain, as strain weakening can reduce the viscosity in the hinge zone from 10^{24} to $\sim 5 \times 10^{22}$ Pa s (*Billen and Hirth*, 2007).

Related to slab strength is the state of stress in the slab and surrounding mantle. Principal compression and tension directions have been estimated from earthquake focal mechanisms in slabs (*Isacks and Molnar*, 1971; *Alpert et al.*, 2010). Numerical mantle convection models at global (*Alpert et al.*, 2010) and regional scales (*Billen et al.*, 2003; *Carminati and Petricca*, 2010) indicate that the state of stress in slabs resulting from numerical models depends on the radial viscosity structure, and on the 3-D geometry of the subducting slabs. However, challenges to reproduce the state of stress in these studies persist, as deviations between the predicted and observed state of stress remain significant.

The rheology also directly influences the manner in which plates and slabs are coupled to the surrounding mantle. The stronger plates are, the more they could exert a force on plate motions, while they act as stress guides between the upper mantle and lithosphere (*Elsasser*, 1969). Global models addressing slab pull show that slabs which are strong enough to remain coupled to plates throughout subduction provide the best fit to observed plate motions, exerting slab pull forces that account for approximately 50% to 70% of the total driving forces on plates (*Becker and O'Connell*, 2001; *Conrad and Lithgow-Bertelloni*, 2002).

Observations of shear wave spliting around slabs putatively provide insight on mantle flow around subducting slabs (*Wiens and Smith*, 2003; *Long and Silver*, 2008, 2009). Accounting

for the downward and/or downdip motion of subducting slabs, one would expect trench-perpendicular flow both on top of and beneath subducting slabs through viscous coupling between the subducting slab and the surrounding mantle. However, the anisotropy estimated from shear wave splitting measurements has been interpreted as implying a significant trench-parallel component to the flow, suggesting a more complex flow pattern around slabs (*Long and Silver*, 2008). *Wiens and Smith* (2003) attributed the observed splitting to trench-parallel flow in the wedge, induced by the opening of backarc basins. Alternatively, the observed anisotropy could be caused by the presence of highly anisotropic minerals formed along faults in the subducting lithosphere (*Faccenda et al.*, 2008). Slab-faulting induced anisotropy would suggest that shear-wave splitting in subduction zones provides little constraint on mantle flow around slabs. Numerical mantle convection models have had limited success in reproducing the trench-parallel flow except around slab edges (*Long and Becker*, 2010; *Jadamec and Billen*, 2010), which seems to indicate that either the observed anisotropy is not fully understood, or the numerical models lack necessary components.

To address these issues, numerical models of global mantle flow are developed, which incorporate significant detail in the thermal buoyancy field, and a composite rheology with yielding. An extremely high local resolution of 0.5 to 4 km is needed around tectonic plate boundaries and slabs to allow for localized weakening in the hinge zone of the subducting plate (*Gurnis et al.*, 2004; *Billen and Hirth*, 2007), and to accommodate the orders-of-magnitude variation in viscosity over short distances between the strong, cold slabs and the weak mantle wedge (*van Keken et al.*, 2002). Additionally, an accurate representation of the buoyancy field for the slab requires high resolution, such that the slab can act as a stress guide (*Zhong et al.*, 1998). Consequently, the mesh size required in global numerical models can become too large for current-generation computers. Adaptive mesh refinement (AMR) is an

approach in which only the areas in a mesh with large changes in material properties over short distances have high resolution; elsewhere a low resolution is allowed. This technique reduces the total number of elements necessary in the whole mesh while still capturing the small-scale features. However, even with AMR, global mantle convection models are still large computational problems requiring several hundreds of millions of elements. Hence, a highly efficient and scalable parallel implementation is required to make these models computationally feasible on today's supercomputers (*Burstedde et al.*, 2008a, 2009b).

In this paper, we assess competing effects of rheological parameters and regional characteristics on mantle dynamics in instantaneous models of mantle flow. By utilizing the new computational methods available, we can study detailed regional features in a globally consistent framework. First, the methods used to compute and analyze the global mantle convection models are described. Then, we explore the effects of changes in rheological parameters on plate motions at a global scale, plateness, and net surface rotation as a first-order test of the results. Models are then assessed using the strain rates and the state of stress in slabs and overriding plates. Finally, the details of regional slab dynamics are studied by investigating flow in and around slabs together with microplate behavior and trench rollback.

3.3 Methods

3.3.1 Numerical Methods

Models of instantaneous mantle convection are computed under the Boussinesq approximation with uniform composition. The nondimensionalized strong form of the governing equa-

tions, the conservation of mass and momentum, are given by:

$$\nabla \cdot \mathbf{u} = \mathbf{0}, \tag{3.1}$$

$$\nabla \mathbf{p} - \nabla \cdot \left[\eta(T, \mathbf{u}) \left(\nabla \mathbf{u} + \nabla \mathbf{u}^{\top} \right) \right] = \mathrm{Ra}\, T\, \mathbf{e}_r, \tag{3.2}$$

where $\mathbf{u}$, $\mathbf{p}$, η, and T are the velocity, pressure, viscosity, and temperature, respectively, and $\mathbf{e}_r$ is the unit vector in the radial direction (e.g., *Schubert et al.* (2001)). Ra is the Rayleigh number, $\mathrm{Ra} = \alpha \rho_o g \Delta T R_o^3 / (\kappa \eta_o)$, where α, ρ_o, η_o, and κ are the reference coefficients of thermal expansion, density, viscosity, and thermal diffusivity (see Table 3.1). ΔT is the temperature difference across the mantle, R_o is the radius of the Earth, and g is the gravitational acceleration. The boundaries at the surface and core-mantle boundary are stress-free in the tangential direction, and have zero velocity in the normal direction. Interior and surface velocities, along with viscosity, strain rate, and state of stress are model outcomes.

The equations are solved with `Rhea`, a finite element mantle convection code designed to run on hundreds of thousands of cores (*Burstedde et al.*, 2012). The code uses the octree-based `p4est` library (*Burstedde et al.*, 2008a, 2011) for adaptive mesh refinement. The leaves of an adaptive octree correspond to elements of a recursively subdivided hexahedral mesh, without holes or overlaps. Connecting the leaves in a tree traversal, where the sequence of eight children is always the same (we choose z-ordering, i.e., from lower front left, lower front right, lower back left, etc., to upper back right), creates a space-filling curve that induces a unique total ordering of all mesh elements. Recursive refinement and coarsening of an octree mesh can create neighboring elements of different sizes. The maximum size difference between neighboring elements is restricted to a factor of two (these meshes are called 2:1 balanced). A parallel partition is defined by segmenting the curve into pieces of equal number

of elements. The `p4est` library implementing these AMR algorithms has been scaled to more than 220,000 processor cores (*Burstedde et al.*, 2010, 2011), although only exactly 6,000 were used for the calculations here.

The initial temperature field is interpolated on a finite element mesh with about 22 million elements, which is refined radially in the upper mantle. First, this initial mesh is coarsened and refined based on temperature variations. Then, the mesh is refined down to 1–2 km element size over the plate boundaries at the surface, which are defined as narrow low-viscosity zones $\sim$ 10 km wide. This leads to meshes with about 100 million elements. Solution of the Stokes equations begins only after these initial AMR steps. The mesh is further refined during the iterative solution of the nonlinear flow system to resolve localization of deformation. Here, element-based error indicators are used to determine which finite elements to refine (or coarsen) during the simulation. The error estimator E is given by a weighted sum of the element integrals of the local temperature and viscosity gradients, and the second invariant of the strain rate:

$$E_e = w_1 \left|\nabla \eta_e\right| + w_2 \left|\nabla T_e\right| + w_3 \left|\nabla T_e \cdot \mathbf{r}\right| + w_4 \, \dot{\varepsilon}_{\mathrm{II}\, e}, \tag{3.3}$$

where e denotes element-based quantities. The terms with gradients in viscosity and temperature allow for refinement at the transition between the cold and highly viscous plates and slabs, and the hotter and less viscous asthenosphere. The temperature gradient in the radial direction ($\nabla T_e \cdot \mathbf{r}$) adds radial refinement to the mesh, essentially at the mantle-lithosphere transition. Additionally, the gradient in viscosity refines the mesh around weak plate boundaries and areas with yielding. Finally, the second invariant of the strain rate adds additional refinement in the mantle wedge (where velocities tend to be high) and in the hinge zone of the subducting plate.

While we apply both refinement and coarsening to the initial mesh during preprocessing, only refinement is enabled during the model run. In each iteration of the solution process we first mark 10–20% of the elements, where the error indicator is large, to be refined. Then, to improve the accuracy of mass conservation, we additionally mark elements for which the divergence of velocity (equation 3.1) is large. The marked elements are then refined after this marking stage. We usually perform about 6–8 such solution-based refinements, resulting in meshes with about 200–300 million finite elements on up to 8 different refinement levels. Typical linear systems arising in our simulations have between 400 million and 1.2 billion unknowns and require a minimum of 4000–5000 processor cores for their solution.

The governing equations 3.1 and 3.2 are solved iteratively by a block preconditioned Krylov method that employs an algebraic multigrid (AMG) subpreconditioner. Discretizing the Stokes equations results in the following matrix problem:

$$Q \begin{pmatrix} \mathbf{u} \\ \mathbf{p} \end{pmatrix} = \begin{pmatrix} \mathbf{f} \\ 0 \end{pmatrix} \qquad \text{with} \qquad Q = \begin{pmatrix} A & B^\top \\ B & -C \end{pmatrix}, \tag{3.4}$$

where $\mathbf{u}$, $\mathbf{p}$, and $\mathbf{f}$ denote the discretized velocity, pressure, and external force. The block matrices A and C are symmetric and positive definite and, thus, equation (3.4) is an indefinite symmetric system. C is a result of the pressure stabilization, which is necessary due to the use of trilinear finite elements for both velocity and pressure (*Dohrmann and Bochev*, 2004; *Elman et al.*, 2005). For the solution with the system matrix Q we employ the preconditioned minimum residual method (MINRES) (*Paige and Saunders*, 1975; *Elman et al.*, 2005). Combining MINRES with an efficient preconditioner is critical to solve systems of the size of our

mantle flow simulations. To construct a preconditioner, we factor the matrix Q as follows:

$$\begin{pmatrix} A & B^\top \\ B & -C \end{pmatrix} = \begin{pmatrix} I & 0 \\ BA^{-1} & I \end{pmatrix} \begin{pmatrix} A & 0 \\ 0 & -(BA^{-1}B^\top + C) \end{pmatrix} \begin{pmatrix} I & A^{-1}B^\top \\ 0 & I \end{pmatrix}, \tag{3.5}$$

showing that Q is congruent to a block diagonal matrix. Neglecting the off-diagonal terms BA^{-1} and $A^{-1}B^\top$ motivates the use of the symmetric and positive definite matrix

$$P = \begin{pmatrix} A & 0 \\ 0 & S \end{pmatrix}, \qquad \text{with} \qquad S = BA^{-1}B^\top + C, \tag{3.6}$$

as preconditioner. We approximate the Schur complement S with a lumped mass matrix weighted by the inverse viscosity (η^{-1}), motivated by spectral equivalence results for constant viscosity (*Elman et al.*, 2005). To invert the resulting block-diagonal preconditioner, one V-cycle of an algebraic multigrid (AMG) solver is used for the viscous block A, for which we rely on the parallel smoothed aggregation code `ML` (*Gee et al.*, 2006). See *Burstedde et al.* (2009b) for more details on the parallel Stokes solver.

A nonlinear rheology requires additional iterations over the viscosity and velocity until convergence is achieved, which is measured by the change in the L_2 norm of the velocity from iteration $i-1$ to i:

$$c = \frac{||\mathbf{v}_i - \mathbf{v}_{i-1}||_2}{||\mathbf{v}_i||_2} < c_{\text{convergence}} \tag{3.7}$$

The velocity determines the strain rate used in the viscosity computation. This viscosity is then used to compute the solution to the Stokes problem in equation (3.2) with velocity as an outcome. To initialize the nonlinear iterations, a uniform strain rate of 10^{-16} s^{-1} is used, an order of magnitude smaller than the transition strain rate between diffusion and dislocation creep,

so that the first estimate occurs entirely in the diffusion creep regime (*Hirth and Kohlstedt*, 2003).

Parameter	Symbol	Value
density	ρ_o	3300 kg m^{-3}
gravitational acceleration	g_o	9.81 m s^{-2}
thermal expansion coefficient	α	2.0×10^{-5} K^{-1}
temperature scaling	ΔT	1400 K
thermal diffusivity	κ	10^{-6} m^2/s
reference viscosity	η_o	10^{20} Pa s
radius	R_o	6.371×10^6 m
Rayleigh number	$Ra = \frac{\rho_o g_o \alpha \Delta T R_o^3}{\eta_o \kappa}$	2.344×10^9

Table 3.1. Parameters used to nondimensionalize the mantle flow equations.

3.3.2 Model

The global models require as input a buoyancy field in the form of temperature, and plate boundaries represented by narrow weak zones. The temperature field consists of several parts: the lithosphere, subducting slabs in the upper mantle, and lower mantle structure. The lithospheric thickness is derived from a half-space cooling model using the lithospheric age (e.g. *Schubert et al.* (2001)):

$$T_L(z,\tau) = T_s + (T_m - T_s)\,\mathrm{erf}(\frac{z}{2\sqrt{\kappa\tau}}), \tag{3.8}$$

where T_s and T_m are the surface and mantle temperatures, κ is the thermal diffusivity, τ the age of the lithosphere, and z is depth. The age of the oceanic lithosphere is determined from a map of lithospheric plate age (*Müller et al.*, 2008). Within areas not purely oceanic, three types of crust are defined: cratons with an age of 300 Ma (*Stoddard and Abbott*, 1996; *Spasojevic et al.*, 2010), areas within a distance of $\sim$ 750 km to (recent) subduction zones with an age of 75 Ma, and remaining areas with an age of 125 Ma (*Stadler et al.*, 2010).

Slabs need to be well resolved so that they have the option of acting as stress guides (*Zhong et al.*, 1998). The use of global tomography models is avoided in the upper mantle, because they are almost always smoother than what one would expect from thermal models of subduction. Where high resolution tomography exists, it is consistent with thermal models (*Schmandt and Humphreys*, 2010). Because such high resolutions do not exist globally, a thermal model of upper mantle slabs is based on smooth slab contours defined by seismicity based on the RUM model (*Gudmundsson and Sambridge*, 1998), and a local age based on lithospheric age at the trench just before the plate subducts. Using cubic splines, these smooth contours are extrapolated to the radial coordinates of the finite element mesh used for the input model. A thermal age for these slab contours is obtained from the age grid of the oceanic lithosphere (*Müller et al.*, 2008), and thickness of the effective lithosphere taken from the half space thermal mode (equation (3.8)). Using GMT routines (*Wessel and Smith*, 1991), this thermal field is smoothed onto a uniform raster file and then resampled on the initial finite element mesh.

The lower mantle structure is derived from the S20RTS tomography model (*Ritsema et al.*, 2004), a seismic S-wave model using both body and surface waves. The tomography model is scaled into nondimensional temperature anomalies using $\delta T = -\omega\, \delta V_s$, with the scaling factor ω varied for different models within the range [0.0, 0.25] (*Karato and Karki*, 2001; *Forte*, 2007). The lithosphere and upper mantle models and the upper and lower mantle models are blended at 75 km and 650 km depths, respectively, over a length scale of 75 km.

The surface positions of convergent plate margins and mid-ocean ridges are derived from a compilation by *Bird* (2003). To incorporate the trenches, fracture zones, and ridges in our models, the line data is propagated downward from the surface using specified dip angles in a preprocessing step. For converging plate boundaries, a surface is created with a dip angle

starting at 0 km depth (θ_o), which transitions to a second dip angle (θ_i) at a depth (z_i). The parameters θ_o, θ_i, and z_i can all vary along strike, and are obtained for thrust events with $M_w \geq$ 5.5 using the hypocenters and dip angles of CMT solutions (*Dziewonski and Anderson*, 1981) over a 32 year period (Global CMT Project, available at http://www.globalcmt.org/, accessed September 2009). Point clouds describing the resulting surfaces are imported into our finite element implementation, where a viscosity reduction factor is computed based on the distance along outward normal vectors to these fault surfaces. This factor $\Gamma(\mathbf{x})$, which multiplies the viscosity (see below), is derived as

$$\Gamma(\mathbf{x}) = 1 - (1 - w) \exp\left(-\frac{x_1^2}{2a^2}\right) \quad \text{with} \quad x_1 = \max(0, x - a), \tag{3.9}$$

where x denotes a point's normal distance to the trench or ridge surface, a the half-width of the weak zone, and w the prefactor for the viscosity. Nominally, $a = 5$ km and $w = 10^{-5}$ are used, resulting in Gaussian smoothed zones with a width of about 10 km, in which the viscosity is reduced by five orders of magnitude. The weak zones extend deeper into the mantle than seismogenic zones in order to mimic the effect of viscosity reduction associated with the release of water into the mantle wedge (*Hebert et al.*, 2009). Only the boundary between the Nazca and South America plates around Peru has a higher viscosity with $w = 5 \times 10^{-3}$. The Peru-Chile trench region has seen several large earthquakes with magnitudes larger than 8.0 and is in a strong compressional regime (*Isacks and Molnar*, 1971; *Uyeda and Kanamori*, 1979; *Jarrard*, 1986), which points to significant coupling between the overriding and subducting plates. Increasing the weak zone factor locally from 10^{-5} to 5×10^{-3} significantly improved plate motion fits for the Nazca plate (*Stadler et al.*, 2010).

The rheology is a composite of linear (Newtonian) and nonlinear (non-Newtonian) vis-

cosity, combined with a yielding law (*Billen and Hirth*, 2007). The dominant mechanism in the upper mantle is the nonlinear dislocation creep (ds), and in the lower mantle the linear diffusion creep (df). We use a general viscosity law from *Hirth and Kohlstedt* (2003):

$$\eta_{df,ds} = \left(\frac{d^p}{A\, {C_{\mathrm{OH}}}^r}\right)^{\frac{1}{n}} \dot{\varepsilon}_{\mathrm{II}}^{\frac{1-n}{n}} \exp\left(\frac{E_a + PV_a}{nRT}\right), \tag{3.10}$$

where η is viscosity in Pa s, d grain size in μm, C_{OH} water content in parts per million of silicon, and n the stress exponent. $\dot{\varepsilon}_{\mathrm{II}}$ is the second invariant of the strain rate tensor in s^{-1}:

$$\dot{\varepsilon}_{\mathrm{II}} = \left[\frac{1}{2}\sum_{ij} \dot{\varepsilon}_{ij}\dot{\varepsilon}_{ij}\right]^{\frac{1}{2}}. \tag{3.11}$$

E_a is the activation energy in J/mol, P lithostatic pressure in Pa, V_a activation volume in m^3/mol, and R the gas constant. The temperature T is defined as:

$$T = T_s + T_{ad} + T_l \Delta T, \tag{3.12}$$

where T_s is the surface temperature, T_l the nondimensional local ambient temperature, and T_{ad} the adiabatic temperature. The parameters A, n, r, and p are determined experimentally (*Hirth and Kohlstedt*, 2003). The composite viscosity is obtained by combining the viscosity from diffusion creep (η_{df}) and viscosity from dislocation creep (η_{ds}) using a harmonic mean. Along with a yield criterion with yield strength σ_y, we obtain an effective viscosity:

$$\eta_{\mathrm{comp}} = \frac{\eta_{df}\eta_{ds}}{\eta_{df} + \eta_{ds}}, \tag{3.13}$$

$$\sigma_y = \min\left(\sigma_o + \frac{\delta\sigma}{\delta z}, \sigma_y^{\max}\right), \tag{3.14}$$

$$\eta_{\text{eff}} = \Gamma(\mathbf{x}) \min\left(\frac{\sigma_y}{\dot{\varepsilon}_{\text{II}}}\ ,\ \eta_{\text{comp}}\right). \tag{3.15}$$

The yielding law is only applied if the local temperature is lower than the yield temperature T_y. $\Gamma(\mathbf{x})$ is the reduction factor used to define weak zones, as described in equation (3.9). The stress exponent n in equation (3.10) determines the nonlinearity of the system, and hence has a substantial impact on the model outcome. The maximum yield stress $\sigma_y^{\max}$ is also an essential parameter in the global models, because it determines the strength of plates and slabs. Both of these parameters, n and σ_y, are varied in this study. In Table 3.2, we provide further explanation and associated numerical values of the parameters in the constitutive equations.

Parameter	Symbol	Upper mantle dislocation creep	Upper mantle diffusion creep	Lower mantle diffusion creep
grain size	d	—	$10 \times 10^3 \mu$m	$100 \times 10^3 \mu$m
grain size exponent	p	—	3.0	3.0
pre-exponent	A	9×10^{-20}	1.0	1.0
water content	C_{OH}	10^3 ppm	10^3 ppm	10^3 ppm
water content exponent	r	1.2	1.0	1.0
stress exponent	n	3.0*	1.0	1.0
activation energy	E_a	480×10^3 J/mol	335×10^3 J/mol	335×10^3 J/mol
activation volume	V_a	11×10^{-6} m^3/mol	2×10^{-6} m^3/mol	1.25×10^{-6} m^3/mol
yield temperature	T_y	1073 K	1073 K	1073 K
surface yield stress	σ_o	0.1 MPa	0.1 MPa	0.1 MPa
yield stress gradient	$\delta\sigma/\delta z$	15 MPa/km	15 MPa/km	15 MPa/km
maximum yield stress	$\sigma_y^{\max}$	100 MPa*	100 MPa*	100 MPa*

Table 3.2. Parameters used in the viscosity law for the reference model. * denotes values varied in this study.

3.3.3 Model Analysis

Several quantities are used to analyze and compare global models with each other: plate velocities, net surface rotation, plateness, and strain rates and state of stress in plates and slabs. The velocities at the surface are compared to the NNR_NUVEL1A plate motion model in the no-net-rotation (NNR) reference frame (*DeMets et al.*, 1994), and to the HS3_NUVEL1A model

in the hotspot reference frame (*Gripp and Gordon*, 2002). We also made spot comparisons for the main plates to the NNR_MORVEL56 model (*Argus et al.*, 2011), and found that differences with the earlier kinematic models with no net rotation are significantly smaller than the differences with the outcomes of the numerical models. Comparison to the NNR_NUVEL1A is accomplished by removing the net surface rotation from the surface velocity field. The net rotation is computed from the surface velocities as follows (*Torsvik et al.*, 2010):

$$\omega_{net} = \frac{3}{8\pi r^4} \sum_i \int_S (\omega_i \times \mathbf{r}) \times \mathbf{r} \, ds_i, \tag{3.16}$$

where $\mathbf{r}$ is the position vector, ω_i the rotation rate vector of plate i, $\int_S ...ds$ the integration over the entire sphere, $\int_S ...ds_i$ the integration over the area of plate i, and $\sum_i$ the summation over all plates. The net surface rotation of the numerical models can be compared to estimates derived from paleo plate motion data and to previous modeling studies (*Becker*, 2006; *Conrad and Behn*, 2010; *Torsvik et al.*, 2010). Surface velocities are also compared to the HS3_NUVEL1A hot spot reference frame model, which requires the lower mantle rotation instead of the net surface rotation be removed from surface velocities.

For each plate, the misfit α of the velocity direction with respect to a particular plate model is computed, and integrated over the plate:

$$\alpha = \frac{1}{S} \int_S \sin^{-1} \frac{\|\mathbf{v}_r \times \mathbf{v}_a\|}{\|\mathbf{v}_r\| \, \|\mathbf{v}_a\|} \, ds, \tag{3.17}$$

where $\mathbf{v}_r$ is the surface velocity resulting from the numerical model, and $\mathbf{v}_a$ the actual velocity described by the plate motion model within the domain (plate polygon) S. Similarly, the plate velocity magnitude misfit m is computed as the ratio between the averaged plate velocity in the numerical model and the average velocity in the plate according to the plate motion

model:

$$m = \frac{\frac{1}{S}\int_S \|\mathbf{v}_r\|\, ds}{\frac{1}{S}\int_S \|\mathbf{v}_a\|\, ds}. \tag{3.18}$$

Additionally, we use two different measures of plateness, indicating how well a plate behaves like a rigid block with deformation only at the boundaries. This is expressed in how much the plate moves according to one rotation pole, in two different ways:

$$P_1 = \frac{1}{S}\int_S \frac{|\mathbf{v}_r \cdot \mathbf{v}_{bf}|}{\|\mathbf{v}_r\|\, \|\mathbf{v}_{bf}\|}\, ds, \tag{3.19}$$

$$P_2 = 1 - \frac{1}{S}\int_S \frac{\|\mathbf{v}_r - \mathbf{v}_{bf}\|}{\|\mathbf{v}_r\|}\, ds, \tag{3.20}$$

where $\mathbf{v}_r$ is the surface velocity resulting from the numerical model, and $\mathbf{v}_{bf}$ is the surface velocity from the best fitting Euler pole (i.e., the pole which best fits all the computed velocities) within the domain S. $\|\cdot\|$ denotes the Euclidean norm and thus $\|\mathbf{v}_r - \mathbf{v}_{bf}\|$ is the root mean square (RMS) difference. A plateness of 1 implies that the plate is moving entirely with one rotation pole, and hence is a "perfect" plate. Plateness P_1 is a measure of how well aligned the local velocity is to the velocity resulting from a single rotation pole. P_2 also takes into account magnitude differences between the local velocity and the best fitting pole velocity.

Changes in rheology and temperature scaling of lower mantle anomalies can have an important effect on the bulk viscosity in the numerical models. Because the rheology is nonlinear, this effect cannot be predicted a priori. Therefore, we compute averaged viscosities of the upper and lower mantle to determine how the stress exponent, yield stress, and lower mantle tomography scaling affect the bulk viscosity. Two different formulations are used (*Parmentier et al.*, 1976; *Christensen*, 1984):

$$\langle\langle\eta\rangle\rangle_1 = \frac{\int_V \eta\ \dot{\varepsilon}_{\mathrm{II}}\ dV}{\int_V \dot{\varepsilon}_{\mathrm{II}}\ dV}, \tag{3.21}$$

$$\langle\langle\eta\rangle\rangle_2 = \frac{\int_V \eta\ \dot{\varepsilon}_{\mathrm{II}}^2\ dV}{\int_V \dot{\varepsilon}_{\mathrm{II}}^2\ dV}, \tag{3.22}$$

where η is the actual local viscosity, $\dot{\varepsilon}_{\mathrm{II}}$ the second invariant of the strain rate, and V denotes the volume over which the viscosity is averaged. *Christensen* (1984) found that $\langle\langle\eta\rangle\rangle_2$ overemphasized regions with very high strain rates in his models, and empirically determined that $\langle\langle\eta\rangle\rangle_1$ performed better in the computation of an effective Rayleigh number in most cases. Since these conclusions were not definitive, we study both measures.

The strain rates and state of stress within plates and subducting slabs are also determined. The surface strain rates are compared to the Global Strain Rate Mapping Project (GSRMP) model from *Kreemer et al*. (2003). This strain rate model is derived from GPS velocities, Quaternary fault slip rates, and focal mechanisms of shallow earthquakes. The strain rate in the shallow and deeper slabs are also compared to minimum average slab strain rate constraints, based on minimum seismic moment estimates from seismicity in the period 1904–1974 (*Bevis*, 1988), 1977–1992 (*Holt*, 1995), or 1977–1994 (*Nothard et al.*, 1996).

The state of stress in plates and slabs resulting from the numerical models is studied by decomposing the stress tensor in its principal components, where the first and third eigenvectors correspond to the tensional and compressional axes, respectively. The stress regime in overriding plates can then be compared to observed regimes (*Jarrard*, 1986; *Lallemand et al.*, 2005). These studies characterize the regimes using stress and strain indicators such as focal mechanisms, Quaternary faults and folds, volcanic vent alignments, overcoring, and the presence of back-arc spreading. In the subducting slabs, the state of stress is compared to stress orientations determined from focal mechanisms (*Isacks and Molnar*, 1971; *Alpert et al.*,

2010). Also individual centroid moment tensor (CMT) stress axes are used to test the model stress in subducting slabs, by interpolating the model stress field onto the CMT locations and computing a misfit angle between the compression axis of each focal mechanism and the interpolated model compression axis. How the averaged stress regime misfit in a subducting slab varies as function of rheology is also determined.

Finally, we assess the models using the entire suite of constraints available to us: global and regional plate motions, plateness, net rotation, strain rates, and the state of stress in plates and slabs. The models are then scored, permitting us to judge which combinations of yield stress and stress exponent best fit this set of constraints.

3.4 Results

3.4.1 Introduction

We have computed a set of global instantaneous models of mantle convection with plates, with the goal to discern effects of rheology on plate motions, plateness, strain rates, state of stress, and slab dynamics. The nonlinearity of the upper mantle rheology, in the form of the stress exponent n, is varied between 2 and 3.75, ranging below and above the experimentally accepted range, [3, 3.5] (*Karato and Wu*, 1993; *Hirth and Kohlstedt*, 2003) (Table 3.3). The strength of plates and slabs represented by the yield stress σ_y is chosen in a range between 50 MPa and 1200 MPa, such that it covers the values based on laboratory studies and geodynamic models (*Ranalli*, 1995; *Kohlstedt et al.*, 1995; *Billen and Hirth*, 2007). Finally, the scaling between the seismic velocity anomalies in tomography inversions to temperature anomalies ω is varied between 0 (no lower mantle structure) and 0.25 (*Karato and Karki*, 2001; *Forte*, 2007). Outcomes of these models are interior and surface flow velocities, state of stress, strain

rate, and viscosity.

Model	Case	Yield stress σ_y	Stress exponent n	LM tomo scaling ω
run97	1	50 MPa	3.0	0.1
run104	2	100 MPa	3.0	0.1
run98	3	200 MPa	3.0	0.1
run99	4	400 MPa	3.0	0.1
run107	5	800 MPa	3.0	0.1
run100	6	100 MPa	2.0	0.1
run102	7	100 MPa	3.25	0.1
run101	8	100 MPa	3.5	0.1
run105	9	400 MPa	3.5	0.1
run106	10	800 MPa	3.5	0.1
run108	11	1200 MPa	3.5	0.1
run109	12	1200 MPa	3.75	0.1
run110	13	100 MPa	3.0	0.0
run94	14	100 MPa	3.0	0.25

Table 3.3. Varied global rheology parameters.

A set of 14 cross-sections in 6 regions is selected for detailed study (Figure 3.1). These regions (the Aleutians, Japan, Marianas, Tonga, Scotia, and South America areas) were selected because they represent subduction zones spanning regions with fundamentally different coupling between plates (*Uyeda and Kanamori*, 1979). Several of these regions display complex plate motions and microplate kinematics with and without trench rollback (Tonga, Marianas, Scotia). This degree of complexity in plate boundaries is present in our models, and hence the microplate behavior provides excellent model tests. Studying such a large set of cross-sections and areas in detail allows us to consider a wide range of slab and plate geometries with respect to variation in input properties.

A typical viscosity field resulting from a numerical model shows the resulting broad-scale variations in viscosity and zones of yielding, as well as the imposed "faults" (Figure 3.2). Narrow low-viscosity features with a value of 10^{18} Pa s are the weak zones defining plate boundaries. The weak zones in subduction zones have a dip which varies both laterally and

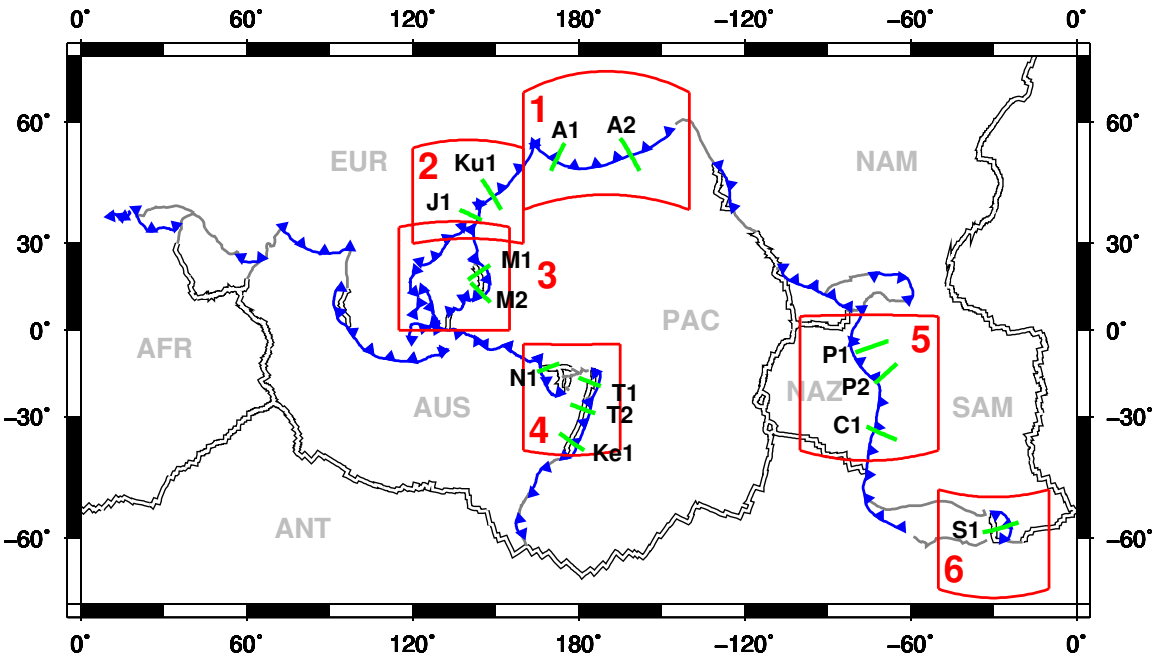

Figure 3.1. Map of regions and cross-sections selected for detailed analysis. Cross-section labels: A: Aleutians; C: Chile; J: Japan; Ke: Kermadec; Ku: Kurile; M: Marianas; N: New Hebrides; P: Peru; S: Sandwich; T: Tonga. Region labels: 1: Aleutians; 2: Japan; 3: Marianas; 4: Tonga; 5: South America; 6: Scotia. Plate labels: AFR: Africa; ANT: Antarctica; AUS: Australia; EUR: Eurasia; NAM: North America; NAZ: Nazca; PAC: Pacific; SAM: South America.

with depth, while those at ridges and fracture zones are vertical (Figure 3.2b). The viscosity in plate interiors is predominantly governed by the maximum cutoff value of 10^{24} Pa s, due to low internal deformation and low intra-plate strain rates. Around plate boundaries, this results in several orders of magnitude change in viscosity over short distances, necessitating the 1 km resolution around weak zones (Figure 3.2c). This refinement in the mesh is facilitated through the viscosity gradient term in the error estimator (equation (3.3)), and occurs during the iterative solution of the Stokes equation. Elsewhere in the plates and slabs, the resolution is 2–10 km. In the upper mantle, the cold and therefore stiff slabs are defined by sharp gradients in viscosity and temperature with respect to the surrounding upper mantle with lower viscosity. The longer wavelength structures in the lower mantle have much smoother gradients, being derived from a smooth tomography model. Here the resolution is on the order of 80–150

km. In addition, the effect of nonlinearity on the upper mantle viscosity is evident in mantle wedges: the high velocity corner flow causes strain rates to be high, giving rise to a low viscosity governed by dislocation creep. The effect of strain rate weakening is also visible in the hinges of subducting plates, where the bending of cold plates into the mantle results in yielding.

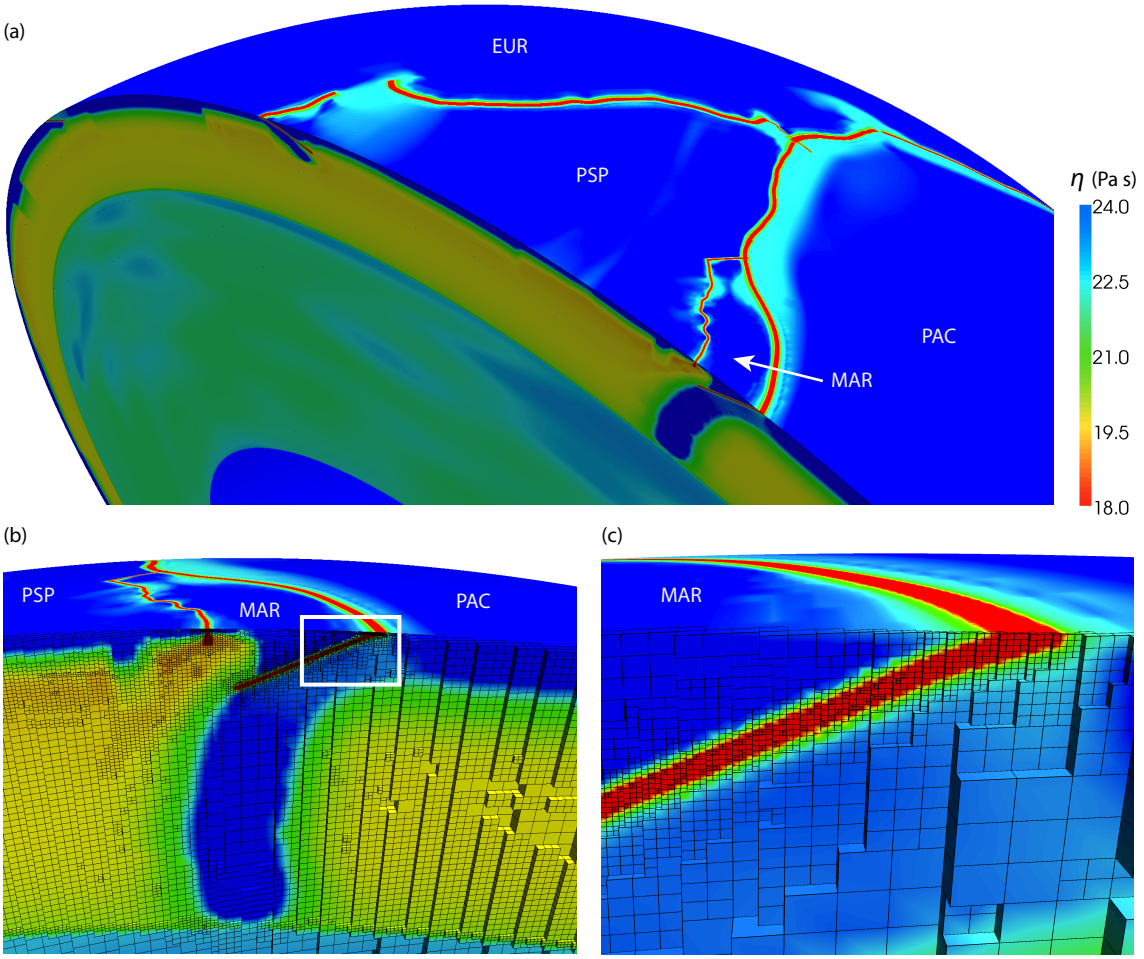

Figure 3.2. (a) Cutout showing viscosity in a global model with stress exponent $n = 3.0$ and yield stress $\sigma_y = 100$ MPa (Case 2) through the Marianas and Philippines. (b) Zoom-in on viscosity of the Marianas subduction zone, showing the mesh. (c) Further zoom-in on the hinge of the Marianas slab, as denoted by the white box in panel (b). Plate labels are: EUR: Eurasia; MAR: Marianas; PAC: Pacific; PSP: Philippine Sea.

3.4.2 Plate Motions and Plateness

3.4.2.1 Global Plate Motions

Global plate motions constitute a first-order test of dynamic convection models with plates, because the plate behavior is only Earth-like for a limited range of parameters in the constitutive relations. If plates are too stiff, they may move too slowly compared to observed motions, although they may satisfy plateness constraints. On the other hand, plates which are too weak may move too fast while exhibiting excessive internal deformation, as indicated through measures of plateness. Here we investigate the fine balance between these end member scenarios.

In general, the global plate motion directions match the NNR_NUVEL1A plate motion model well (*DeMets et al.*, 1994), but the velocity magnitudes are a strong function of the rheology. An increase in yield stress from 100 (Case 2, Figure 3.3a) to 800 MPa (Case 5, Figure 3.3b) results in a decrease in magnitude of the predicted model velocity in both subducting and overriding plates, while generally not significantly altering the directions of plate motions. This velocity reduction is strongest in the subducting plates (Pacific, Australia, Cocos), as the increase in yield stress allows for less yielding in the slab hinges, limiting the ability of the plate to subduct. An increase in stress exponent from 3.0 to 3.5, while the yield stress remains constant at 800 MPa (Case 10), results in a significant speedup of all plates due to stronger strain rate weakening in the upper mantle and hence lower viscosity below the plates and in the hinge zones (compare Figure 3.3b to c). A further increase in stress exponent from 3.5 to 3.75, even as the yield stress increases from 800 to 1200 MPa (Case 12, Figure 3.3d), causes the plates to further speed up. Evidently, the weakening induced by the increase of the stress exponent overwhelms the strengthening caused by the increase in yield stress. Now, with the larger stress exponent and yield stress, significant changes in plate motion direction can be

seen for the Nazca and South America plates (compare Figure 3.3c to d). It could be argued that the plate motions in the South America region experience more effect from changes in yield stress and stress exponent than elsewhere, due to the stronger plate boundary coupling around Peru.

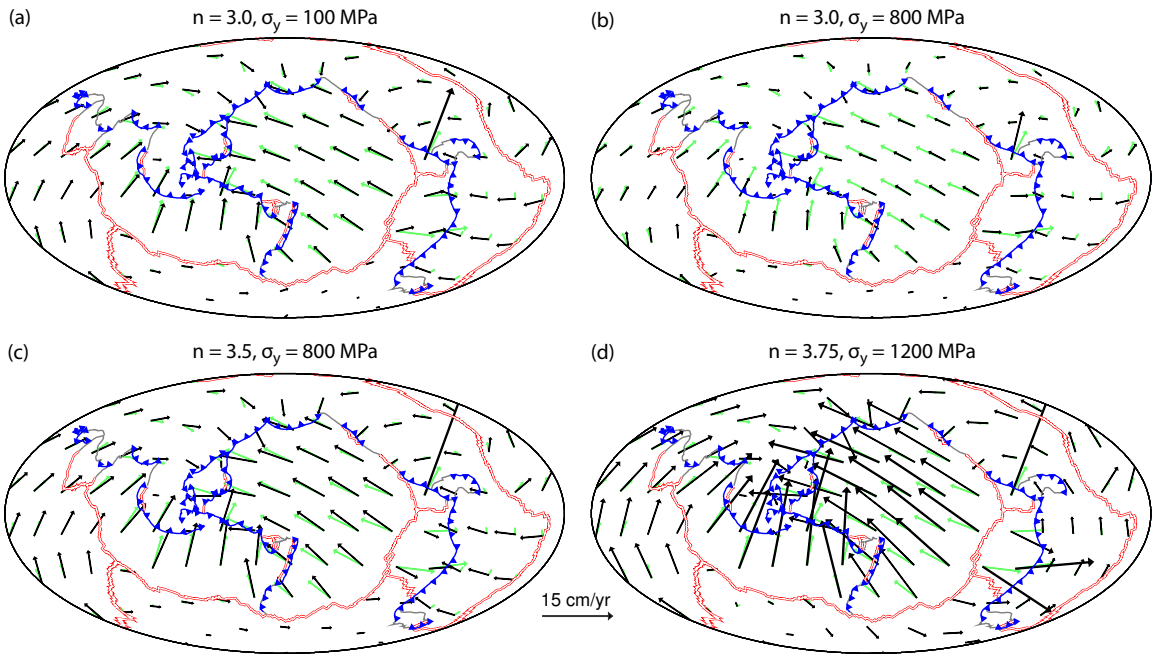

Figure 3.3. Global plate motions with variation of yield stress and stress exponent. Known plate motions in a no-net-rotation frame (NNR_NUVEL1A) in green are compared against modeled plate motions in black. (a) Case 2: $\sigma_y = 100$ MPa and $n = 3.0$; (b) Case 5: $\sigma_y = 800$ MPa, $n = 3.0$; (c) Case 10: $\sigma_y = 800$ MPa, $n = 3.5$; (d) Case 12: $\sigma_y = 1200$ MPa, $n = 3.75$.

The sensitivity of plate motion direction and speed to the stress exponent and yield stress is explored for several plates and for a global average. The angle misfit, α, is defined as the average clockwise angle between the model plate velocity and the NNR_NUVEL1A velocity (equation (3.17)); a value of 0 denotes a perfect angle fit. The normalized velocity is the average plate speed divided by the NNR_NUVEL1A speed (equation (3.18)); a value of 1 indicates a plate moving at the correct speed. The global average is a surface-weighted average of the nine largest plates (AFR, ANT, AUS, EUR, IND, NAM, NAZ, PAC, SAM). The global averaged

angle misfit is the average of absolute misfit values. It is noteworthy that the best angle fit occurs for different combinations of the stress exponent and yield stress for different plates (Figure 3.5a–c), suggesting that the misfits are governed by regional characteristics such as geometry and interplate coupling, rather than rheology. In contrast, the sensitivity of the normalized velocity magnitude to variations in parameters is consistent between each plate and the global average (Figure 3.5d–f). There is a significant dependence on the stress exponent for all yield stresses used, indicating that nonlinear strain rate weakening is dominant in determining plate speeds. The strain rate weakening occurs in the hinge of the subducting slab (Figure 3.2), influencing the ease with which the slab subducts. It also occurs in the asthenosphere, governing the amount of decoupling between the plates and underlying mantle. The strong sensitivity of plate speeds to rheology provides us with combinations of stress exponent and yield stress that result in acceptable plate motions, mostly with a stress exponent between 3 and 3.25. Only models with weaker plates and slabs (i.e., with a yield stress below a threshold of around 200 MPa) display dependence on yield stress, and require significantly lower stress exponents.

There are two domains in the space of yield stress (σ_y) and stress exponent (n) evident in Figure 3.5 (and subsequent similar representations), which we illustrate with a schematic (Figure 3.4). In domain I, both the yield stress and the stress exponent have a strong influence on the resultant quantity, e.g., plate velocity magnitude. This behavior is observed consistently below a yield stress of 200 MPa. In domain II, the yield stress has little or no bearing on the result, and only the stress exponent governs the outcome. This occurs for yield stresses above 200 MPa. The transition between the two domains is governed by the convective stress σ_c, determined by the bulk viscosity and integrated buoyancy in the system. Yield stresses below this transition stress limit the strength of the material and hence have an effect on plate

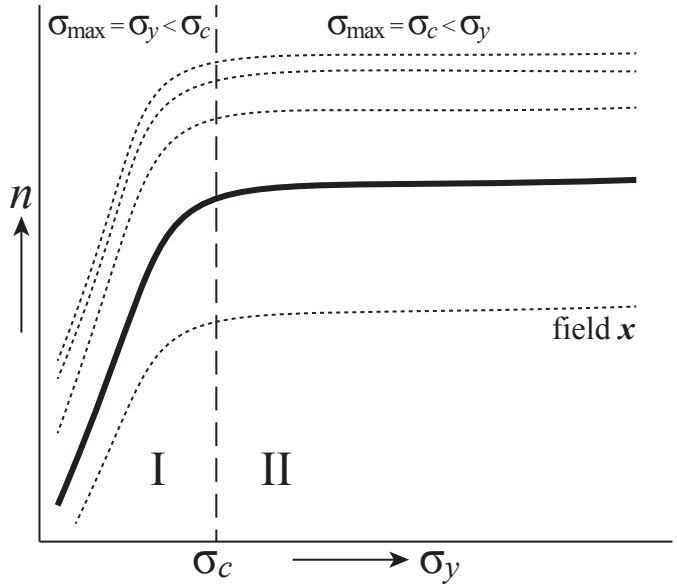

Figure 3.4. Schematic of the behavior of a resulting quantity as function of (σ_y, n). Contour lines of the field x are indicated; the two domains are denoted with I and II. The convective stress is σ_c.

motions and other resulting quantities: $\sigma_{\max} = \sigma_y < \sigma_c$. When yield stresses exceed the transition stress, the ubiquitous convective stress determines bulk ambient stresses, as mantle flow redistributes stress throughout the domain: $\sigma_{\max} = \sigma_c < \sigma_y$. Only in localized areas are the stresses higher such that the yield stress will have an effect (for example in the interior of cold slabs). There is a gradual bend in the contours with increasing yield stress, as smaller and smaller volumes contain stresses that exceed the yield stress. In both domains, gradients in the resulting quantity are stronger for larger stress exponent values (denoted by the decreased contour spacing, Figure 3.4), as observed for the plate motions in Figure 3.5d–f. This illustrates the highly nonlinear response of the system to rheology.

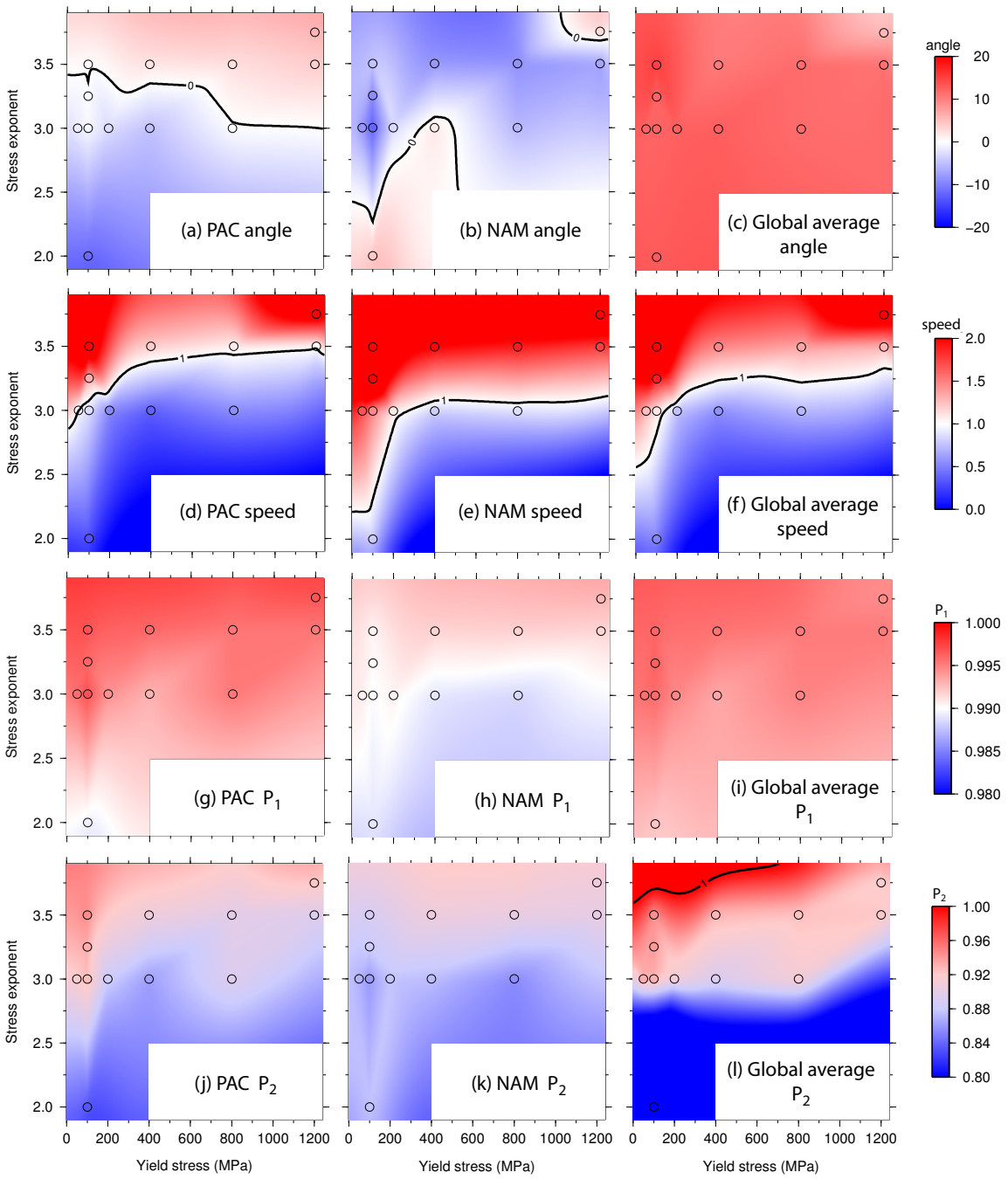

Figure 3.5. (a)–(c): Angle misfit; (d)–(f): plate speed normalized by observed speed in a no-net-rotation reference frame; (g)–(i): plateness P_1; (j)–(l): plateness P_2. From left to right: Pacific (PAC), North America (NAM), global average weighted by surface area. The circles denote the models run in this study; the background shows the field interpolated from these values. Note that for the global average angle (c) the absolute value of the misfit angle is used.

3.4.2.2 Plateness

Plateness is a measure of plate rigidity and coherence and is strongly influenced by the non-linearity in the rheology. We use two measures of plateness. P_1 relates to the angle difference between the local plate velocity and the velocity according to the best fitting pole for the entire plate. P_2 describes the norm of the vector difference between the two velocities. An increase in yield stress (100 MPa to 800 MPa, while n remains constant at 3.0; Case 2 and 5, respectively) results in smaller plateness P_2 for the Pacific plate, especially around the plate boundaries (Figure 3.6a and b). Also, the rotation poles for different parts of the Pacific are more broadly dispersed, indicating larger differential rotation and internal deformation. With less yielding permitted, the Pacific plate becomes more "stuck" to the neighbouring plates. Case 10 (Figure 3.6c) has more localized deformation with an increase in stress exponent from 3.0 to 3.5 as the yield stress remains a constant 800 MPa, as is indicated by the narrower areas with low plateness. An even higher stress exponent and yield stress allows for a stiffer plate with a high plateness (respectively 3.75 and 1200 MPa, Case 12, Figure 3.6d). The low P_2 areas around the plate edges have almost entirely disappeared, except for the southwest corner. Also, the Pacific plate is moving more according to a single rotation pole but with significantly higher speed than in the other models, indicated by the closer clustering and larger magnitude of the rotation poles for different sections of the plate.

The integration of plateness over multiple plates allows some discrimination between model outcomes P_1 and P_2 (Figure 3.5g–l). Plateness P_1 varies from plate to plate, but in general a higher stress exponent leads to a higher plateness in response to stronger localization of plate boundary deformation. The plateness decreases somewhat for higher yield stress, but this effect is much weaker than that of the stress exponent. The integrated plateness for PAC is lower than that of the global average: Presumably, the larger the plate, the more diffi-

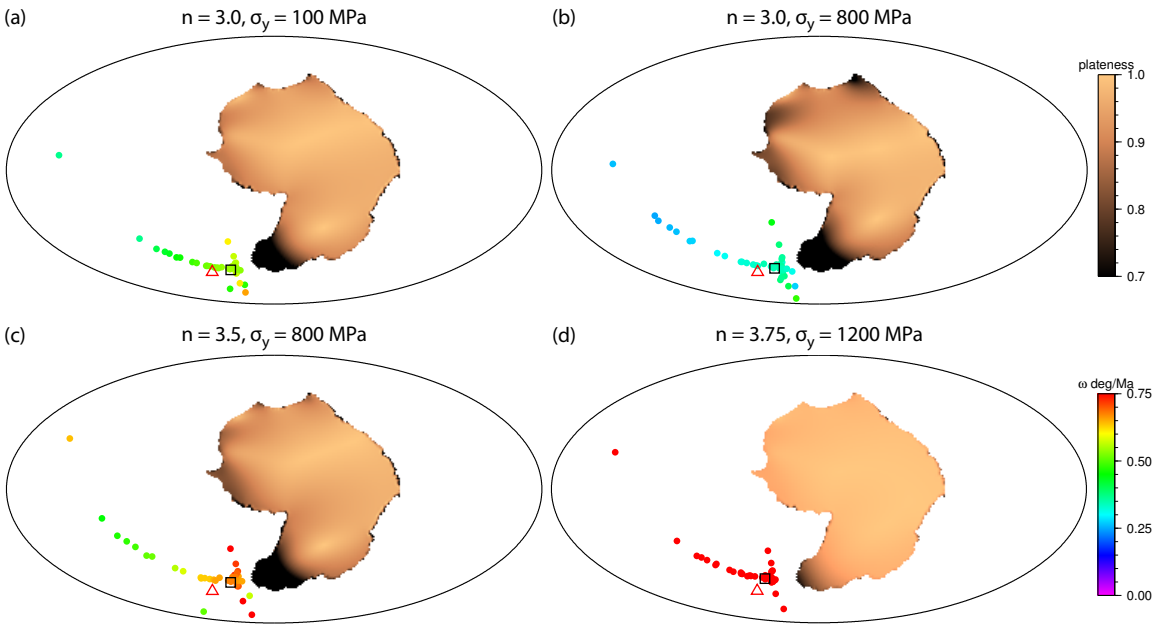

Figure 3.6. Pacific plateness with variation in yield stress and stress exponent. The color of the dots denotes the magnitude of the rotation pole for different plate sampling caps with a radius of 20°. The magnitude of the rotation pole for PAC in the NNR_NUVEL1A model is 0.64°/Ma. Red triangle: NNR_NUVEL1A rotation pole. Black square: Rhea average rotation pole. The background color is the plateness P_2, the RMS difference between Rhea velocities and the best fitting pole. (a) Case 2: $\sigma_y = 100$ MPa and $n = 3.0$; (b) Case 5: $\sigma_y = 800$ MPa, $n = 3.0$; (c) Case 10: $\sigma_y = 800$ MPa, $n = 3.5$; (d) Case 12: $\sigma_y = 1200$ MPa, $n = 3.75$.

cult it is to ensure little internal deformation and therefore high plateness. Plateness P_2 shows patterns similar to P_1. The sensitivity of P_2 to changes in rheology is larger, due to the fact that differences between the local velocity magnitude and the velocity magnitude from the best fitting pole is also taken into account, rather than just the angle difference, as for P_1. Hence we found P_2 to be more diagnostic of the amount of plate deformation.

3.4.2.3 Comparison to Hotspot Reference Frame

Plate motions are compared in different reference frames, namely the no-net-rotation frame (NNR_NUVEL1A model, *DeMets et al.* (1994)) and the hotspot frame (HS3_NUVEL1A, (*Gripp and Gordon*, 2002)). The difference in plate motions between the two reference models in,

e.g., the Pacific is significant, both in direction and magnitude (Figure 3.7a and b); the fit of the Rhea plate motions is much worse for the HS3_NUVEL1A model than for the NNR_NUVEL1A model.

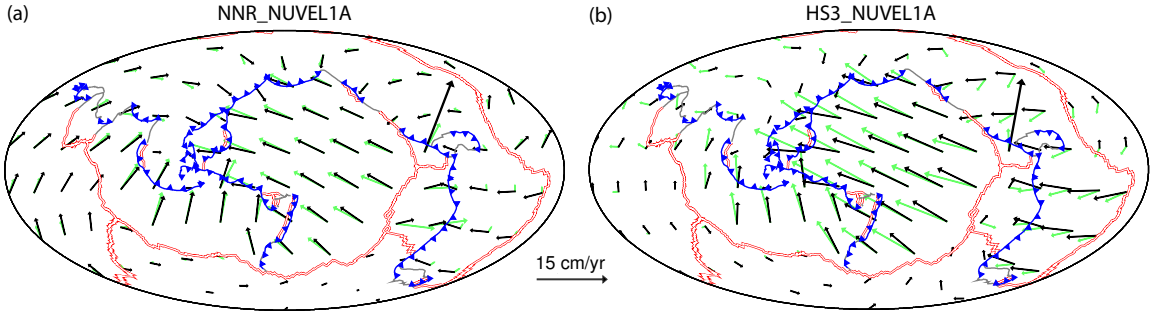

Figure 3.7. (a) Plate motions in NNR reference frame (black arrows), compared to NNR_NUVEL1A (green arrows), for Case 2. (b) Plate motions in hotspot reference frame (black), compared to HS3_NUVEL1A (green).

To assess plate motions in a hotspot reference frame, the total rotation of the lower mantle is subtracted from the surface velocity field. This lower mantle rotation is affected by the mantle bulk viscosity and by the buoyancy field present in the lower mantle, as is further explored below (Section 3.2.5). Consequently, any change in lower mantle flow will result in a different surface velocity pattern in the hotspot reference frame, even if the surface velocities were to stay constant in a no-net-rotation reference frame. This makes comparisons between models with different rheology parameters more difficult, since we are assessing the combined effect of the lower mantle rotation and surface rotation. Therefore, this study mainly focuses on results in the no-net-rotation reference frame. Additionally, the platenesses P_1 and P_2 are not invariant under spherical coordinate transformations, since they are based on vector norms in a Euclidean space. These vector norms will be minimum in a no-net-rotation frame of reference, and therefore a NNR model will always yield a larger plateness than a model with non-zero net rotation, such as the hotspot reference frame. This difference in plateness

does not reflect a change in the amount of plate deformation, and consequently a comparison of plateness between different reference frames is not meaningful.

3.4.2.4 Net Surface Rotation

The magnitude of the estimated surface net rotation varies significantly between different plate models (Table 3.4). For instance, the HS3 model (*Gripp and Gordon*, 2002) has a rotation rate almost four times that of T10 (*Torsvik et al.*, 2010), 0.44°/My compared to 0.13°/My. The former is based on current-day plate motions, whereas the latter results from plate reconstructions averaged over the past 5 My. Previous numerical models (*Becker*, 2006; *Zhong*, 2001; *Ricard et al.*, 1991) typically did not predict strong net rotation, usually less than 0.15°/My. The net rotation in the numerical models presented here shows significantly more variation than in the plate motion models described in the literature (Types H and A in Table 3.4), suggesting that this quantity can be used as a constraint on rheology. One reason we show a greater range of net rotation is that we include models that do not fit plate motions well (e.g., Case 12, with $n = 3.75$ and $\sigma_y = 1200$ MPa). The net rotation only mildly depends on the reference frame in our models: removal of the lower mantle rotation results in a small increase in the net surface rotation (Table 3.4). This indicates that surface rotation is dominant over lower mantle rotation in our models.

The amount of net surface rotation strongly depends on the stress exponent (Figure 3.9). An increase in stress exponent causes all velocities in the upper mantle and plates to increase (indicated by the increase of the L_2 norm of velocity in the entire model volume), which directly influences the amount of rotation of the surface with respect to the deeper mantle. Even though the stress exponent only affects the nonlinear component of the upper mantle viscosity, the velocities in the entire domain are increased, including in the lower mantle,

Model	Type	Parameters	Pole lat (°N)	Pole lon (°E)	Rotation rate (°/My)	Reference
T10	H		-68	132	0.13	*Torsvik et al.* (2010)
ON05	H		-46	92	0.19	*O'Neill et al.* (2005)
SB04	H		-40	38	0.17	*Steinberger et al.* (2004)
HS3	H		-56	70	0.44	*Gripp and Gordon* (2002)
T22	H		-62	88	0.14	*Wang and Wang* (2001)
R91h	H		-56	84	0.15	*Ricard et al.* (1991)
HS2	H		-49	65	0.33	*Gripp and Gordon* (1990)
GJ86	H		-30	33	0.11	*Gordon and Jurdy* (1986)
K09	A		-58	63	0.21	*Kreemer* (2009)
B06a	N		-46	71	0.08	*Becker* (2006)
B06b	N		-45	94	0.13	*Becker* (2006)
BSK	N		-63	76	0.06	*Becker* (2006)
Z01	N		-42	103	0.09	*Zhong* (2001)
R91m	N		-47	93	0.15	*Ricard et al.* (1991)
Case 2	N	$n = 3.0$ $\sigma_y = 100$ MPa	-86	309	0.13	This study
Case 2–LM	N		-89	251	0.14	
Case 10	N	$n = 3.5$ $\sigma_y = 800$ MPa	-69	89	0.29	This study
Case 10–LM	N		-73	94	0.32	
Case 12	N	$n = 3.75$ $\sigma_y = 1200$ MPa	-53	97	0.80	This study
Case 12–LM	N		-60	99	0.84	

Table 3.4. Compilation of net rotation from several plate motion models and from numerical models. Types: H: hotspot plate models; A: anisotropic constraints; N: numerical flow models. For each of the Cases 2, 10, and 12, two results are given. The first is the regular net rotation of the surface, the second (with the suffix "–LM") has the lower mantle rotation removed for comparison with hotspot models.

indicating that there is a strong coupling of flow between the upper and lower mantle. For an increase in stress exponent n from 3.0 to 3.5, plate velocities increase by a factor ~ 2.5 (Figure 3.5f), but the net rotation becomes stronger by a factor of ~ 5.0 (Figure 3.9c). This increase should indeed be around twice that of the velocity, since the upper and lower mantle flow have to be more or less opposite to each other, and hence the differential rotation doubles.

Changes in rheology affect the bulk viscosity, which can be seen through two measures of integrated viscosity: $\langle\langle\eta\rangle\rangle_1$ based on viscosity and strain rate (equation (3.21)), and $\langle\langle\eta\rangle\rangle_2$ based on viscosity and the square of the strain rate (equation (3.22)). Both measures of the

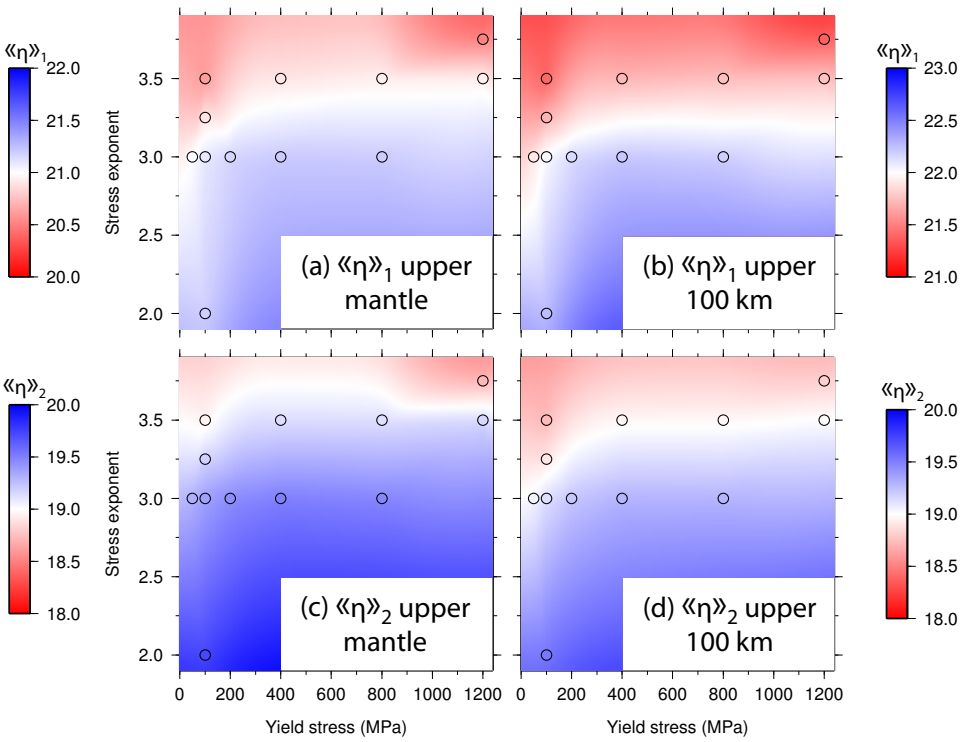

Figure 3.8. (a) Integrated viscosity $\langle\langle\eta\rangle\rangle_1$ in the upper mantle. (b) $\langle\langle\eta\rangle\rangle_1$ in the upper 100 km. (c) Integrated viscosity $\langle\langle\eta\rangle\rangle_2$ in the upper mantle. (d) $\langle\langle\eta\rangle\rangle_2$ in the upper 100 km.

bulk viscosity in the upper mantle decrease with increasing stress exponent (Figure 3.8a-b). For both the upper mantle and for the top 100 km, $\langle\langle\eta\rangle\rangle_2$ varies less than $\langle\langle\eta\rangle\rangle_1$, and is more similar to the change in velocity, and therefore more representative of model dynamics. In the $\langle\langle\eta\rangle\rangle_2$ measure, the square of the strain rate is used; hence localized variations in viscosity resulting from nonlinearity are taken into account more locally, and have a smaller effect on the bulk viscosity than in $\langle\langle\eta\rangle\rangle_1$.

The yield stress has no significant bearing on the net rotation, since it does not affect the viscosity in the mantle surrounding the slab. Only a narrow region in the (σ_y, n) parameter space fits the net rotation constraint using the most recent analysis of *Torsvik et al.* (2010), with a stress exponent of ~ 3.0 (Figure 3.9c). The yield stress also has little effect on the bulk viscosity, especially for larger yield stresses. For both the net rotation and the bulk viscosity, we discern the same pattern in (σ_y, n) space as described above (Figure 3.4).

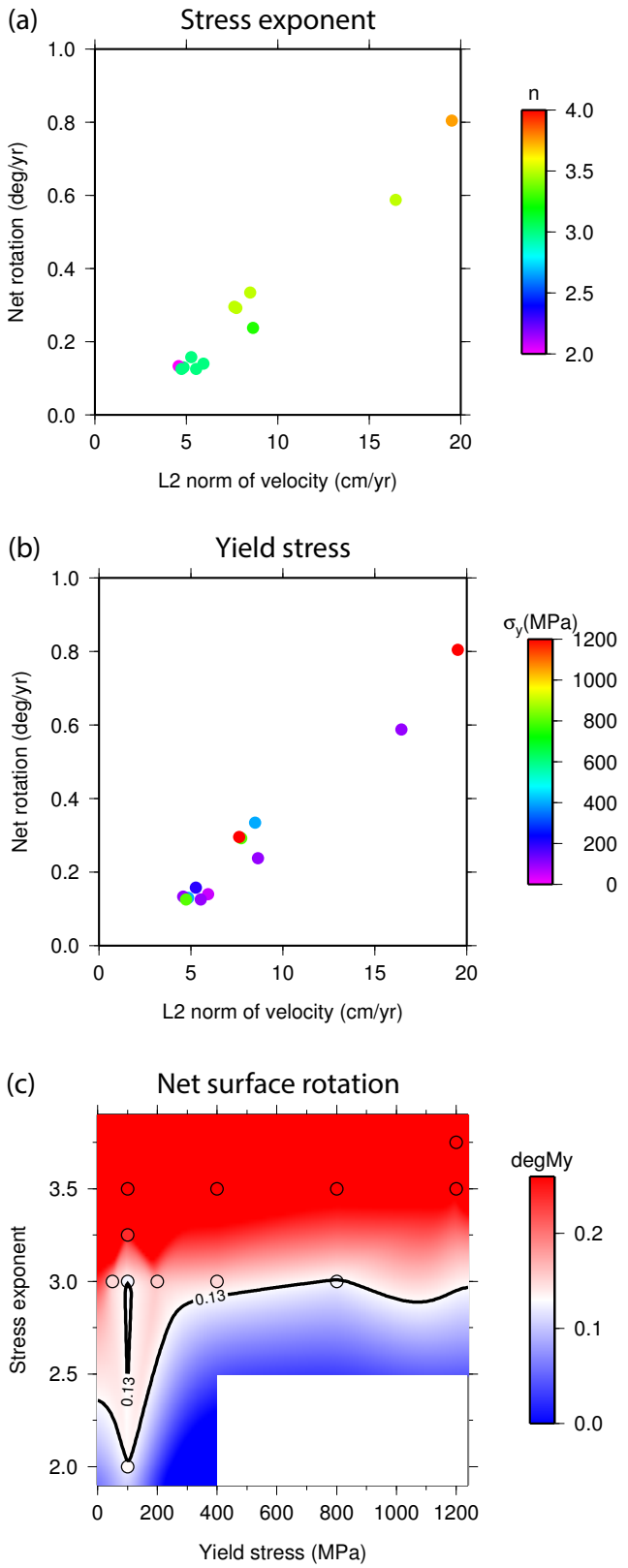

Figure 3.9. (a) Resulting net rotation and volume L_2 norm of velocity, color coded by stress exponent. (b) Same quantity, color coded by yield stress. (c) Net surface rotation as function of stress exponent and yield stress.

3.4.2.5 Lower Mantle Structure

The lateral viscosity structure of the lower mantle is a function of the conversion factor from seismic velocity to temperature anomalies, ω, through the temperature dependence of the viscosity. Stronger negative temperature anomalies in the lower mantle result in structures with higher viscosities. In models with a purely depth-dependent viscosity, this additional negative buoyancy in the deep slabs would speed up plate motions (*Becker and O'Connell*, 2001). This effect can be mitigated by the presence of a strong viscosity gradient across the 660 km phase transition, which impedes flow across the transition zone (*Conrad and Lithgow-Bertelloni*, 2002). In the nonlinear temperature- and depth-dependent models presented here, the influence of lower mantle structure strength on plate motions is not nearly as straightfoward.

Increasing the conversion factor from $\omega = 0$ (no lateral temperature variation in the lower mantle, Case 13) to $\omega = 0.1$ and to 0.25 (strong temperature anomalies in the lower mantle, Cases 2 and 14, respectively) causes a general increase in plate speeds due to the addition of negative buoyancy in structures with low temperature and therefore high viscosity, promoting overall flow in the mantle and plates (Figure 3.10b, e, and h). However, some plates slow down significantly, such as the Pacific and Australia, where slabs connect to large-wavelength anomalies of high viscosity in the lower mantle on the western side of the Pacific (Figure 3.10a, d, and g). Also the Nazca plate slows down, as the Nazca slab is connected to the high-viscosity structure beneath South America. Overriding plates with no attached subducting slabs, such as North and South America, Antarctica, and Africa, are only affected by the increased amount of negative buoyancy in the lower mantle, and therefore they speed up. The difference in behavior between the Nazca and South America plates is visible in the viscosity and velocity cross-sections through the South America trench in Figure 3.10c, f, and i, where Nazca on the left slows down, and South America on the right speeds up with a

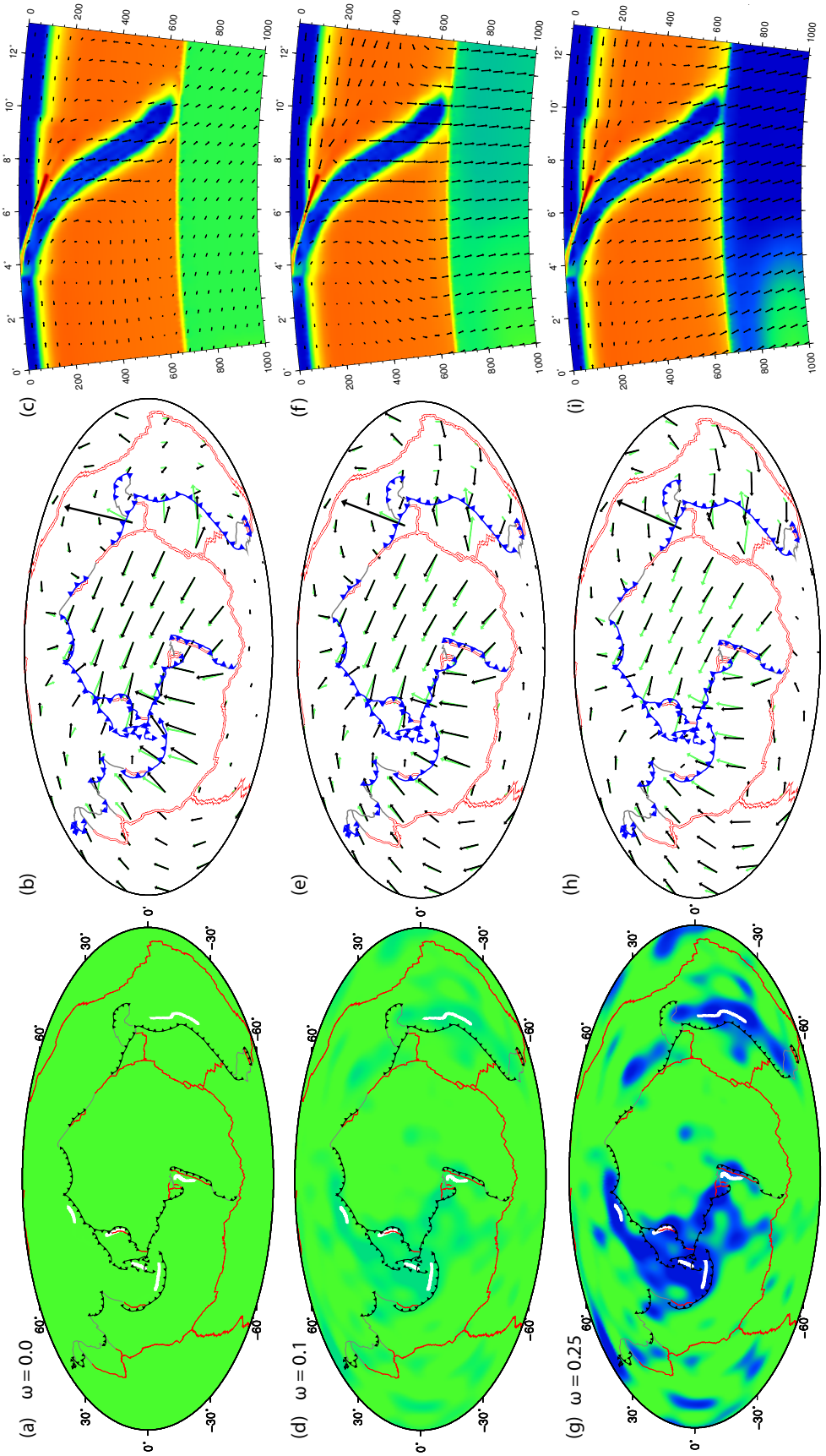

Figure 3.10. Top row: Case 13, lower mantle tomography conversion factor $\omega = 0.0$; Center row: Case 2 with factor $\omega = 0.1$; Bottom row: Case 14, factor $\omega = 0.25$. Left column: Viscosity field at 700 km depth (color map), with slab contours at 600 km depth plotted in white contours. The contours are defined by nondimensional temperature $T = 0.55$. Center column: Global plate motions, NNR_NUVEL1A plate motions are plotted in green, Rhea velocities in black. Right column: Cross-sections through Peru (for location see P2, Figure 3.1). The background is viscosity; the vectors show velocity in a no-net-rotation reference frame.

generally faster flow in the mantle. The Cocos and Eurasia plate speeds do not increase. The Cocos plate subducts beneath North America, but the slab does not reach the high viscosity structure in the lower mantle underneath (e.g. Figure 3.10a, d, g) and is therefore not slowed down by the increase in conversion factor.

The bulk lower mantle viscosity $\langle\langle\eta\rangle\rangle_2$ increases from 1.1 $\times$ 10^{22} to 1.3 $\times$ 10^{22} and to 1.7 $\times$ 10^{22} Pa s for, respectively, cases with conversion factor $\omega = 0$, 0.1, and 0.25. This partially mitigates the effect of increase in negative buoyancy on the flow, which could explain why the speedup of South America, North America, and Africa from $\omega = 0.0$ to 0.1 is more significant than from $\omega = 0.1$ to 0.25.

3.4.3 Strain Rates

3.4.3.1 Surface Strain Rates

Surface strain rate is a manifestation of deformation of plates and their boundaries. These strain rates are directly related to the nonlinearity of the viscosity, which allows localization of deformation, visible as the narrow bands of high strain rates at plate boundaries (Figure 3.11). Increasing the yield stress from 100 to 800 MPa with n constant at 3.0 (Cases 2 and 5) decreases strain rates in slab hinges where yielding occurs, and in turn decreasing the velocity of both large and small plates (Figure 3.11a–c compared to d–f). However, increasing the stress exponent from 3.0 to 3.75 has a significantly larger effect than the change in yield stress from 800 MPa to 1200 MPa: strain rates increase significantly throughout the plates including their boundaries (Case 12, Figure 3.11 g–i).

Modeled output of the second invariant of the strain rate at the surface is compared to surface strain rate maps from the Global Strain Rate Mapping Project (Figure 3.11j–l, *Kreemer et al*. (2003)). A striking difference is the width and magnitude of the high strain rate areas

around plate boundaries in the GSRMP maps compared with the dynamic models which have substantially narrower zones of deformation. *Kreemer et al*. (2003) do not include microplates in their analysis, which locally results in anomalously high strain rates in overriding plates, whereas the dynamic models have these high strain rates in the hinges of subducting plates. In the GSRMP model, the microplates are considered part of diffuse plate boundaries, increasing the length scale of deformation. The grid size of $0.6° \times 0.5°$ used by *Kreemer et al*. (2003) would only allow at most a few elements across a microplate, wich is insufficient to resolve the differential velocity of the microplate with respect to the major plates. Aside from the shift from the overriding plates to subducting slab hinges, the high strain rate areas in the GSRMP maps correspond to the highest ones in the dynamic models, especially where there are sharp bends in the plate boundaries or where plate boundaries join. Examples are northern Tonga and New-Hebrides (Figure 3.11j) and the area north of the Marianas microplate (Figure 3.11l). The strain rates in the Sandwich plate in the GSRMP map (Figure 3.11k) are significantly lower than around the other microplates. Overall plate velocities in this area are smaller than in the other regions, with slower deformation and therefore a smaller strain rate. Although our model results also indicate generally lower strain rates in this area compared to other regions, the plate boundaries themselves exhibit orders of magnitude higher strain rates than shown in the GSRMP map. This is also consistent with the averaging of strain rates over larger length scales in the GSRMP model compared to our models.

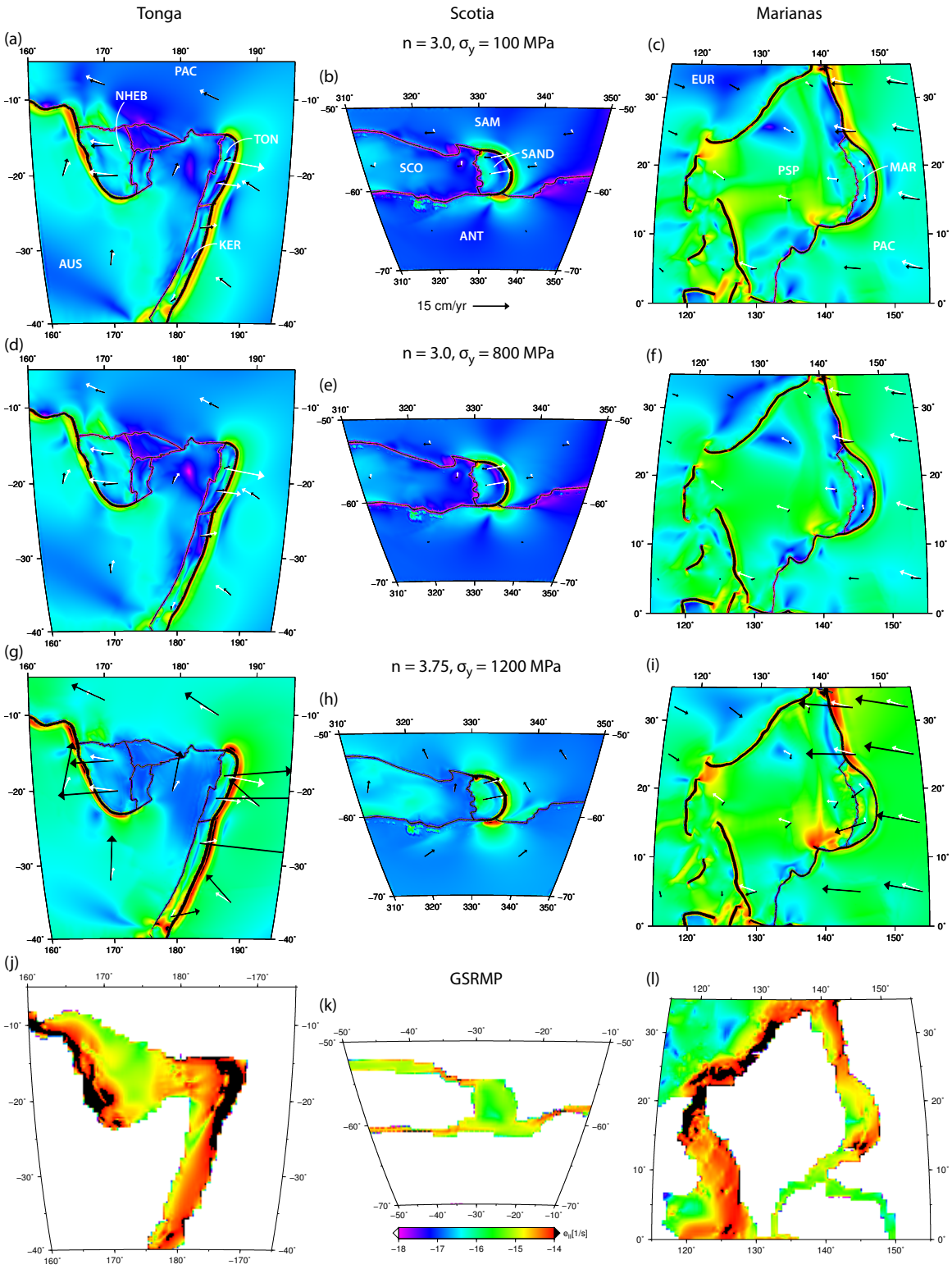

Figure 3.11. Comparison of surface strain rates. From left to right: Tonga, Scotia, Marianas. From top to bottom: Case 2, $\sigma_y = 100$ MPa and $n = 3.0$; Case 5, $\sigma_y = 800$ MPa, $n = 3.0$; Case 12, $\sigma_y = 1200$ MPa, $n = 3.75$; Global Strain Rate Map Project (*Kreemer et al.*, 2003). NNR_NUVEL1A plate motions are shown in white, Rhea no-net-rotation velocities in black; plotted on top of the second invariant of the strain rate tensor.

3.4.3.2 Slab Strain Rates

Estimates of seismic moment release by earthquakes in slabs provide a minimum constraint on actual strain rates within slabs (*Bevis*, 1988). The slabs deform at least at the rate implied by earthquakes. Any aseismic component of deformation is not represented by the earthquakes, hence these estimates give a minimum constraint on the strain rate in slabs. Shallow strain rates (between 75 and 175 km depth) are extracted in all studied subduction zone cross-sections (Figure 3.1), and compared to the minimum constraint of 10^{-15} s^{-1}, using earthquakes between 1904 and 1974 (*Bevis*, 1988). Additionally, we compare the average strain rate in the Tonga slab from 200 km depth downward, to the minimum estimate of 5×10^{-16} s^{-1} (*Bevis*, 1988; *Holt*, 1995; *Nothard et al.*, 1996).

The strain rates in slabs are a function of yield stress and stress exponent (Figure 3.12). Strain rates in slabs increase strongly with increase in stress exponent, and decrease with yield stress only in the low yield stress regime. For yield stresses higher than about 200 MPa, only the stress exponent has a strong effect on strain rate. This pattern is similar for all cross-sections; this uniformity suggests that rheology is of much more influence on strain rate in slabs than regional geometry, and again fits the pattern in (σ_y, n) space described by the schematic in Figure 3.4. The global shallow slab strain rate constraint provides a minimum stress exponent estimate of $\sim$ 3.0–3.5 for yield stresses $<$ 200 MPa, and slightly higher for $\sigma_y > 200$ MPa. The average strain rate within the Tonga slab is somewhat less sensitive to rheology, and allows a wider range of parameter choices than the global shallow average, with a minimum acceptable value of around 3.0. This is similar to the results found by *Alisic et al.* (2010), although in that study a much smaller parameter space was considered ($n = 3.0$, and $\sigma_y = \{50, 100, 200, 400\}$).

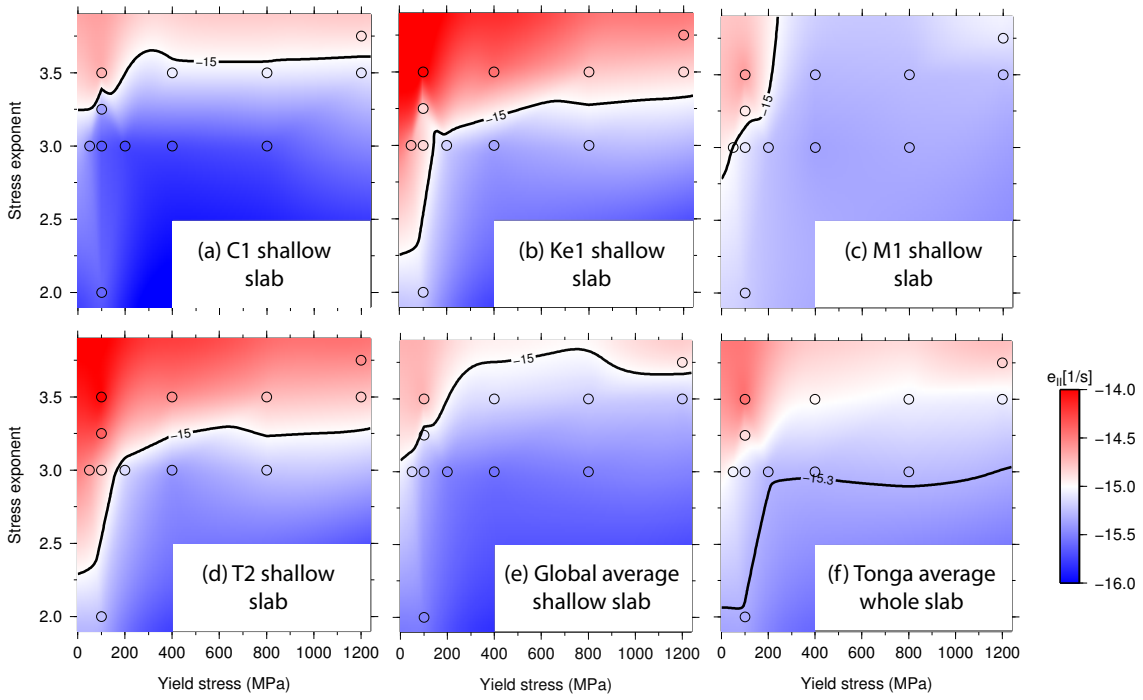

Figure 3.12. Global constraint for the strain rate in shallow slabs, and for the average Tonga slab. (a) Strain rates in the shallow part of the Chile cross-section, C1 in Figure 3.1; (b) Kermadec, Ke1; (c) Marianas, M1; (d) Tonga, T2; (e) Shallow slab average of the 14 cross-sections in Figure 3.1. Black contour: the global shallow slab strain rate constraint from seismicity of 10^{-15} s^{-1}, which must minimally be achieved. (f) The average strain rate in the Tonga slab below 200 km depth, with the region-specific minimum constraint of 5×10^{-16} s^{-1}.

3.4.4 State of Stress

3.4.4.1 Stress Drop

The stress drop estimates for large moment magnitude deep earthquakes form a lower limit of the stress that the slab must sustain. The 1994 Bolivia M_W 8.3 earthquake at 647 km depth experienced a minimum frictional stress of 55 MPa and a static stress drop of 114 MPa (*Kanamori et al.*, 1998). There are several other deep earthquakes with large predicted stress drop in the same region, including the 1970 Colombia M_W 8.3 event with a stress drop of 68 MPa (*Fukao and Kikuchi*, 1987; *Ruff*, 1999). Although these large stress drops are only measured in few cases, they imply that at least in the Bolivia-Colombia region stresses of

around 100 MPa are present. In *Alisic et al*. (2010) it was shown that global convection models can sustain such stresses at the depth of deep earthquakes.

3.4.4.2 Surface Stress Regime

The state of stress in overriding plates in the models is compared to stress regime observations (Figure 3.13). The state of stress at the surface indicates that the overriding plates in the Aleutians (Figure 3.13c), Peru and Chile (Figure 3.13e), Japan and the Kuriles (Figure 3.13f) are in compression, which is in agreement with observations in the literature (*Jarrard*, 1986; *Lallemand et al*., 2005). Similarly, the tensional regime in the overriding plate in the New Hebrides, Tonga, and Kermadec region (Figure 3.13d) is predicted correctly. However, the Marianas and Scotia areas (Figure 3.13a and b) show compression, which does not fit the observations. These are regions where the microplate motions in the numerical models do not correspond to inferred plate motions (see Figure 3.11 and Section 3.5.1). In the Marianas region, this is related to the Philippine Sea plate directly to the west of the Marianas microplate. Instead of moving westward and subducting under Okinawa and the Philippines, the plate is stuck as the subduction zones on the west of the plate are not contiguous, with gaps located at Taiwan and at Luzon in the Philippines orogen. Surface strain rates in the gaps are high ($\sim 10^{-15}$ to 10^{-14} s^{-1}), and the Philippine Sea plate is in strong southeast-northwest compression (see Figures 3.11c, f, i, and Figure 3.13b).

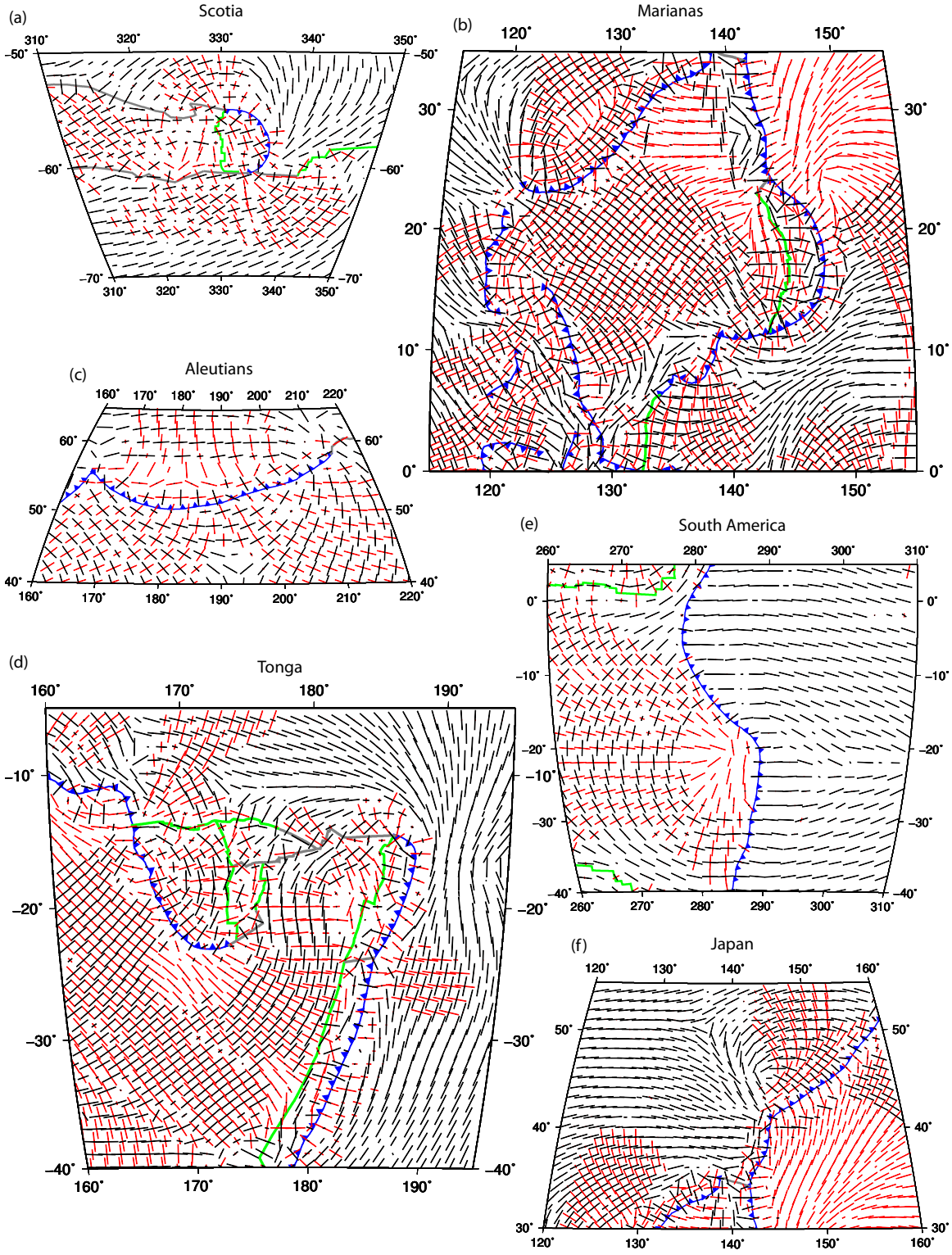

Figure 3.13. Regional state of stress at the surface for Case 2. Compression axes in black, tension axes in red. (a) Scotia; (b) Marianas; (c) Aleutians; (d) Tonga; (e) South America; (f) Japan.

The surface stress axis orientations do not vary significantly as a function of the stress exponent, yield stress, or lower mantle tomography strength. This indicates that in light of the tested parameters, regional characteristics such as interplate coupling and the geometry of subduction zones and plates are major contributing factors to the state of stress at the surface, rather than the rheology law. This was also determined by *Stadler et al*. (2010), who found that an increase in interplate coupling between the Nazca and South America plates in the Peru area strongly rotated the compression axes at the surface from trench-parallel to trench-perpendicular.

3.4.4.3 Stress Regime in Slabs

Previous studies have addressed the state of stress in slabs from earthquake focal mechanisms (*Isacks and Molnar*, 1971; *Alpert et al.*, 2010). It was shown earlier that changes in the radial viscosity profile can have a significant effect on the state of stress in slabs (*Vassiliou and Hager*, 1988; *Gurnis and Hager*, 1988; *Alpert et al.*, 2010). *Billen et al*. (2003) also found that the stress orientation in slabs is sensitive to the relative viscosity of the slab, lower mantle, and wedge. We determine the model stress regime in slabs by comparing the orientation of the compressional and tensional axes of the stress tensor to the principal axes from earthquake focal mechanisms. We also investigate the effect of changes in yield stress and stress exponent on the stress regime.

The compression axes from the CMT solutions are typically not precisely matched by the model compression axes. However, the general trends in stress regimes approximately fit the earthquake data, as shown for Case 2 in Figure 3.14 ($n = 3.0$, $\sigma_y = 100$ MPa). In Peru (Figure 3.14a), the observations show that the slab is in tension in the upper 300 km, and in compression in the deep slab. This pattern is also seen in the model results. A similar

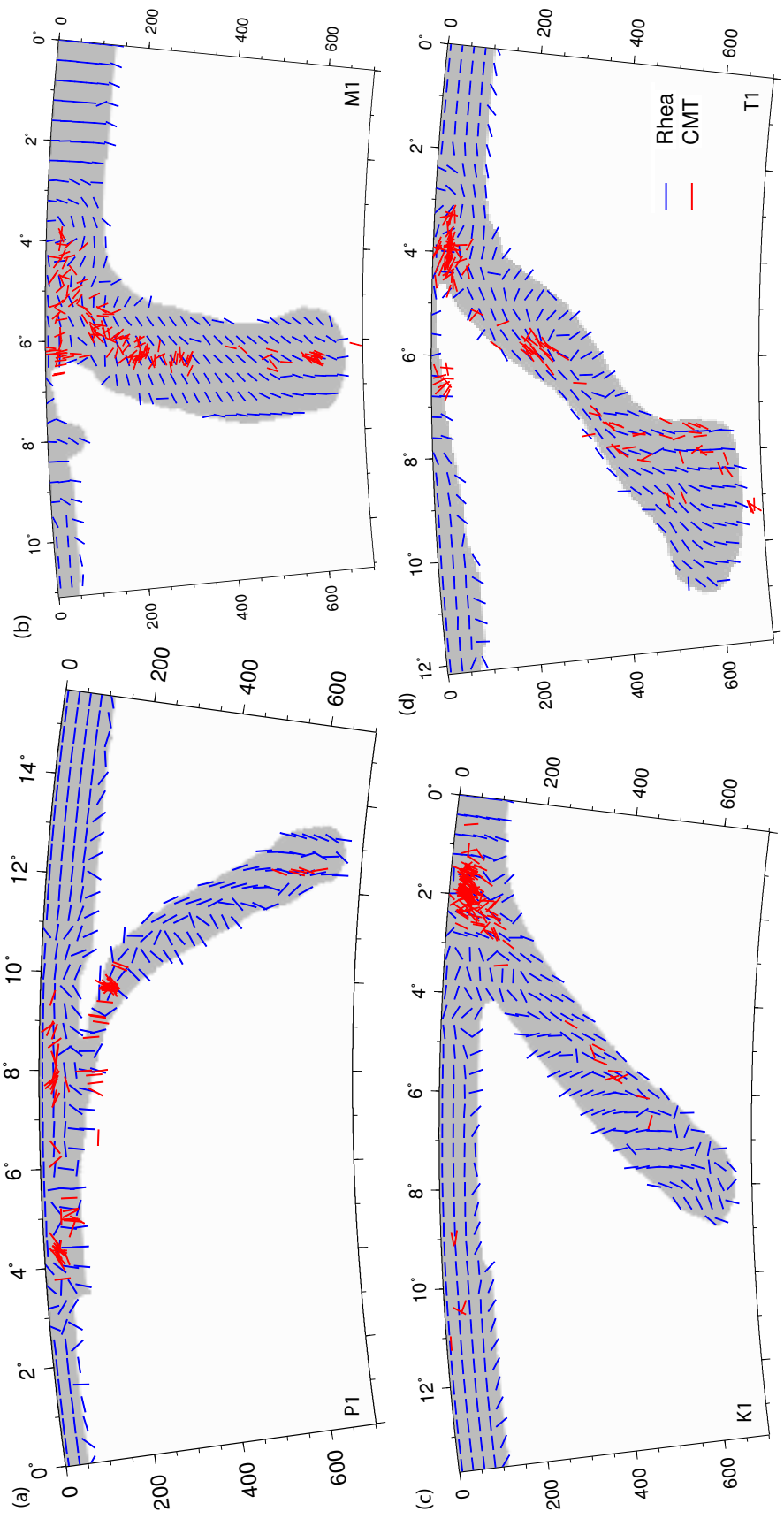

Figure 3.14. Cross-sections of state of stress in slabs; Case 2. Blue dashes: Rhea compression axes. Red dashes: CMT compression axes. The grey areas denotes nondimensional temperatures below 0.8. (a) Peru, P1 (see Figure 3.1 for location of cross-sections); (b) Marianas, M1; (c) Kurile, Ku1; (d) Tonga, T1.

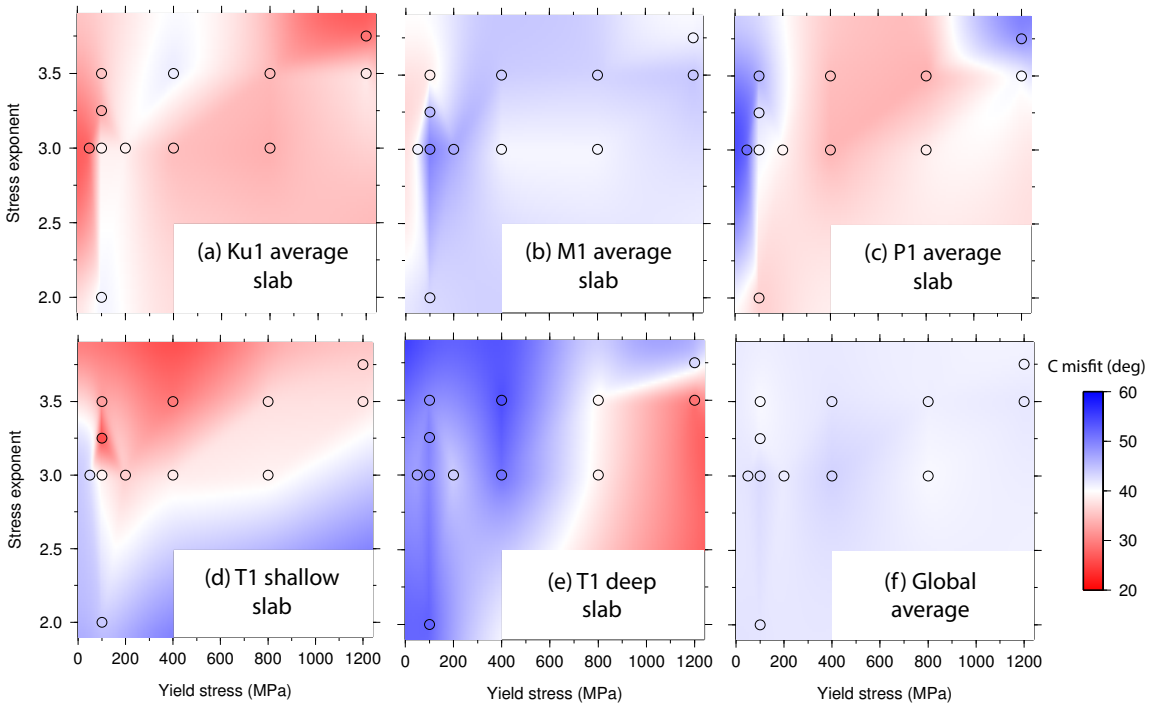

Figure 3.15. Variation of slab compression misfit with yield stress and stress exponent. (a) Kurile (Ku1) average; (b) Marianas (M1) average; (c) Peru (P1) average; (d) Tonga (T1) shallow; (e) Tonga (T1) deep; (f) Global average.

stress regime is observed in both data and model for the Marianas (M1) cross-section (Figure 3.14b). The Kurile (Ku1) and Tonga (T1) cross-sections (Figure 3.14c and d) show compression throughout the slabs, which is also reproduced in the model.

The misfits of model compressional axes with respect to CMTs are binned spatially and then averaged in the shallow slab (0–100 km depth), intermediate slab (100–410 km depth), and deep slab (below 410 km), as well as in the whole slab. These average compression misfits vary with rheology, although a significant stress regime change from compression to tension or vice versa is not observed (Figure 3.15). We do not see any universal trend of response to rheology among subduction zones. Additionally, different depth intervals within slabs (e.g., Tonga, T1, Figure 3.15d–e) even show varied responses. This suggests that the local geometry determines the sensitivity of slabs to changes in stress exponent and yield stress. The misfit

averaged for all cross-sections globally (Figure 3.15f) shows little sensitivity to the rheology. Therefore, we find that the state of stress in slabs does not constitute a useful test to determine their rheology in terms of yield stress and stress exponent.

3.4.5 Regional Dynamics

3.4.5.1 Microplate Kinematics and Trench Rollback

The motions of microplates and trenches are essential for our understanding of the convective system, as trench rollback occurs in areas of plate bending that are critical for overall plate motions. This rollback is highly sensitive to rheology, and is therefore useful for testing our models. Microplates are defined as plates with small surface areas, such as the New Hebrides, Tonga, Kermadec, Marianas, and Sandwich plates studied here. Although the Easter Island microplate is resolved and included in our models, we have not used its motions as model constraints here. The New Hebrides, Tonga, and Kermadec microplates (left column in Figure 3.11) and the Sandwich plate (center column, Figure 3.11) are rapidly rolling back (white arrows) (*Bird*, 2003), while the Marianas plate is observed to be stationary (right column, Figure 3.11). The model with stress exponent 3.0 and yield stress 100 MPa (Case 2) correctly predicts New Hebrides and Kermadec rollback both in magnitude and direction (Figure 3.11a). The rollback in Tonga is underpredicted, and Sandwich even exhibits trench advance in the dynamic model (Figure 3.11b); the modeled Marianas plate is close to stationary (Figure 3.11c). An increase in yield stress from 100 to 800 MPa (Case 5) reduces the velocity of the plates, especially the Pacific and Australian plates, and the New Hebrides microplate (Figure 3.11d–f). The Tonga, Kermadec, Marianas, and Sandwich microplates are not affected as much. Generally, the major plates appear to be more strongly affected by the increase in yield stress than microplates, especially the ones connected to subducting slabs (e.g. the Pacific, Australia, and

Cocos plates in Figure 3.3a–b). The ease with which these major plates subduct is governed by the amount of weakening in the slab hinges, and therefore by the yield stress. In the model with the highest yield stress and stress exponent (respectively 1200 MPa and 3.75, Case 12, Figure 3.11g–i), all plates are moving significantly faster than in the other models. In this case, microplates appear to be more strongly influenced by the increased nonlinearity than the major plates, since the enhanced localization of deformation affects small-scale features. Rollback is strongly overpredicted in the New-Hebrides, Tonga, Kermadec, and the Marianas. The Sandwich microplate exhibits the correct amount of rollback, but the surrounding plates are moving too fast, as do the major plates in the other study areas.

All trenches addressed here roll back in various frames of reference including hotspot reference frames, except for the Marianas, which shows rapid trench advance in hotspot reference frames (*Funiciello et al.*, 2008). Because changes in rheology affect net rotation (see Section 3.2.4), we prefer to study the effect of rheology on trench motion in a no-net-rotation frame of reference. The amount of trench rollback v_r (defined as the magnitude of the microplate velocity perpendicular to the trench, positive for rollback) depends foremost on the stress exponent, and to a lesser extent on the yield stress for small yield stresses only (Figure 3.16a, d, g, and j), exhibiting the same pattern in (σ_y, n) space as illustrated in Figure 3.4. In order to match the observed rollback, generally a stress exponent of around 3.25 is required when yield stresses larger than 200 MPa are used. The Sandwich microplate requires a higher stress exponent of 3.5–3.75 to fit the rollback constraint (Figure 3.16j).

For each of the microplates, we plot the trench rollback velocity v_r in relation to subducting plate velocity v_s (also defined perpendicular to the trench) and the second invariant of the strain rate in shallow slabs ($\dot{\varepsilon}_{\mathrm{II}}$), as the stress exponent and yield stress are varied (Figure 3.16b–c, e–f, h–i, and k–l). The magnitudes of the quantities v_r, v_s, and $\dot{\varepsilon}_{\mathrm{II}}$ increase when

the stress exponent is increased. We can observe several important characteristics when the stress exponent is kept constant while yield stress increases. First, the rollback, subduction velocity and strain rate decrease with increasing yield stress. Second, the change in v_r and v_s decreases with increasing yield stress: the decrease in v_r and v_s is significant when the yield stress is changed from 50 to 100 MPa and from 100 to 200 MPa, but for higher yield stresses the change in rollback and subducting plate velocity is small. This effect is stronger for higher stress exponents, and conforms to the two domains described by Figure 3.4. Third, models with the same stress exponent fall more or less on the same line in (v_s, v_r) space. For the four microplates, these lines have an increasing slope and shift towards larger absolute values of rollback when the stress exponent is increased. This indicates that an increase in n has more effect on the rollback than on the velocity of the subducting major plate. The ability of microplates to roll back depends on strain localization, and therefore microplates have a stronger response to higher stress exponents than large plates.

Analysis of the set of constraints formed by the observed values of v_r, v_s, and the minimum constraint on $\dot{\varepsilon}_{\mathrm{II}}$ in shallow slabs, e.g., 10^{-15} s^{-1}, shows that the three constraints are close to intersecting in (v_s, v_r) space for the Marianas and New Hebrides, and a cluster of models approximately fits all constraints. For Tonga and Sandwich, several models are close to fitting both the v_r and v_s constraints, but the strain rate for those cases is systematically too low and therefore no model fits all three constraints simultaneously. Generally, the models that perform best with respect to microplate kinematics have stress exponents and yield stress combinations of [3.0,3.25] and [50,100] MPa, or [3.5,3.75] and [400,1200] MPa, respectively.

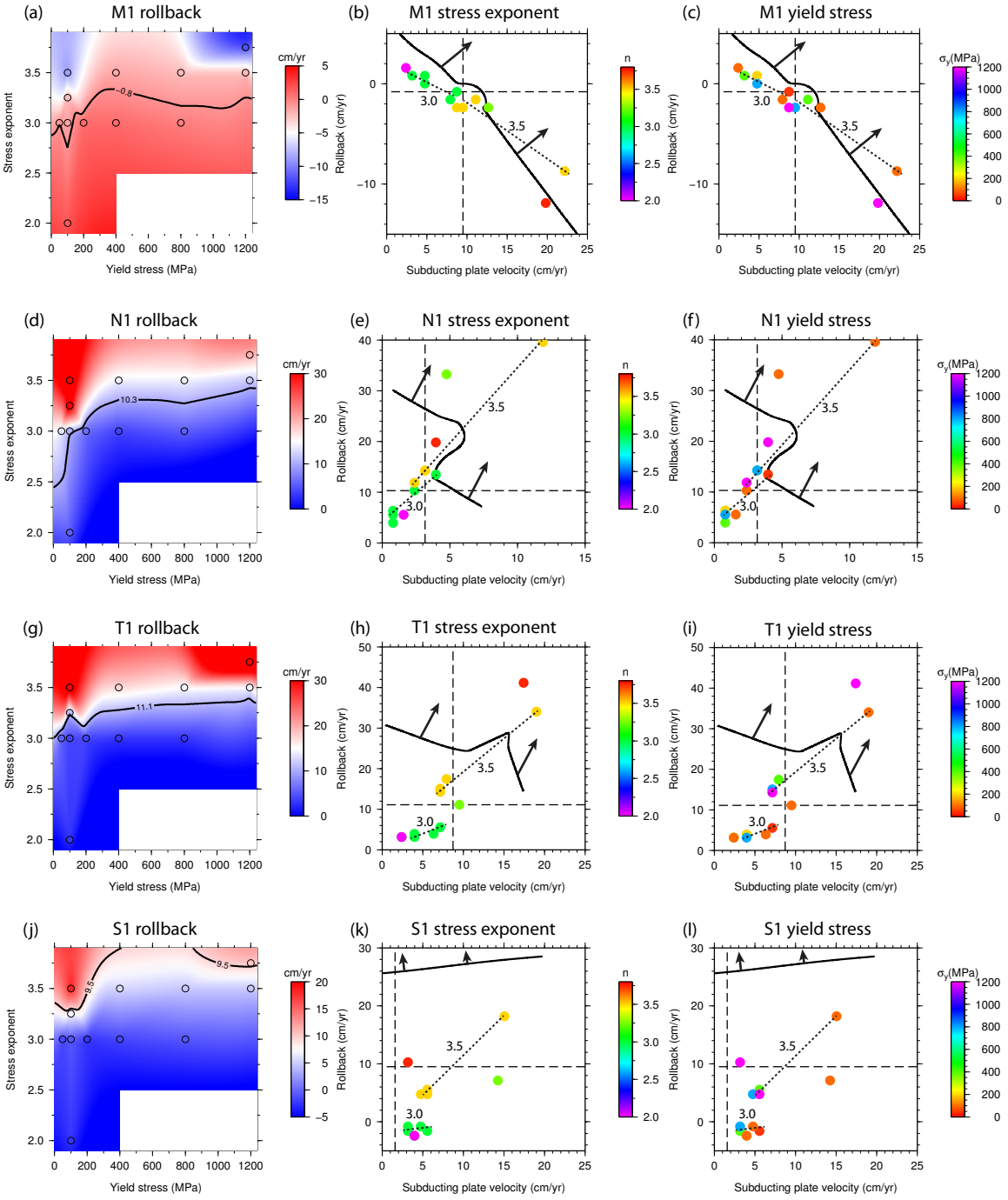

Figure 3.16. Top to bottom: Marianas, M1; New Hebrides, N1; Tonga, T1; Sandwich, S1. Left: Variation of amount of rollback v_r with yield stress and stress exponent in several slabs. The contour denotes the observed rollback. Center: Rollback velocity versus subducting plate velocity, color coded by stress exponent. The black dashed lines denote the observed rollback (horizontal) and subduction velocity (vertical), the solid contour line shows the minimum shallow slab strain rate constraint of 10^{-15} s^{-1}. Above the line as indicated by the arrows, modeled strain rates are higher than the minimum constraint. The dotted lines show trends when the stress exponent is held constant between models ($n = 3.0$ and 3.5). Right: Rollback velocity versus subducting plate velocity, but with data points color coded by yield stress. Note: Subducting and rollback velocities are both perpendicular to the trench.

We have shown that trenches and microplates above the subducting hinge display a variety of behaviors, from rapidly rolling back to being stationary. This is intimately linked to the amount of yielding in the slab hinge, slab morphology, the presence of high viscosity structures in the lower mantle beneath the slab tip, and the magnitude and orientation of velocity in the slab with respect to the plate. In the Marianas, the velocity in the slab is of the same magnitude as that of the subducting plate, and is approximately aligned with the slab (Figure 3.17a). This suggests that the modeled slab is in a stable configuration, and both the trench and the Marianas microplate are stationary. The hinge of the Marianas slab contains only a limited amount of yielding, and the yielding does not extend oceanward of the surface intersection of the plate boundary. Additionally, there is a high-viscosity structure in the lower mantle centered below the slab tip (Figure 3.10d, g), which might anchor the slab in its current vertical position. The Tonga area displays a different behavior: the slab sinks vertically into the mantle with a velocity larger than the subduction velocity of the Pacific plate (Figure 3.17c). This sinking is not aligned with the slab, which is less steep than, for example, the Marianas slab. This results in rapid rollback of the trench and the Tonga microplate with ample yielding in the slab hinge. The Tonga slab reaches into the transition zone and borders a large, high-viscosity structure in the lower mantle (Figure 3.10). The complex slab shape implies that this structure could (partially) anchor the slab and cause internal deformation of the slab rather than pure lateral motion of the entire slab. The New Hebrides slab exhibits even stronger motion not aligned with the slab (Figure 3.17b), as it is moving backward with a velocity significantly larger than the subducting plate velocity. There is substantial yielding in the hinge and within the microplate which is rolling back rapidly. The New Hebrides slab does not extend to the lower mantle and is not anchored. The entire slab can therefore move freely in a lateral sense, rather than deform to a more complex morphology.

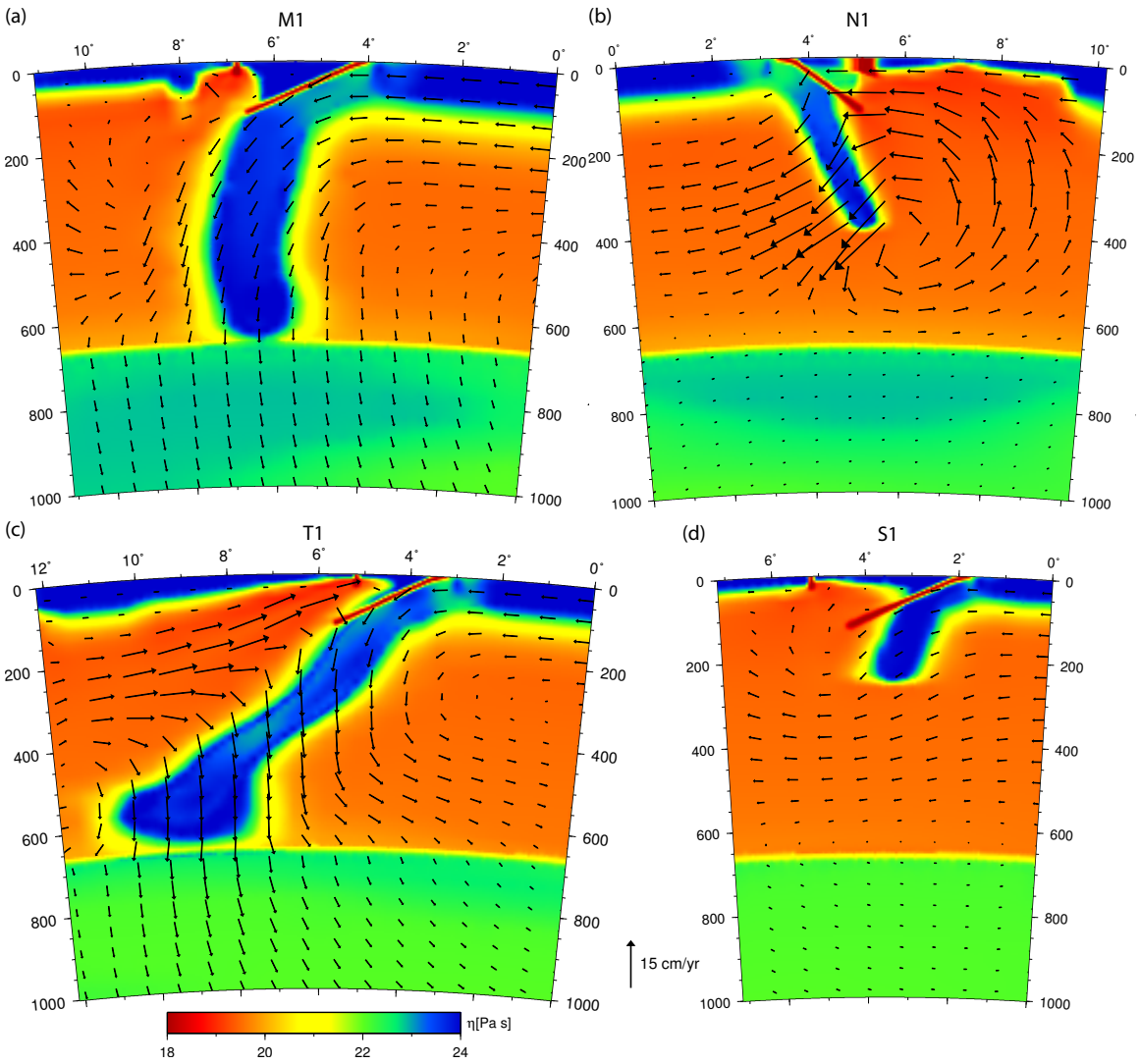

Figure 3.17. Cross-sections through slabs and microplates of Case 2, with stress exponent $n = 3.0$ and yield stress $\sigma_y = 100$ MPa. Arrows: no-net-rotation velocity; background color: viscosity. (a) Marianas, M1; (b) New Hebrides, N1; (c) Tonga, T1; (d) Sandwich, S1. See Figure 3.1 for the location of the cross-sections.

The velocities at the surface and within the mantle in the Sandwich area are overall small compared to those in the other cross-sections (Figure 3.17d), leading to small strain rates at the surface and in the slab. Yielding in the slab hinge is minimal, and the Sandwich microplate is more or less stationary in this model with $n = 3.0$. The slab is subducting more slowly than the other slabs we considered, since it is shorter and therefore has less negative buoyancy. The velocity in the slab is aligned and of the same magnitude as that of the subducting South

America plate. As illustrated in Figure 3.11, the Sandwich microplate only displays rollback when a large stress exponent of 3.75 is used. This allows stronger localization of deformation, and therefore more weakening in the hinge zone and stronger decoupling of motion between South America and the Sandwich plate.

We found that the magnitude of the velocity in plates and slabs as well as the rollback varies a great deal with the rheology. In contrast, the velocity orientation in slabs, much like the state of stress, does not vary significantly with yield stress or stress exponent; therefore the direction of slab motion and the stability of subduction zones appear to be more affected by regional factors (such as geometry of slab and plates, and presence of lower mantle structure) than by rheology.

3.4.5.2 Lateral Flow Field Around Slabs

We now turn to the lateral flow around slabs at various depths in the Tonga, Japan, and Marianas regions. The lateral velocity at 400 km depth differs considerably in orientation from the surface velocity pattern (Figure 3.18a–c and d–f), often showing return flow from plate motions. In general, lateral flow near slabs at 400 km depth is perpendicular to the strike of the trench (see Figure 3.18d–f), indicating that the orientation of mantle flow is mostly governed by the downward motion of the subducting slabs. There is toroidal flow around the edges of the slabs, but its lateral extent is limited. In the Tonga-Fiji area (Figure 3.18, left column) the interaction of flow around multiple slabs in close vicinity results in a complex flow pattern in the upper mantle. The toroidal flow around the Tonga slab causes some trench-lateral flow in the mantle wedge east of and above the New-Hebrides slab, and fast rollback of both slabs creates a strong paddle effect. There is also some lateral component to the flow in the mantle wedge above the Marianas slab, to the west of the trench (Figure 3.18, center

column). Unlike Tonga, the Marianas slab is not interacting with the lateral flow around it because its tip is anchored in the lower mantle, and therefore there is no paddle effect and less trench-perpendicular flow. However, in general, we do not observe the pervasive presence of trench-parallel flow that, e.g., *Long and Silver* (2008, 2009) require to explain the sub-slab or mantle wedge trench-parallel fast directions inferred from seismic anisotropy.

Of note is the increase in lateral velocities at 400 km depth with respect to surface velocities, by up to a factor of three in the model shown ($n = 3.0$, $\sigma_y = 100$ MPa). This occurs most significantly in the mantle wedges on top of the subducting slabs, which is to the west of the Tonga slab and to the east of the New Hebrides slab (Figure 3.18d); to the southwest of the Marianas slab (Figure 3.18e); to the west of the Japan slab, and to the north of the Kurile slab (Figure 3.18f). The strain weakening in mantle wedges leads to low viscosities which again leads to high (lateral) velocities and strain rates, due to the strongly nonlinear nature of the rheology. This velocity increase factor correlates strongly with the stress exponent: in models with $n = 3.5$, it can be as much as 5 to 10, as was also observed by *Jadamec and Billen* (2010), and studied in detail by *Billen and Jadamec* (2012).

The lateral flow at 800 km depth is much smaller due to the increase in viscosity with depth and the purely linear viscosity in the lower mantle (Figure 3.18g–i). The flow beneath slab tips experiences little effect on its orientation from the presence of slabs or the lower mantle viscosity structure. Only in the model with stronger lower mantle structure (Case 14) does the lateral flow pattern extend deeper. In our models, the orientation of lateral flow does not depend on rheology, only the magnitude of flow in the upper mantle is affected by the stress exponent.

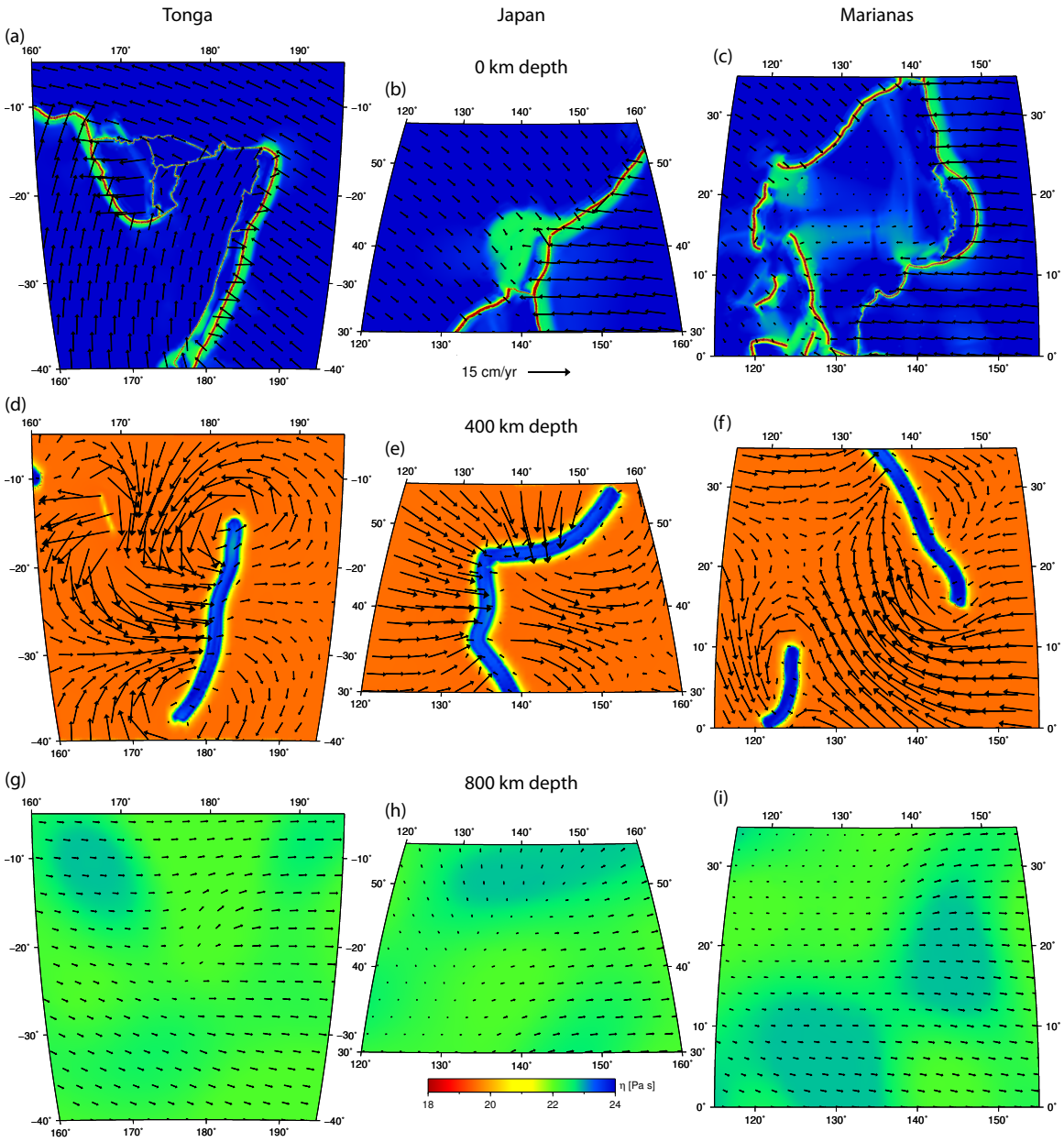

Figure 3.18. Lateral flow at depth, plotted on viscosity, for Case 2. From left to right: Tonga, Japan, Marianas. Top to bottom: Surface, 400 km, 800 km depth.

3.4.6 Model Quality

We now assess our models using the entire suite of constraints: global plate motions, plateness, net rotation, strain rate, stress in slabs, and microplate kinematics. Each model is scored as having either a good, bad, or inconclusive fit to each constraint (Table 3.5). An important observation is that no model fits all constraints without ambiguity, and different constraints have different optimal parameter ranges for the stress exponent and yield stress. For instance, globally averaged plate speeds and net surface rotation are best fit for moderate stress exponents around 3.0, whereas a good fit to plateness and strain rate constraints ideally requires higher stress exponents of 3.5–3.75. The best fitting stress exponent for trench rollback depends on the individual trench, and ranges from $n = 3.0$ to 3.75. As was demonstrated earlier, the plate motion angle misfit and the compression misfit in slabs do not allow distinction in quality among models. Often several combinations of stress exponent and yield stress fit constraints equally well, leading to non-uniqueness, illustrated by contour lines of fit to model constraints in the (σ_y, n) parameter space for plate motions, net rotation, minimum strain rate, and trench rollback. Another notable observation is the great variability in how easily constraints are met. Some constraints are fit for almost the entire parameter space tested, such as the minimum strain rate in the Tonga slab, whereas others are only met as an exception (for example the Sandwich rollback).

To determine a "best" model, one could count the constraints that are met, partially met, or not met (shown in the last column of Table 3.5). There are some models with good scores, but all have at least several constraints that are met only partially or even not at all. We consider the first-order test of global plate motion fit to be the most important, and therefore choose Case 2 ($\sigma_y = 100$ MPa and $n = 3.0$) as our best model. Models with lower yield stress do not conform to the minimum stress drop constraint ($n = 3.0$ with $\sigma_y < 100$ MPa; Case 1), and

models with higher yield stress do not fit the minimum strain rate constraints ($n = 3.0$ with $\sigma_y \geq 400$ MPa; Cases 3, 4, and 5). Models with lower stress exponents have velocities that are too slow ($n < 3.0$ for all σ_y; Case 6). Models with higher stress exponents typically have plate motions and net rotations that are too fast ($n \geq 3.25$ with $\sigma_y \leq 200$ MPa; Cases 7 and 8); increasing the yield stress along with the stress exponent partly mitigates this problem (Cases 9, 10, 11, and 12).

Model	Case	σ_y	n	ω	$\lvert v_p \rvert$	α	P_1	P_2	NR	$\dot{\varepsilon}_{\mathrm{II}}$	$\dot{\varepsilon}_{\mathrm{II}}$ T	σ_d	C	v_r M1	v_r N1	v_r T1	v_r S1	v_r all	**Total**
run97	1	50	3.0	0.1	+	○	○	○	+	○	+	−	○	+	○	○	−	○	3+, 6○, 1−
run104	2	100	3.0	0.1	+	○	○	○	+	○	+	+	○	+	+	○	−	○	4+, 6○, 0−
run98	3	200	3.0	0.1	+	○	○	○	+	−	+	+	○	○	+	○	−	○	4+, 5○, 1−
run99	4	400	3.0	0.1	○	○	−	−	+	−	+	+	○	○	−	−	−	−	3+, 3○, 4−
run107	5	800	3.0	0.1	○	○	−	−	+	−	+	+	○	○	−	−	−	−	3+, 3○, 4−
run100	6	100	2.0	0.1	−	○	−	−	+	−	○	+	○	−	−	−	−	−	2+, 3○, 5−
run102	7	100	3.25	0.1	−	○	+	+	−	+	+	+	○	○	○	+	+	+	6+, 2○, 2−
run101	8	100	3.5	0.1	−	○	+	+	−	+	+	+	○	−	−	−	○	−	5+, 2○, 3−
run105	9	400	3.5	0.1	○	○	+	+	−	○	+	+	○	○	−	−	○	○	4+, 5○, 1−
run106	10	800	3.5	0.1	○	○	+	+	−	○	+	+	○	○	○	○	○	○	4+, 5○, 1−
run108	11	1200	3.5	0.1	○	○	○	○	−	○	+	+	○	○	+	○	○	○	2+, 7○, 1−
run109	12	1200	3.75	0.1	−	○	+	+	−	+	+	+	○	−	−	−	+	○	5+, 3○, 2−
run110	13	100	3.0	0.0	+	○	○	○	+	○	+	+	○	+	+	○	−	○	4+, 6○, 0−
run94	14	100	3.0	0.25	+	○	○	○	+	○	+	+	○	+	+	○	−	○	4+, 6○, 0−

Table 3.5. Table with model scores. The models are scored as "+" when a constraint is met, as "○" when the score is ambiguous, and as "−" when the constraint is not met. Columns: σ_y: yield stress in MPa; n: stress exponent; ω: lower mantle tomography scaling between S-wave speeds and temperature; $|v_p|$: plate speeds; α: plate velocity angles; P_1 and P_2: plateness; NR: net rotation of the surface; $\dot{\varepsilon}_{\mathrm{II}}$: second invariant of the strain rate in shallow slabs; $\dot{\varepsilon}_{\mathrm{II}}$ T: second invariant of the strain rate in the Tonga slab; σ_d: stress drop; C: compression misfit in the slab; v_r: trench rollback in the Marianas (M1), NewHebrides (N1), Tonga (T1), and Sandwich (S1). The trench rollback for these four cross-sections is combined in "v_r all" for the total model score.

3.5 Discussion

In this paper, numerical models of mantle convection with plates have been computed to study the rheology and dynamics of convection on both global and regional scales. We will now discuss implications of these models relating to coupling between lower mantle structure and plate motions, the strength of slabs, and the effect of rheology on different plates, and comment on the reliability of model constraints.

We studied the effect of lateral variations in lower mantle viscosity on surface plate motions. Our results show that changes in density contrasts in the lower mantle affect the flow throughout the mantle, including surface velocities. This suggests that there is a strong coupling throughout the domain between plates, slabs, and both the upper and lower mantle. *Becker and O'Connell* (2001) concluded that the addition of lower mantle density anomalies improves fit to observed plate motions by speeding up plates, and that the contribution of lower mantle density anomalies to the average plate torque is significant ($\sim$ 30% of the total). *Conrad and Lithgow-Bertelloni* (2002) found that slabs in the lower mantle could not contribute to pull forces on plates due to the large viscosity contrast across the transition zone. Our models show a more complicated interaction of buoyancy forces and viscous drag in the mantle affecting plate motions. Generally, the increase in scaling factor ω from lower mantle seismic velocity anomalies to temperature anomalies results in structures with larger negative buoyancy, increasing overall flow as predicted by *Becker and O'Connell* (2001). Plates with no subducting slabs or only short slabs therefore speed up. However, plates that have deep slabs connecting to high-viscosity lower mantle structures slow down. To better understand this behavior, consider a Stokes sphere sinking in an incompressible viscous fluid. Its velocity U is determined by the balance between buoyancy forces acting on the volume of the sphere

as a function of the density difference between the sphere and the surrounding mantle $\Delta\rho$, and drag on the surface of the sphere as function of the mantle viscosity η: $U = 2\Delta\rho g a^2/9\eta$ (see, e.g., *Batchelor* (1967)), where a is the radius of the sphere, and g the gravitational acceleration. In the work by *Becker and O'Connell* (2001) and by *Conrad and Lithgow-Bertelloni* (2002, 2004), a radially varying viscosity was assumed, and there exists only a density contrast between slabs and the surrounding mantle. The viscosity used in our models is temperature dependent and varies laterally within the lower mantle, which not only affects the buoyancy force acting on the volume of a sinking body, but also the viscous drag on its surface. An increase in density difference due to a larger scaling factor ω results in a faster sinking velocity of slabs. But when density differences are increased, the viscosity around the slab tip also increases due to the presence of lower mantle anomalies, slowing the slabs — more so than in models with a purely radially varying viscosity. Furthermore, the large-wavelength high-viscosity structures in the mantle do not sink faster like a slab in the upper mantle would. The large irregularly shaped features experience increased viscous drag, and the increase in negative buoyancy could be partially or even fully compensated.

The plates and slabs in the models presented here are mechanically strong, with a viscosity around 10^{24} Pa s, as a result of the temperature dependence of the viscosity. Only areas with localized deformation such as plate hinges have lower viscosities of $\sim 10^{22}$ Pa s due to strain rate weakening and plastic yielding. Earlier work by, e.g., *Billen and Hirth* (2007) shows that generic kinematic time-dependent models of slab subduction require slabs with similar viscosities as those in our models, but with yield stresses of around 1000 MPa and a stress exponent n of 3.5. We have shown that models with such strong slabs perform well in producing plates with high plateness, but a stress exponent of 3.5 generally causes surface velocities and net surface rotations that are too high compared to observed values (compare

Cases 10 and 11, with $n = 3.5$ and $\sigma_y = 800$ and 1200 MPa, respectively). The yield stress of 1000 MPa would well exceed the convective stress and therefore fall in Domain II of the schematic of Figure 3.4, not permitting a narrow constraint on its value. In contrast, *Liu and Stegman* (2011) inferred that slabs have to be weak with viscosities of $\sim 10^{21}$ to 5×10^{21} Pa s in order to fit observed segmentation and curvature of the Farallon slab in time-dependent models with prescribed surface velocities, using a Newtonian rheology. If such low slab viscosities were used in our models, slabs would not be able to act as stress guides or sustain large stress drops, and plates would display small plateness with little internal rigidity. It is not clear if our present models are inconsistent with the work of *Liu and Stegman* (2011) or not, as the recent history of Farallon slab subduction beneath North America has been one in which the slab is descending into a region previously dominated by flat-slab subduction, which presumably dramatically altered the mantle compared to most regions. Furthermore, our preferred values for n and σ_y (3.0 and 100 MPa, respectively) result in slab break-off in time-dependent models (*Billen and Hirth*, 2007; *Andrews and Billen*, 2009), as these studies require a significantly higher yield stress of 500-1000 MPa in order to preserve slab strength with time.

The ongoing debate as to whether slabs are weak or strong exists partly because various studies address different aspects of slab strength. Linear models effectively take into account the integrated strength of slabs, where the viscosity in the hinge of the subducting slab equals that of the rest of the slab. Nonlinear models assess localized weakening, such that especially in the hinge a lower viscosity compared to the rest of the slab is permitted. An equivalent total amount of slab deformation in Newtonian models would require overall weaker slabs compared to our models or those by *Billen and Hirth* (2007) due to the lack of localization of deformation. As was described in Section 3.1, observations of bending-related faulting and

serpentinization in outer rises (*Ranero et al.*, 2003; *Grevemeyer et al.*, 2005), as well as gravity measurements showing reduction in flexural rigidity towards the trench (*Billen and Gurnis*, 2005), support the notion of localized weakening in hinges of subducting plates present in our models.

Analytic boundary layer models of convection with finite plate strength using an energy balance approach show that multiple solution branches for plate velocities exist, depending on choices in material properties of the mantle and lithosphere (*Crowley and O'Connell*, 2012). In that study, Earth-like plate motions are reproduced; however only a depth-dependent viscosity is considered. The range of lithosphere viscosities found in our models ($\sim 10^{22}$–10^{24} Pa s) could locally represent solutions on different branches, therefore locally affecting the dominance of lithosphere and mantle terms in the energy balance.

The dynamic models reproduce the observed variety in trench rollback, ranging from rapid rollback (Tonga, New Hebrides) to stationary trenches (Marianas). This amount of rollback is predominantly affected by the dip and length of the slab, i.e., by subduction duration (*Gurnis et al.*, 2004). The Sandwich slab is observed to roll back rapidly, whereas our models have great difficulty predicting this rollback for such a short slab reaching to only about 250 km depth. Considering the subduction initiated at about 45 Ma (*Barker*, 2001; *Gurnis et al.*, 2004) and the observed rapid trench rollback, a far larger length of slab would be expected than incorporated in our model. Recent P-wave tomography models suggest the presence of a dipping high seismic velocity anomaly beneath the Sandwich trench down to the transition zone and beyond, which could be perceived as the continuation of the Sandwich slab (*Li et al.*, 2008; *van der Meer et al.*, 2009). This additional negative buoyancy would significantly increase the ability of the Sandwich trench to roll back, and potentially alter the state of stress at the surface to better match observations of tension (Section 3.4.2 and Figure 3.13).

The effect of rheology on plate motions varies between plates depending on their nature. Generally, the major plates appear to be more strongly affected by the increase in yield stress than microplates, especially ones connected to subducting slabs (e.g., the Pacific, Australia, and Cocos plates in Figure 3.3a–b). The ease with which these major plates subduct is governed by the amount of weakening in the slab hinges, and therefore by the yield stress. In contrast, the increase in stress exponent has a stronger effect on the microplates than on the major plates, as small-scale features are more significantly influenced by localization of deformation. Stronger nonlinearity enhances decoupling of microplates from the surrounding large plates, and therefore allows faster trench rollback in the Tonga, New Hebrides, Marianas, and Sandwich areas.

In this study, we extensively rely on plate motion models, minimum strain rate estimates, and state of stress to test our dynamic models. In recent years, the plate motion models, as well as estimates of net surface rotation, have improved with the increased availability of GPS data and an improved understanding of plate motions in the past 150 My (*Torsvik et al.*, 2010; *Argus et al.*, 2011). We found that the differences between the NNR_NUVEL1A, NNR_GSRM-2, and NNR_MORVEL56 models are significantly smaller than variations between our models related to choices in rheology (*DeMets et al.*, 1994; *Kreemer et al.*, 2006; *Argus et al.*, 2011). Therefore, in light of the model analysis described here, the use of NNR_NUVEL1A has proven to be adequate, and errors associated with rotation poles in the plate motion models are insignificant for the purposes of our analysis. Minimum strain rate estimates from seismic moment release (*Bevis*, 1988; *Holt*, 1995; *Nothard et al.*, 1996) are an important component of the constraints on mantle convection models in this study. However, these estimates are based on accumulated seismicity within the past century. We cannot tell if there exists a temporal variation in seismicity with a period longer than our measurement period, and therefore we do not

know with certainty how representative these minimum strain rate estimates are for slabs that have been subducting for tens of millions of years (*Gurnis et al.*, 2000a). We have not made an attempt to compare misfits in the predicted state of stress between different studies. The state of stress and its misfit with stress determined from CMT focal mechanisms vary significantly from slab to slab and also within slabs, and thus we conclude that globally averaged misfits do not convey much information. Additionally, no comparison with previous work addressing the state of stress in slabs has been made, since these studies all have the viscosity structures prescribed (*Vassiliou and Hager*, 1988; *Billen et al.*, 2003; *Alpert et al.*, 2010), resulting in an absence of feedback between the state of stress and viscosity. It is unclear whether this may have implications for the resulting stress field in those models.

It is to be expected that the coupling and rheology of plates vary depending on, for example, local tectonic setting, pre-existing faulting in the subducting plate (*Ranero et al.*, 2003), and the amount of water being released from the slab during subduction (*Hebert et al.*, 2009). The effect of spatial variation in plate boundary strength has not yet been extensively explored, but could be used to gain a better understanding of interplate coupling and its effect on plate motions and state of stress in plates. Furthermore, the models presented in this study are instantaneous solutions to the Stokes equation. The computational cost of these global models (circa 144,000 computing hours per model) prevented the incorporation of time dependence. Time-dependent models would allow us to study the evolution of plates and slabs through time, providing an additional constraint on rheology, as plates and slabs must be able to sustain their strength through significant intervals in geologic time. Additionally, time dependence allows tracking of strain accumulation, such that the effect of grain size reduction and recrystallization processes on viscosity could be addressed.

3.6 Conclusions

We computed fully dynamic instantaneous global models of mantle convection with plates, incorporating a composite rheology with yielding. A local high resolution of $\sim$ 1 km allows us to study regional features such as trench rollback and microplate motions. The rheological parameters σ_y (yield stress) and n (stress exponent) govern the strength of materials, the non-linearity of their behavior, and flow velocity magnitudes in the system. Global plate motions, trench rollback, net rotation, plateness, and minimum strain rates from seismic moment release provide important constraints on these rheological parameters. Although we are able to match general trends in the state of stress in plates and slabs, it does not allow for distinction in quality among models. We find that a model with $n = 3.0$ and $\sigma_y = 100$ MPa best fits the suite of model constraints. Plates and slabs are strong with a viscosity of 10^{24} Pa s, with only localized weakening in slab hinges to $\sim 10^{22}$ Pa s accommodating deformation. This results in significant coupling throughout the model domain, from lower mantle structures to surface motions. The lateral flow around slabs is generally trench-parallel, induced by the strongly coupled downward motion of the subducting slabs, and therefore our models do not account for the significant trench-parallel flow inferred from shear-wave splitting analysis.

Acknowledgements

This work was partially supported by the NSF PetaApps program (OCI-0749334, OCI-0748898), NSF Earth Sciences (EAR-0426271, EAR-0810303), and the Caltech Tectonics Observatory (by the Gordon and Betty Moore Foundation). Computing resources on TACC Ranger, Lonestar, and Spur systems were provided through the NSF TeraGrid under grant number TG-MCA04N026. The figures were produced using Generic Mapping Tools (GMT) and Paraview.

Chapter 4

Dynamics of the 50 Ma Plate Reorganization

4.1 Abstract

The cause of relatively rapid plate reorganizations in the past, including the change in the direction of the Pacific plate at $\sim$ 50 Ma, is not well known. Whether such changes are driven by mantle or plate processes is the subject of ongoing discussion. We use high-resolution instantaneous dynamic mantle convection models capable of resolving plate boundaries at a fine scale, $\sim$ 1 km, to study the reorganization occurring around 50 Ma. This event is commonly associated with a swerve in direction of Pacific plate motion and major tectonic events in the Pacific region, including initiation of Izu-Bonin-Marianas and Tonga-Kermadec subduction. Slab break-off at the East Asian subduction zone, related to arrival of the Izanagi-Pacific spreading ridge at the trench, as well as plate motion changes in the Atlantic and Indian oceans expressed by fracture zone bends, may also be related to the reorganization. The plate boundaries in our models are derived from global plate reconstructions, and the thermal structure is obtained from time-dependent convection models with a resolution of $\sim$ 40 km. A composite viscosity including non-Newtonian viscosity and yielding allows for localization of deformation in the plates, bending slabs, and upper mantle. The resulting models are validated

against the inferred plate motions at 55 and 45 Ma. We further compare model outcomes at these times in terms of (changes in) surface velocities, intraplate deformation, state of stress, and mantle flow. We concentrate on the Pacific plate as it was subject to a major change in motion during the reorganization, while focusing on the initiation and cessation of subduction in the western Pacific.

4.2 Introduction

Reconstructions of past plate motions are typically created using a wide variety of constraints, including paleomagnetic data (e.g. apparent polar wander paths), geologic restorations of conjugate continental margins, volcanic records for onset of new subduction zones, and marine surveys of magnetic anomalies and seafloor bathymetry, especially fracture zone orientations.

Although relatively detailed plate tectonic evolution can be reconstructed back to $\sim$ 250 Ma (*Torsvik et al.*, 2010; *Seton et al.*, 2012), the force balance associated with this evolution is poorly understood. A crucial example is the enigma of rapid plate reorganizations. During these events, plate motions significantly changed orientation, while plate boundaries were formed or destroyed all within a few millions of years. Several such plate reorganizations have been inferred, including ones at around 100 Ma, 50 Ma, and 6 Ma (*Wessel et al.*, 2006; *Austermann et al.*, 2011). The cause of these reorganizations is subject to significant discussion, and the main topic of this chapter.

We focus on the reorganization at $\sim$ 50 Ma, as there is a relative abundance of available observations and limited error in reconstructions compared to older events. The best-known manifestation of this event is the bend in the Hawaiian-Emperor chain (HEB), dated between 47 and 50 Ma (*Sharp and Clague*, 2006; *Tarduno et al.*, 2009), and thought to represent

a significant change in the absolute motion of the Pacific plate in both fixed and moving hotspot reference frames. The initiation of the Izu-Bonin-Marianas (IBM) and Tonga-Kermadec subduction zones around 50 Ma is a second component of the plate tectonic puzzle (*Stern and Bloomer*, 1992; *Gurnis et al.*, 2004). Other concurrent phenomena include the South Pacific triple junction reorganization and the collision of the Indian and Eurasian continents (*Wessel et al.*, 2006; *Cande and Stegman*, 2011).

The initiation of subduction may have been an essential part in the chain of events during the 50 Ma reorganization, likely caused by, as well as reinforcing, the change in motion of the Pacific plate (e.g., *Gurnis et al*. (2004)). *Whittaker et al*. (2007) propose that the completion of subduction of the Izanagi-Pacific Ridge (IPR) resulted in massive slab break-off along the Japanese trench, changing the forces on the Pacific plate from ridge-push to slab-pull and initiating a rotation of plate velocity from northwest to west around 53 Ma. This change in Pacific plate motion caused cessation of Tasman Sea spreading at $\sim$ 52 Ma. Increased slab pull north of Australia due to westerly progression of the subducting Wharton Basin ridge (to the northwest of Australia) changed the absolute plate motions of Australia from northwest to north, and caused faster spreading between Australia and Antarctica. The combination of Australia and Pacific plate motion changes between 53 and 50 Ma could then nucleate the initiation of the IBM and Tonga-Kermadec subduction zones, further increasing the westward rotation of the Pacific plate. *Whittaker et al*. (2007) additionally suggest that the observed subsequent slowdown of sub-Pacific mantle flow at 47 Ma (*Tarduno et al.*, 2003) may have been caused by the progressive impediment of lateral sub-Pacific flow by the descending slabs. This constitutes a "top-down" view, where plate motions steer the reorganization and govern mantle flow (e.g., *Anderson* (2001)).

However, several studies have at least partly attributed the HEB to southward movement

of the underlying Hawaiian hotspot prior to $\sim$ 50 Ma (*Steinberger et al.*, 2004; *Tarduno et al.*, 2003). Temporary pinning of the plume by a nearby ridge could cause significant hotspot motion (*Tarduno et al.*, 2009). Mantle plumes may have an important effect on the driving of plate motions, specifically the arrival of a plume head below the lithosphere together with the associated lateral asthenospheric flow (*Cande and Stegman*, 2011; *van Hinsbergen et al.*, 2011). These observations and inferences are consistent with the "bottom-up" view where mantle flow drives plate motion (e.g. *King et al.* (2002)).

Whether the top-down or bottom-up view best represents the force balance of the Earth's convective system has implications for the coupling between mantle flow and plate motions (*Crowley and O'Connell*, 2012). Numerical convection models at the time of plate reorganizations that include both mantle and plates provide a way to obtain greater insight into this force balance. *Richards and Lithgow-Bertelloni* (1996) tested the hypothesis that the collision between India and Eurasia gave rise to the HEB by combining the Indian and Eurasian plates into one. In these models, no appreciable effect on the motion of the Pacific plate was found, and no convergence arises between the Pacific and Australian boundaries. Instead, the authors speculate that the HEB is caused by the sudden change from transverse motion to subduction along preexisting transform faults in the western Pacific. In a more extensive study, *Lithgow-Bertelloni and Richards* (1998) investigated the kinematics of the last 120 My of plate motions and dynamics of Cenozoic motions by means of a self-consistent model of plate motions. This model was constructed from a simplified subduction history, for which the induced plate motions for each stage of the Cenozoic was approximately reproduced, except for the stage after the HEB. The study shows that the main plate-driving forces arise from subducted slabs ($>$ 90%, predominantly in the lower mantle), with forces due to lithospheric effects such as oceanic plate thickening providing a minor component ($<$ 10%). However, sudden plate mo-

tion changes defined by stage boundaries, such as the westward rotation of the Pacific implied by the HEB, remain unexplained. *Conrad and Lithgow-Bertelloni* (2004) further constrain the relative importance of slab suction and slab pull by comparing Cenozoic plate motions to model predictions that include viscous mantle flow and a proxy for slab strength. Slab pull from upper mantle slabs combined with slab suction from lower mantle slabs reproduce the observation that subducting plates currently move ~ 4 times faster than nonsubducting plates, and the temporal evolution of plate motions is explained through increase of slab length with time. Although the speedup of the Pacific during the latter half of the Cenozoic is predicted, the rapid northerly to westerly change in Pacific plate motion direction indicated by the HEB is not. Instead, the shift in plate motion direction gradually evolves during the entire Cenozoic.

A different approach is used by *Faccenna et al.* (2012), where the role of slab pull acting on the Pacific plate is analyzed during its early Tertiary change in motion. In this study, slab pull forces are estimated by integrating the negative buoyancy of a 700 km long slab along subduction boundaries. The torques predicted from this simple slab pull model match the directions of Pacific plate Euler vectors during the Tertiary fairly well, and the authors suggest that the change of the Pacific motion at $\sim$ 50–40 Ma is driven by the onset of the Izu-Bonin-Mariana system and, soon afterwards, by the Tonga-Kermadec subduction zones.

The limitation in these previous studies is that the flow models, although capable of predicting general plate motions, could not resolve key features such as plate boundaries and localized deformation in subducting plates. In this paper, we use the finite element code `Rhea` to compute global dynamic convection models with plates. This code utilizes adaptive mesh refinement (AMR) (e.g., *Burstedde et al.* (2008a)). AMR ensures a high resolution in areas of the model domain that have high gradients in viscosity and temperature, while allowing a lower resolution elsewhere. This technique reduces the total number of elements in a

numerical mesh, rendering global convection computations with well-resolved plate boundaries computationally feasible (*Stadler et al.*, 2010; *Alisic et al.*, 2010, 2012); see Chapter 3. We study the 50 Ma plate reorganization through the use of use high-resolution dynamic mantle convection models capable of resolving plate boundaries at a fine scale, mitigating the severe limitations of previous flow models. A composite viscosity, including a non-Newtonian component as well as yielding, allows for localization of deformation in the plates and upper mantle. These instantaneous models are validated by reproducing inferred plate motions at 55 and 45 Ma. We then compare model outcomes at 55 and 45 Ma in terms of (changes in) intraplate deformation, state of stress, and mantle flow.

4.3 Methods

We compute instantaneous dynamic global models of mantle convection with plates at 55 and 45 Ma before and after the plate reorganization. These models are computed using the equations, preconditioning, solver, and meshing techniques described in detail in Section 3.3. The utilization of adaptive mesh refinement allows for resolution of plate boundaries and other strongly deforming areas at a fine scale. A major difference with the present-day models presented earlier is the manner in which the model input is assembled, as we now depend on reconstructions of plates and mantle structure in the geologic past for the locations of plate boundaries, lithospheric thickness, slab morphology, and transition zone and lower mantle structure.

The software `GPlates` was used to obtain plate boundaries at 55 and 45 Ma (*Boyden et al.*, 2011; *Gurnis et al.*, 2012b). The changes in plate motions and the nature of plate boundaries associated with the plate reorganization around 50 Ma described in the introduc-

tion are represented in the GPlates reconstructions (see Figures 4.1 and 4.2). On the northwest boundary of the Pacific plate, the subduction of the Izanagi-Pacific Ridge (IPR) occurs between 60 and 55 Ma (Figure 4.1a–b). To the west of the southwestern corner of the Pacific plate, the Tasman Sea spreading ceases between 55 and 50 Ma (Figure 4.1b, d). Between 50 and 45 Ma, the Pacific plate motion rotates from northwest to west, and the spreading between the Australia and Antarctica plates increases significantly (Figure 4.1d–e). In the same time period, subduction is initiated in the Tonga-Kermadec (TK) and the Izu-Bonin-Marianas (IBM) subduction zones on the western boundary of the Pacific plate (Figure 4.2d–e).

Without tomography models to infer mantle structure, we rely on predictions from time-dependent convection models. It is possible to infer mantle structure from tomography for past times with an inverse convection model (see e.g. *Liu and Gurnis* (2008)), but with current methods this would result in broad and smooth representations of slabs, and well-defined slabs are essential. The time-dependent models are computed with CitcomS (*Tan et al.*, 2006), and are based on the same GPlates line data, plate rotations, and age grids, but at a lower resolution making time stepping from 250 Ma computationally feasible. The CitcomS mesh has a lateral mesh size of $\sim$ 40 km. The reconstructed age grids shown in Figure 4.1e–f and 4.2e–f are used to define the thermal structure of the lithosphere. In the top 350 km of the mantle, slabs associated with reconstructed subduction zones are assimilated with a specified age and thickness, a 45° slab dip with a radius of curvature of 200 km (*Gurnis et al.*, 2012a). These slabs are then advected using reconstructed plate motions as surface velocity boundary conditions and the overall computed convective flow, such that an estimate of overall mantle structure can be obtained at any intermediate geologic time since 250 Ma. This low-resolution temperature field at 55 and 45 Ma is used in the construction of the Rhea temperature field, replacing the tomography and other geophysical constraints used in the present-day models

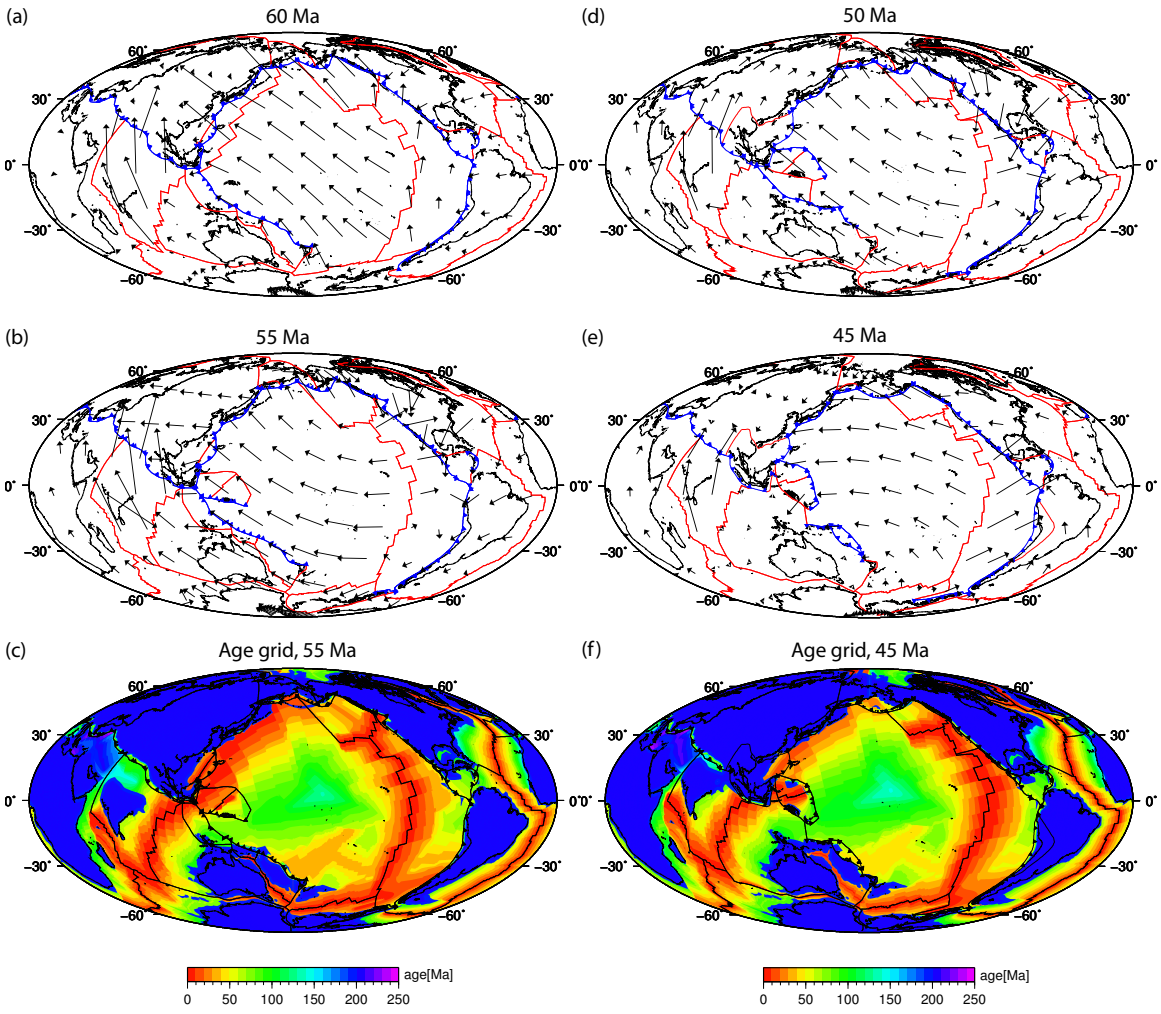

Figure 4.1. (a) `GPlates` reconstruction of global plate motions at 60 Ma; (b) 55 Ma; (c) Reconstructed age grid at 55 Ma; (d) Reconstructed plate motions at 50 Ma; (e) 45 Ma; (f) Reconstructed age grid at 45 Ma.

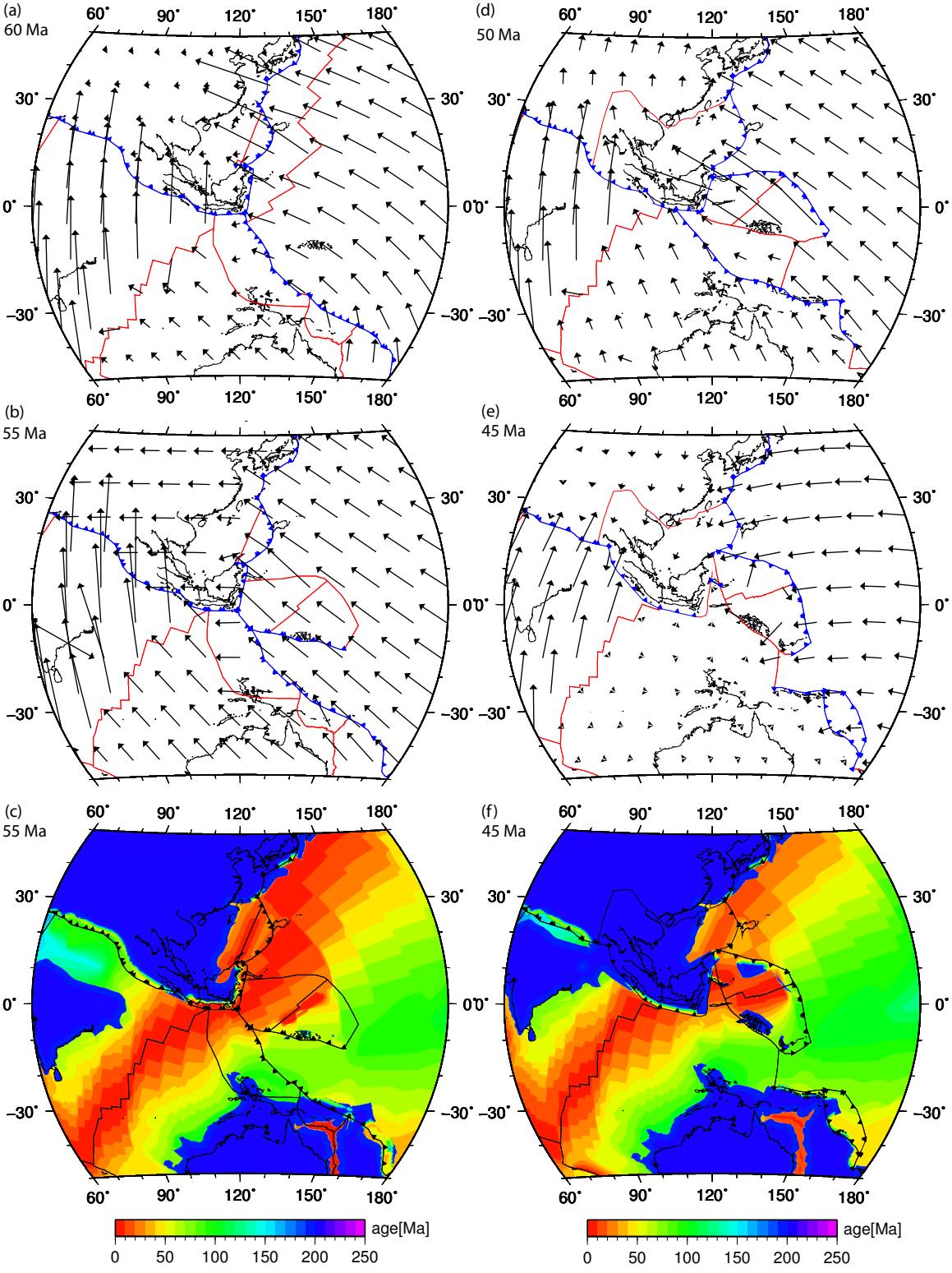

Figure 4.2. (a) `GPlates` reconstruction of plate motions in the western Pacific at 60 Ma; (b) 55 Ma; (c) Reconstructed age grid at 55 Ma; (d) Reconstructed plate motions at 50 Ma; (e) 45 Ma; (f) Reconstructed age grid at 45 Ma.

(model "BO4" in *Bower et al.* (2012)).

It is essential for the dynamic models with plate motions that slabs are sharply resolved, so that the slabs act as stress guides (see Section 3.2.2). To ensure that slabs retain their sharpness in the top 350 km of the mantle, we re-assimilate the slabs in this depth interval at `Rhea` mesh levels (which are different from the `CitcomS` levels) and incorporate this into the overall `Rhea` temperature field, together with the low-resolution `CitcomS` mantle structure and the lithospheric structure from the reconstructed age grids. The resulting mesh in the `Rhea` models has a resolution of $\sim$ 1 km around plate boundaries, and 2–10 km elsewhere in the plates and slabs. In other areas of the mantle with smaller temperature and viscosity gradients away from slabs, the resolution is 80–150 km.

We use the composite rheology law described in Section 3.3.2, combining linear diffusion creep, nonlinear dislocation creep, and yielding. The strain rate dependent components (dislocation creep and yielding) allow for localized weakening, which is crucial to allow otherwise stiff plates to bend in subduction zones. We assume the same bulk rheology in the past as today. Therefore, we use the parameter values that provide the best fit to the various constraints on present-day models explored in Section 3.4, namely a stress exponent $n = 3.0$ and yield stress $\sigma_y = 100$ MPa. The geological boundaries derived from paleo plate reconstructions are used to define weak zones that effectively decouple the plates, by means of a pre-exponent to the viscosity of 10^{-5} (see Section 3.3.2). The time-dependent model used to derive the mantle structure has a significant fraction of high-viscosity slab remnants accumulated in the lower mantle. Therefore, we use a smaller grain size in the lower mantle compared to Chapter 3 ($70 \times 10^3 \mu$m instead of $100 \times 10^3 \mu$m), to compensate for the increase in bulk lower mantle viscosity with respect to a smoother lower mantle structure from tomography.

Model outcomes are velocities at the surface and in the interior of the mantle, viscosity,

strain rate, and state of stress. The models at 55 and 45 Ma are validated by comparing model surface velocities to reconstructed plate motions. We then study changes in surface strain rate, viscosity, and state of stress between the 55 and 45 Ma models. In addition, viscosity, velocity, and the state of stress in several cross-sections around the Pacific ocean are compared. We also study lateral flow patterns in the mantle for clues of causes and effects of the plate reorganization at around 50 Ma.

4.4 Results

4.4.1 Model Viscosity

The use of time dependent models to create mantle structure results in features that are significantly sharper compared to structures derived from tomography, especially in the lower mantle (see Chapter 3). The advected slabs and their remnants have a considerable lifespan as they accumulate in the lower mantle (Figure 4.3b–c). These high-viscosity features are relatively stable; we do not see significant changes in their position or shape between 55 Ma and 45 Ma.

4.4.2 Plate Motions

A first requirement of a dynamic convection model with plates is that deformation primarily takes place at plate boundaries rather than within plate interiors. The models at 55 Ma and 45 Ma indeed display this localized deformation, illustrated by high strain rates and low viscosities at the plate boundaries, while plate interiors are generally strong with high viscosities and low strain rates (Figures 4.4a–d and 4.5a–d). One exception can be seen at the western edge of the Pacific plate, where the subduction of the Pacific-Izanagi Ridge had just completed

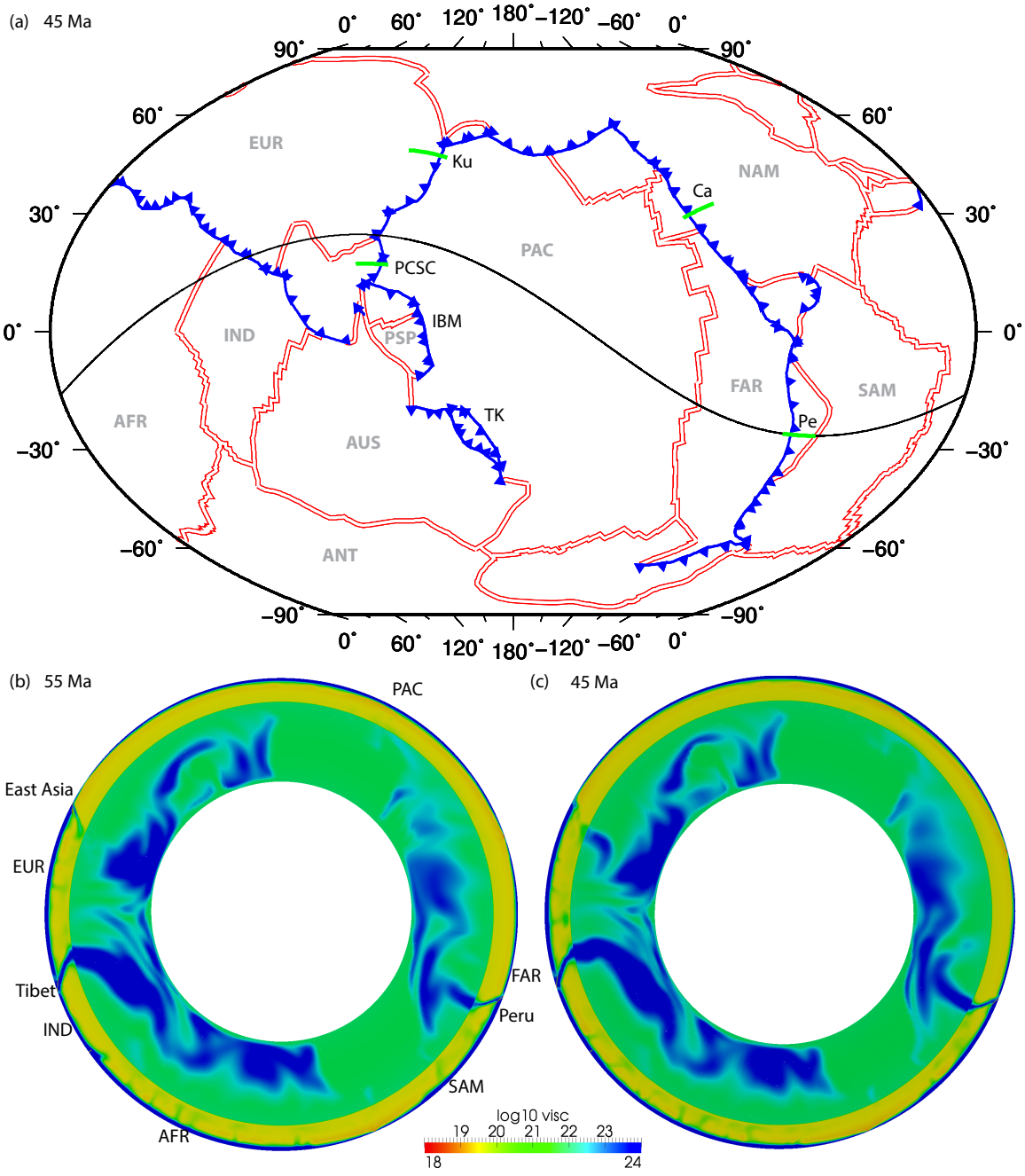

Figure 4.3. (a) Map with locations of the annulus shown in panels (b) and (c) (black), and the cross-sections of Figures 4.8 and 4.9 (green). Note that the plate boundaries are plotted at their 45 Ma configuration to show the newly formed subduction zones. (b) Global cross-section through model viscosity at 55 Ma; (c) 45 Ma. Plate abbreviations: AFR: Africa; ANT: Antarctica; AUS: Australia; EUR: Eurasia; FAR: Farallon; IND: India; NAM: North America; PAC: Pacific; PSP: Philippine Sea Plate; SAM: South America. Cross-section abbreviations: Ca: California; Ku: Kurile; PCSC: Proto-South China Sea; Pe: Peru. Subduction zone abbreviations: IBM: Izu-Bonin-Marianas; TK: Tonga-Kermadec.

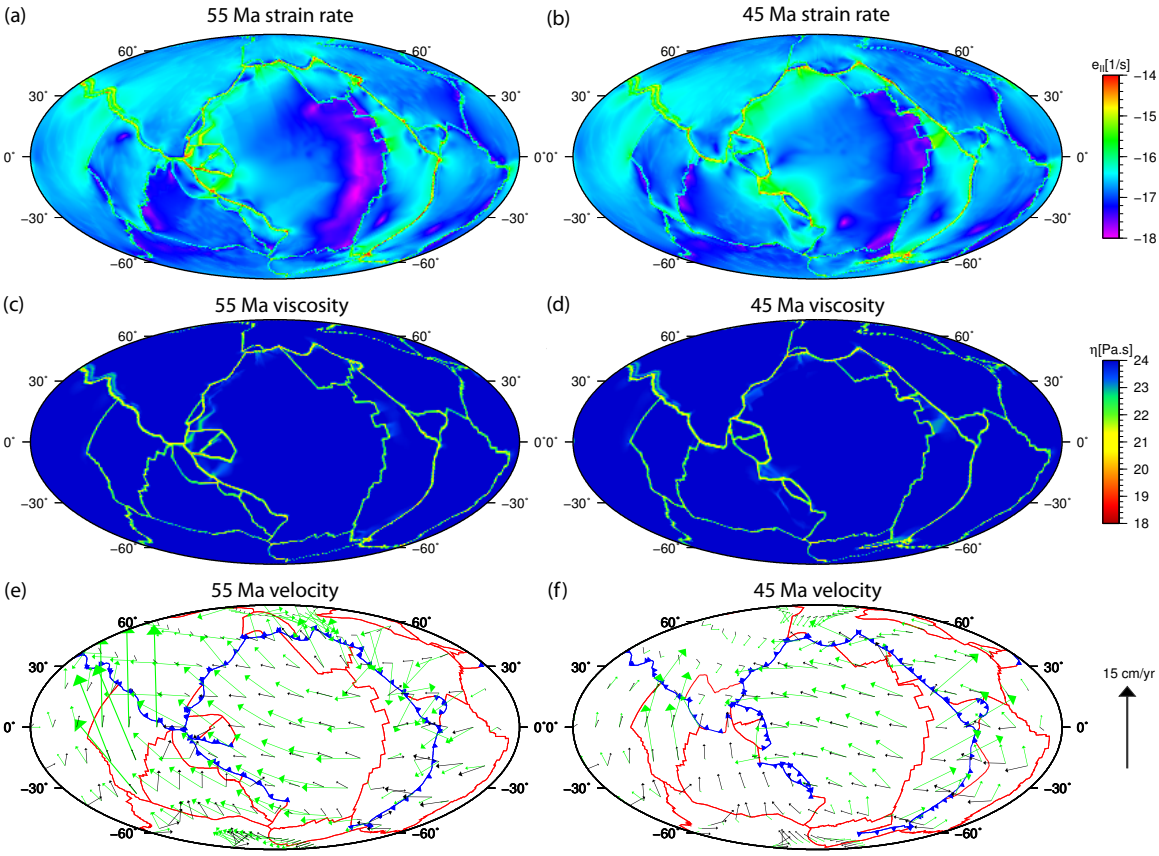

Figure 4.4. Map view of modeled surface quantities; global view centered on the Pacific at 55 Ma (left) and 45 Ma (right). (a)–(b): Second invariant of the strain rate; (c)–(d): Viscosity; (e)–(f): Velocities from the dynamic model (black) and from plate reconstructions (green). No line data is plotted in the viscosity and strain rate panels.

by 55 Ma. Young and therefore thin oceanic lithosphere still remains (see Figures 4.1e and 4.2e), which is easier to deform than the surrounding thicker lithosphere on the Pacific plate. Another narrow band of deformation is present to the south of this area, in the Pacific plate just east of Australia and north of the Tasman Sea Ridge. Interestingly, this is at the location where later an inferred boundary between the Pacific and the Indo-Australia plate has developed at 45 Ma (Figure 4.2f).

The model surface velocities are compared with velocities derived from `GPlates` paleo plate reconstructions (Figures 4.4e–f and 4.5e–f). The fit in plate motions is poor. Most plates are moving too slow, especially the ones that have subducting slabs attached to them, such

as the Pacific, Australia, India, and Kula plates. The Pacific plate is moving almost due west in the 55 Ma model, lacking a northward component. The Australia plate is moving to the northeast instead of the northwest. At 45 Ma, the Pacific plate continues moving westward in the dynamic model without much change, only its southern section shows a decrease in northward motion. The Australia plate now moves more to the north, but the other plates have not significantly changed direction.The lack in plate motion change could be linked to the highly stationary lower mantle slab remnants, which we will explore further. An exception is the fast clockwise rotation of the Philippine Sea Plate between 55 and 45 Ma (center of Figure 4.5e–f), which is also observed in the plate motion reconstructions.

An important characteristic of global plate motions is the net rotation of the surface, which describes the rotation of the entire surface with respect to the deep mantle. Estimates of this net rotation for the past 150 Ma by *Torsvik et al*. (2010) are significantly smaller than in the `GPlates` reconstruction, even when the net rotation from the plate reconstruction is averaged into the same intervals as used in the estimate by Torsvik et al. (Figure 4.6). The slow and relatively unchanging plate motion in the dynamic plate motion models is reflected in the net surface rotation, which, approximately constant at 0.11°/My in a westward orientation (dominated by the motion of the Pacific plate), is significantly smaller than both the `GPlates` prediction and the prediction by *Torsvik et al*. (2010) at 55 Ma (respectively 0.52 and 0.33°/My). The `GPlates` model as well as the model by *Torsvik et al*. (2010) show a strong decrease in net rotation at 45 Ma compared to 55 Ma: 0.20°/My and 0.08°/My, respectively. The net rotation in the dynamic model, still at 0.11°/My, is more similar to these predictions at this time.

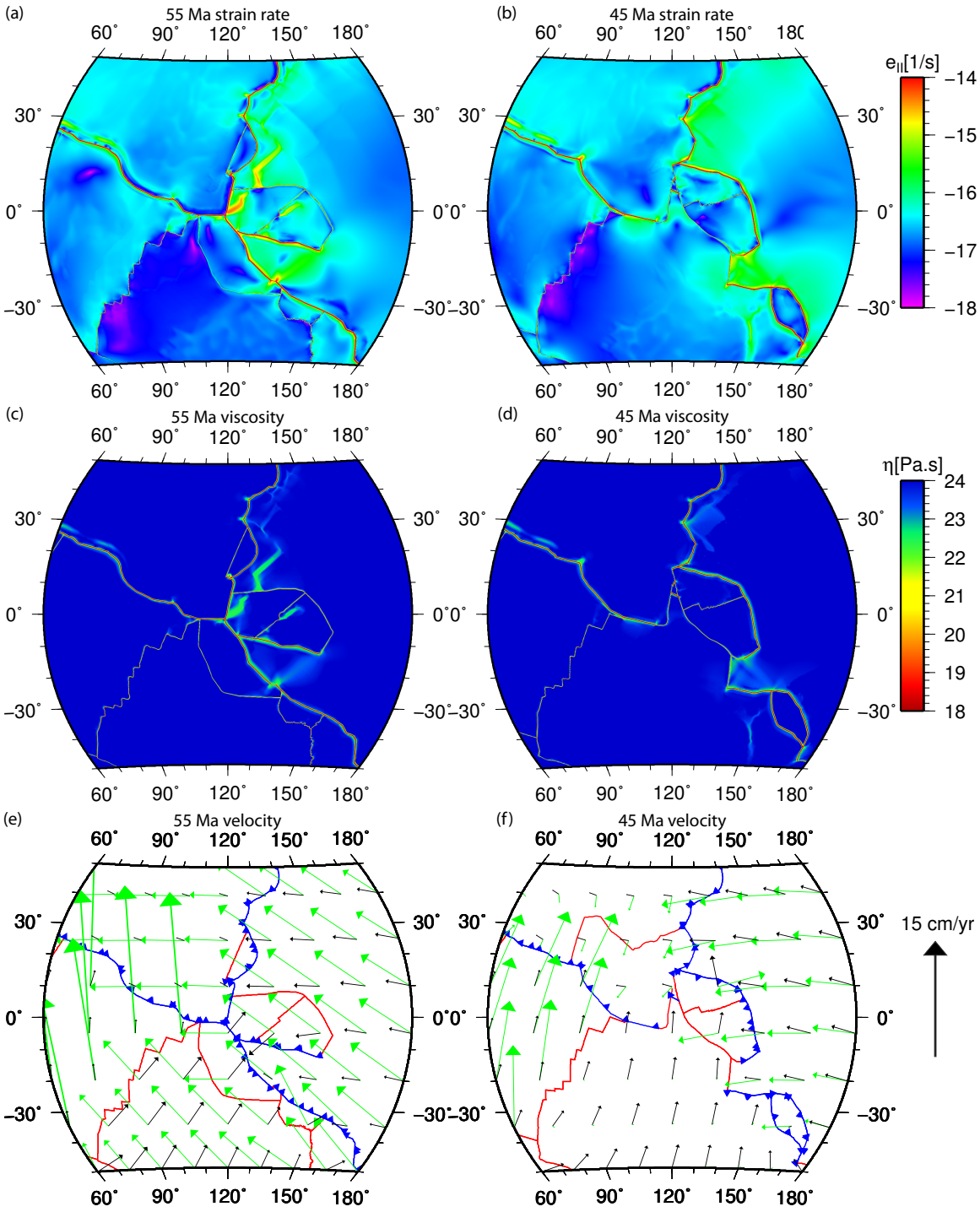

Figure 4.5. Map view of modeled surface quantities; zoom-in on the western Pacific at 55 Ma (left) and 45 Ma (right). (a)–(b): Second invariant of the strain rate; (c)–(d): Viscosity; (e)–(f): Velocities from the dynamic model (black) and from plate reconstructions (green). No line data is plotted in the viscosity and strain rate panels.

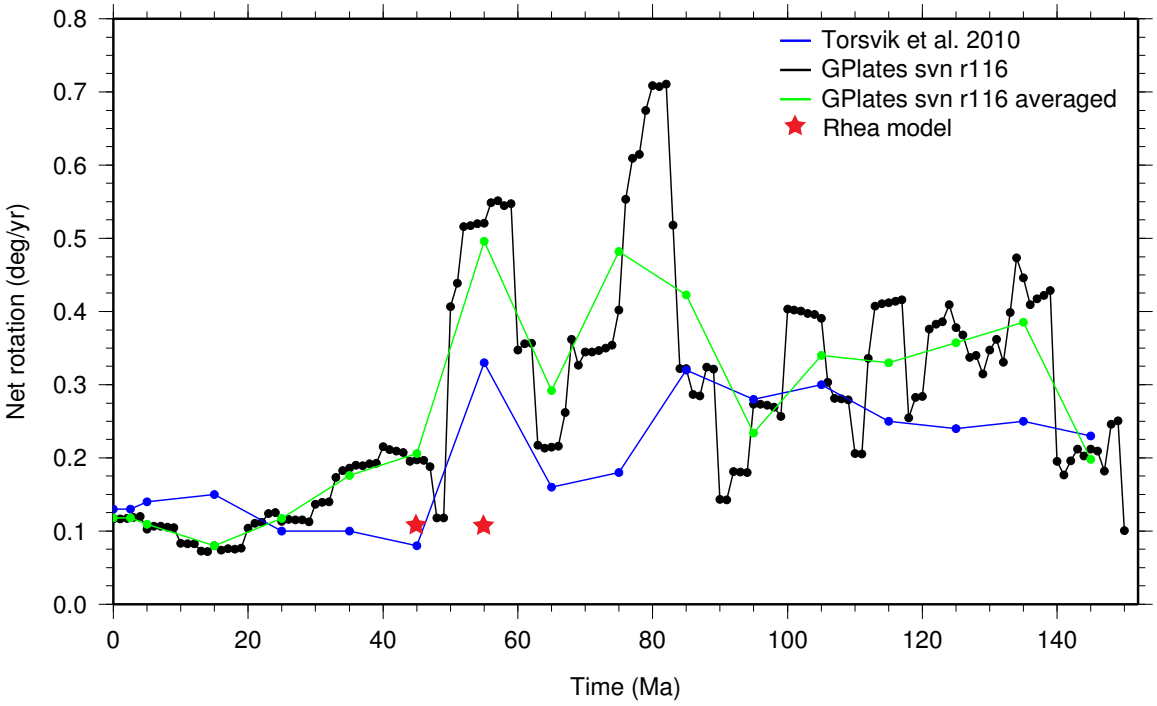

Figure 4.6. Time evolution of global net surface rotation. Blue: Prediction by *Torsvik et al.* (2010). Black: `GPlates` reconstruction used in this chapter. Green: `GPlates` net rotation averaged in the same time intervals as used by *Torsvik et al.* (2010) for comparison. Red stars: net rotation resulting from the dynamic motion models.

4.4.3 Surface State of Stress

The state of stress at the surface in the western Pacific is complicated. An interesting feature is the rotation of stresses along the western boundary of the Pacific plate (Figure 4.7). At 55 Ma, there is strong tension in the subducting Pacific plate perpendicular to the trench at the southern end of the boundary with Eurasia, indicating that subduction is readily occurring there. Further toward the north along the same boundary, this is changing into compression perpendicular to the trench, denoting a stronger resistance to subduction. and a reduction in slab pull.

There are two areas with significant changes in the state of stress between 55 and 45 Ma: just east of the center of the study area where the Izu-Bonin-Marianas subduction zone initiated, and in the southeast corner where the Tonga-Kermadec subduction zone initiated. In both cases, the stress regime in the subducting plate near the new trench has changed from compressional or partly tensional to strongly tensional perpendicular to the trench. Plates that are now overriding are all in compression near these trenches.

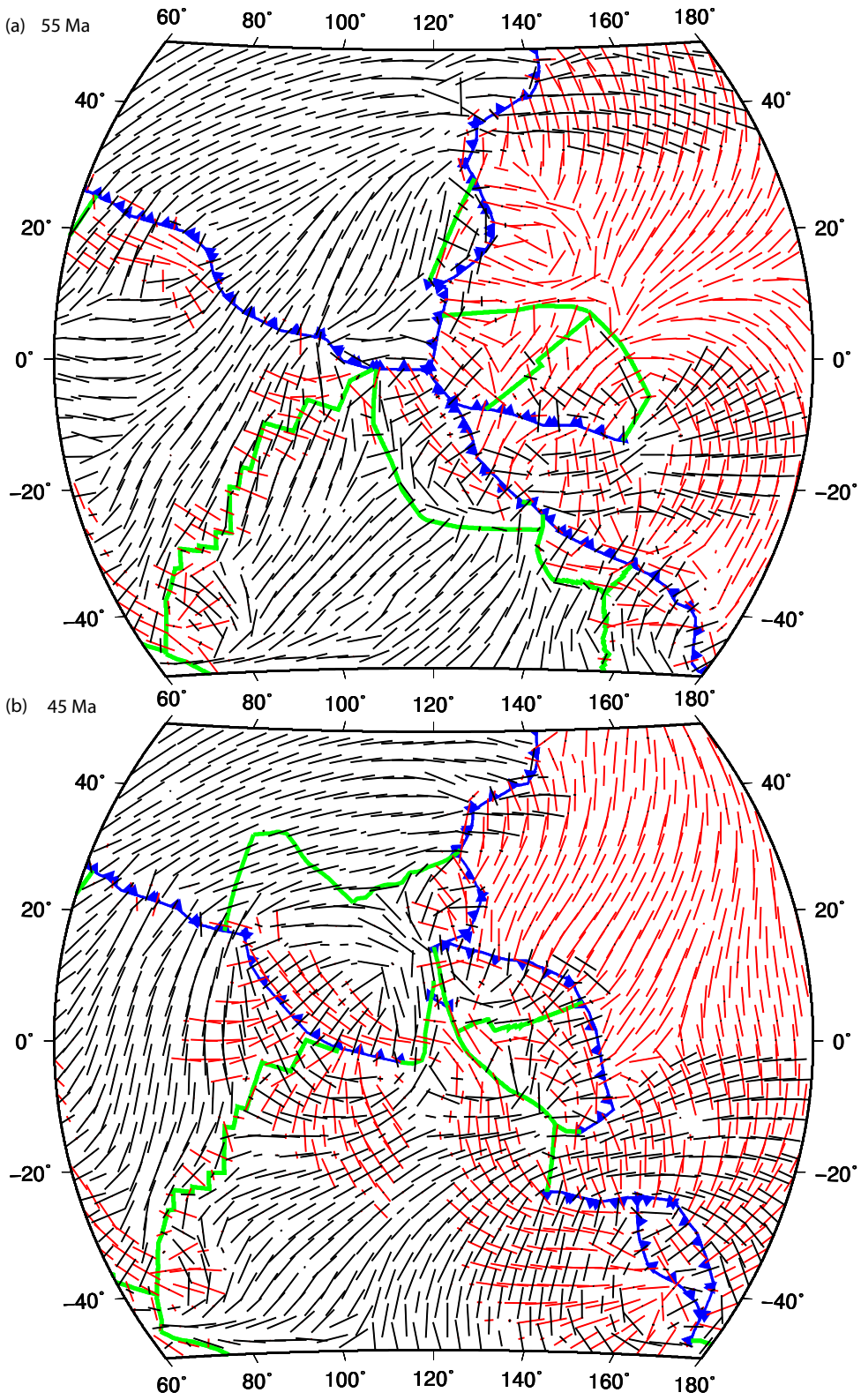

Figure 4.7. Map view of the surface state of stress, zoom-in on the western Pacific. (a) 55 Ma; (b) 45 Ma. Red dashes denote tension, black dashes show compression axes.

4.4.4 Slabs

We now focus on the slabs in cross-sections around the Pacific Ocean: the Proto-South China Sea (PSCS) where the western Pacific subducts beneath Eurasia (Figures 4.8a–b and 4.9a–b); the Kuriles further to the north on the same boundary (Figures 4.8c–d and 4.9c–d); California, where the Farallon plate subducts underneath North America (Figures 4.8e–f and 4.9e–f); and Peru, where the Farallon plate subducts underneath South America (Figures 4.8g–h and 4.9g–h); see Figure 4.3a for the exact locations of the cross-sections.

In the Proto-South China Sea, the Pacific plate is subducted more or less perpendicular to the trench. Between $\sim$ 300 and 660 km depth, the slab has a reduced viscosity from 10^{24} to $\sim 10^{22}$ Pa s compared to the shallow slab, and has a lower velocity than its surroundings in this depth interval (Figure 4.8a). The loss of strength causes the motion of the lower mantle continuation of the slab to be slightly decoupled from the upper mantle slab. The majority of the slab is in compression, apart from the hinge (Figure 4.8b). The subducting Pacific plate is in tension, indicating that the slab is indeed pulling the Pacific plate down. At 45 Ma, the slab viscosity further decreases, and with it the coupling between the upper and lower mantle segments (Figure 4.9a). The shallow slab experiences more tension now (Figure 4.9b). The Kurile slab shows a similar decoupling between the upper and lower mantle slab at 55 Ma: the viscosity in the 300–660 km "gap" is only $\sim 5 \times 10^{20}$ Pa s (Figure 4.8c). The Pacific plate is in compression and subducts slowly, since there is not much negative buoyancy attached to it to pull it down. The difference with the PSCS cross-section reflects the increase in resistance towards the north to subduction of the Pacific plate that was indicated by rotation of surface stresses. The upper mantle slab is in significant tension, transitioning to compression below 400 km depth (Figure 4.8d). The lower mantle is hardly moving, and does not appear to be coupled to the upper mantle flow. At 45 Ma, the upper mantle slab is even more decoupled

from the lower mantle high-viscosity structure, resulting in more significant tension (Figure 4.9c–d). The slab break-off at the East Asian subduction zone related to the arrival of the Izanagi-Pacific Ridge prior to 55 Ma resulted in slumping or avalanching of the slab remnant beneath the Pacific-Eurasia plate boundary, folding back on top of itself (visible in Figure 4.3b–c). This is illustrated by the tensional stress regime of the Pacific plate in the vicinity the East Asian subduction zone and in the still connected shallow slab.

On the other side of the Pacific ocean in California, there is more significant flow in the upper mantle around slabs. The Farallon slab is more strongly connected to the lower mantle compared to the western Pacific cross-sections (Figure 4.8e). The effect of lower mantle structure on dynamics is prominent: the velocities strongly decrease from the upper to the lower mantle as well as in the broad high-viscosity section of the slab just above the transition zone. In this case, the sharply defined and highly viscous lower mantle slab remnants inhibit the subducting slab motion, which is also indicated by the strong compressional regime throughout the entire slab (aside from its hinge which is in tension; see Figure 4.8f). The high-viscosity core of the slab extends deeper at 45 Ma, such that compression is even more dominant in the slab (Figure 4.9e–f). The slab in the Peru cross-section shows different behavior. The flow between upper and lower mantle is fully coupled at both 55 and 45 Ma, with a slab that has a high-viscosity core from the surface to the lower mantle (Figures 4.8g and 4.9g). This results in tension throughout the entire slab, as it is able to efficiently pull down the subducting plate (Figures 4.8h and 4.9h).

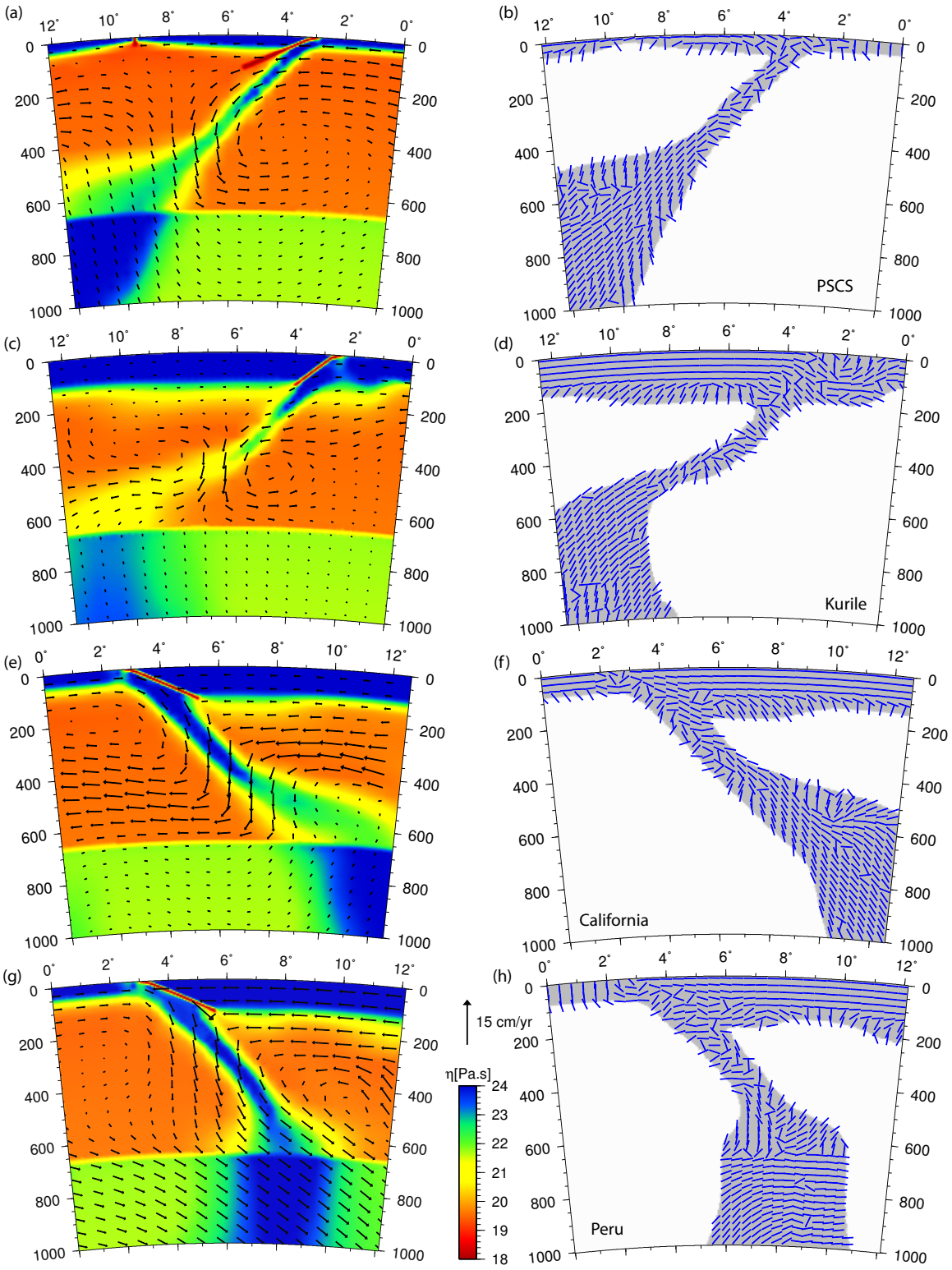

Figure 4.8. Cross-sections through subducting slabs at 55 Ma. Left column: viscosity and velocity. Right column: compression axes of unit length, with the grey background denoting the area with $T < 0.9$. (a)–(b): Proto-South China Sea (PSCS); (c)–(d) Kurile; (e)–(f) California; (g)–(h) Peru. See Figure 4.3a for the cross-section locations.

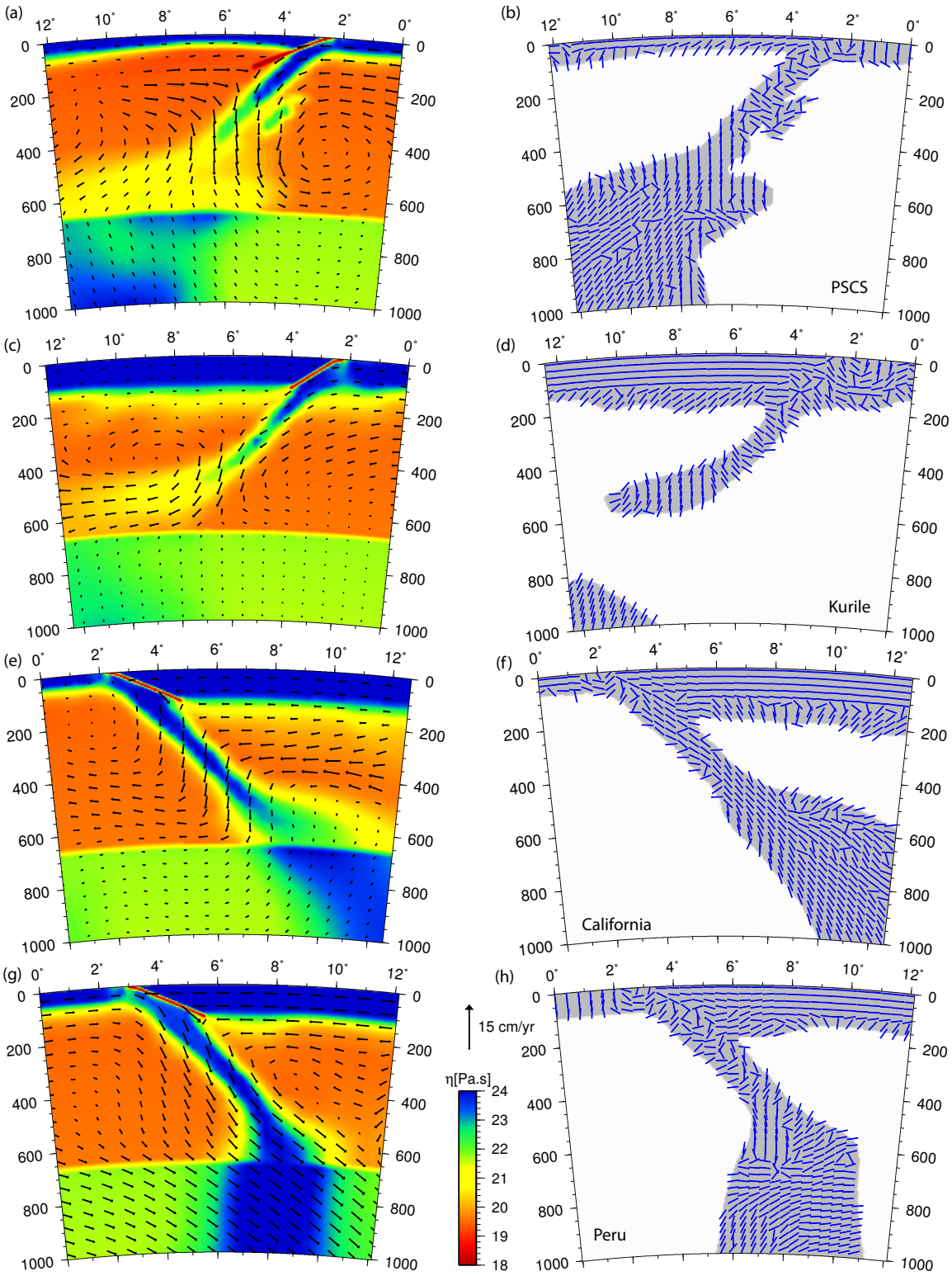

Figure 4.9. Cross-sections through subducting slabs at 45 Ma. Left column: viscosity and velocity. Right column: compression axes of unit length, with the grey background denoting the area with $T < 0.9$. (a)–(b): Proto-South China Sea (PSCS); (c)–(d) Kurile; (e)–(f) California; (g)–(h) Peru. See Figure 4.3a for the cross-section locations.

Overall, several patterns emerge. Plates only efficiently subduct when the upper mantle slabs are sufficiently connected to their lower mantle counterparts. This effect, or the lack of it, becomes evident in the northwestern Pacific (Figure 4.10): the high viscosity segments at 700 km depth in that area do not correspond to slabs outlined by low temperature at 600 km depth. This missing pull could be a cause for the misfit of the Pacific plate motion, which moves too much to the west without the predicted significant northerly component. In contrast, a strong overlap of the slab outline at 600 km depth and high-viscosity structures at 700 km depth in Central and South America corresponds to strongly coupled slabs. This difference in behavior between the western Pacific and the Americas can be attributed to the age of the plate subducted in the preceding period. In the PSCS and Kurile area, the young Izanagi plate and the Izanagi-Pacific Ridge were just subducted, leading to a thin slab with limited coupling. The Farallon plate subducted beneath California and especially under Peru was significantly older, resulting in thick and strongly coupled slabs, with connected lower mantle structures that dip almost vertically into the mantle. An even more extreme example can be seen in southern Eurasia, where the very old and thick African plate is subducting, resulting in strongly connected slabs.

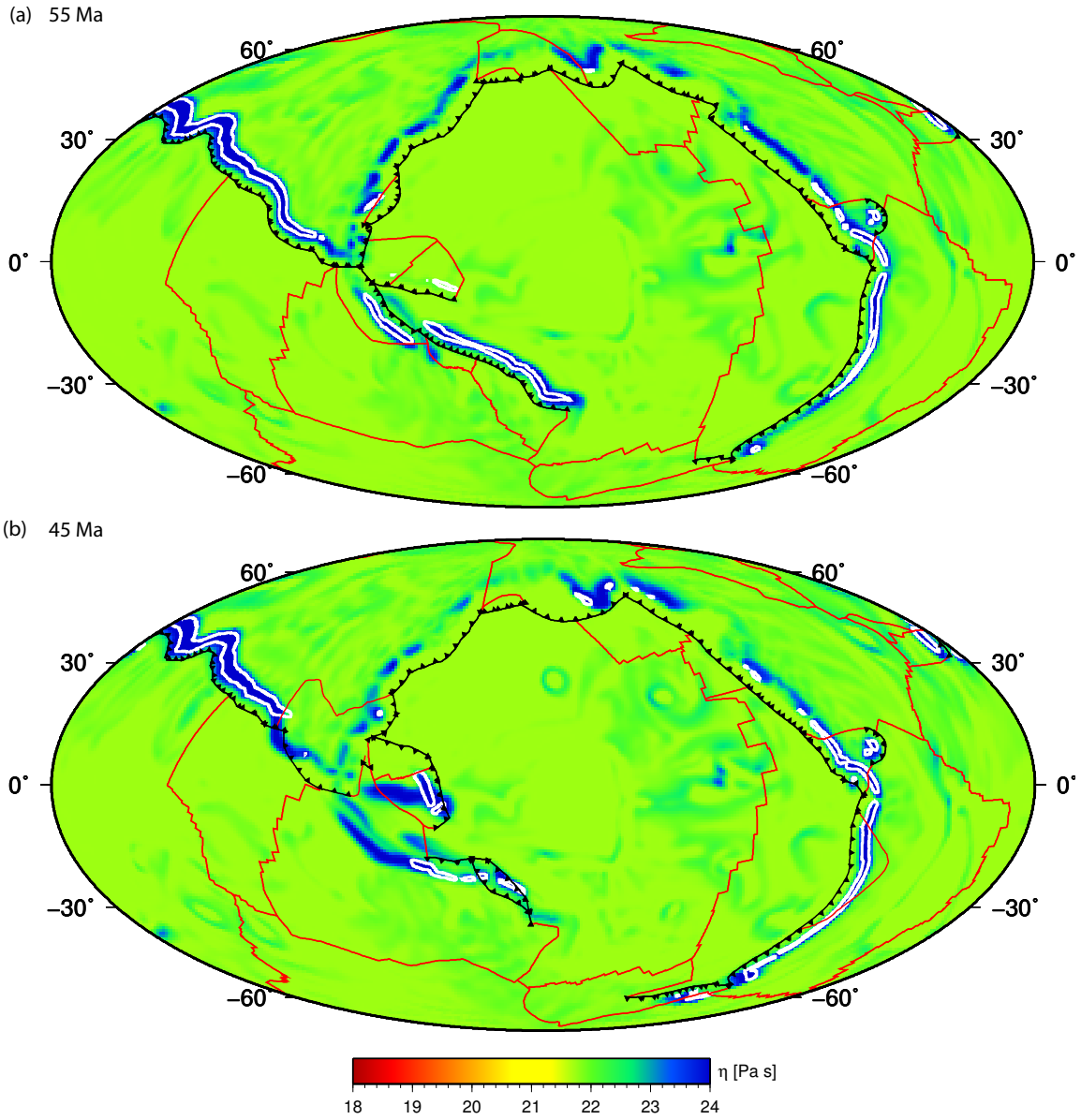

Figure 4.10. Viscosity field at 700 km depth (color map), with slab contours at 600 km depth plotted in white contours. The contours are defined by the nondimensional temperature $T = 0.8$.

4.4.5 Lateral Mantle Flow

The stationary upwelling under the central Pacific, corresponding to the Hawaiian hotspot location, dominates the sub-Pacific flow pattern (Figure 4.11). Flow beneath continents appears irregular, being dominated by small-scale drips from the lithosphere that have a higher viscosity compared to the ambient mantle. These features may decrease the ability of the continental lithosphere to decouple from the upper mantle, and hence they slow continental plate motion.

The presence of slabs affects lateral flow in the mantle. The pattern in the western Pacific shows that trench-perpendicular flow is dominant. Especially at 400 km depth, the largest lateral flow occurs through gaps in the subducting Pacific slab, where the flow is funneled and accelerated. The initiation of the Izu-Bonin-Marianas and Tonga-Kermadec subduction prior to 45 Ma causes the flow pattern at 45 Ma to locally diverge from that at 55 Ma. However, the overall pattern at 400 km depth is not significantly altered, and differences at 800 km depth are more or less indiscernable. This implies that it is unlikely that general sub-Pacific mantle flow could be altered or slowed by the subduction of slabs in the IBM and TK subduction zones, as was suggested by *Whittaker et al*. (2007). Instead, changes in flow patterns are highly localized, likely due to the nonlinear rheology. In areas where flow is enhanced such as around slabs, the high strain rate will lower the viscosity, which further increases velocities but also limits the extent of the area affected by the presence of the slab.

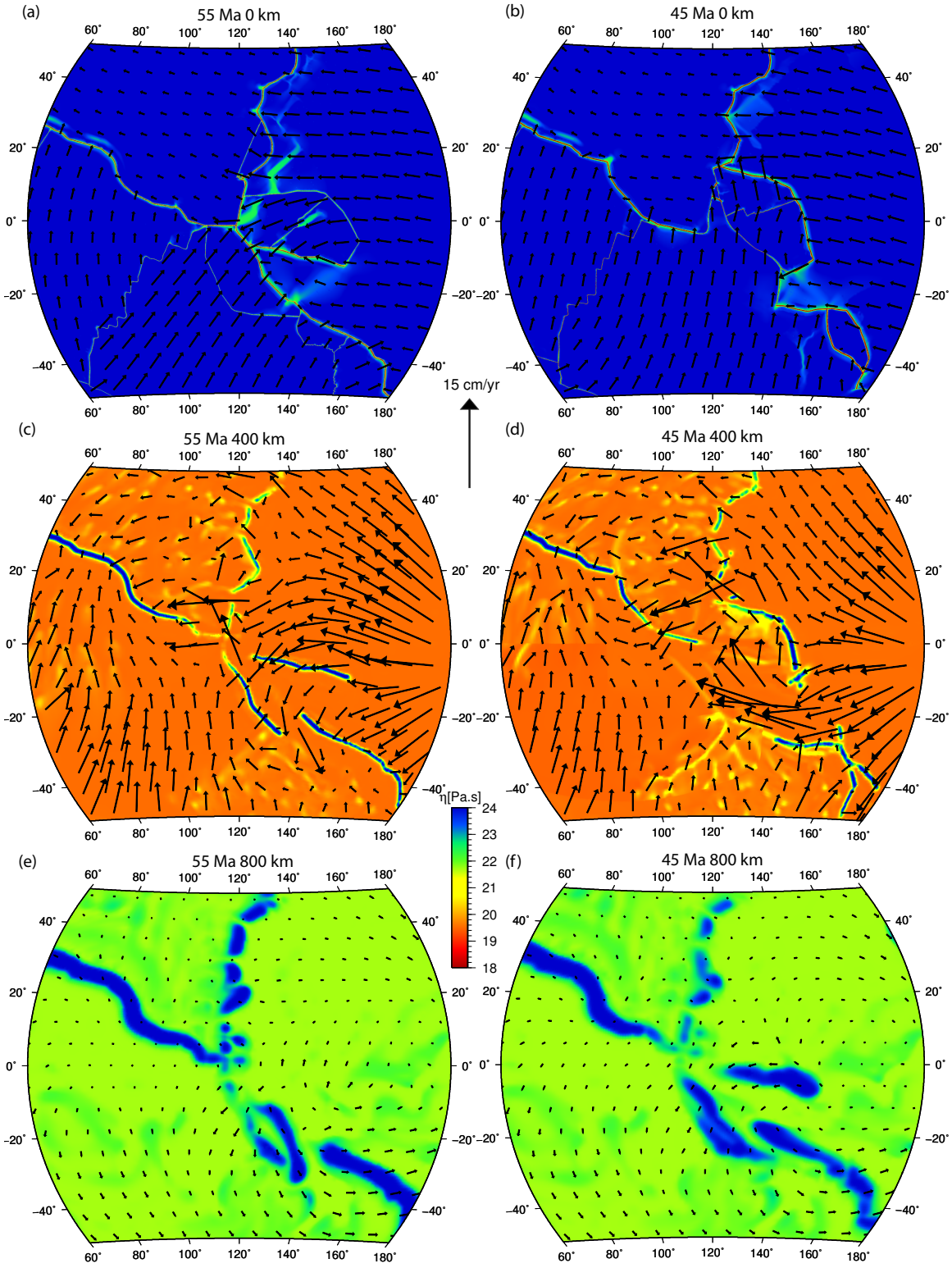

Figure 4.11. Map view of lateral mantle flow plotted on viscosity, zoom-in on western Pacific; 55 Ma (left) and 45 Ma (right). (a)–(b): Surface; (c)–(d): 400 km depth; (e)–(f): 800 km depth.

4.5 Discussion

Despite the implementation of a nonlinear rheology and detailed reconstructed plate boundaries, lithospheric thickness, and assimilated slabs with their appropriate age, plate motions only change slowly between 55 and 45 Ma, which results in a poor fit of plate motions in the dynamic convection models to predictions from paleo plate reconstructions. We are therefore currently not able to reproduce the rapid plate reorganizations.

Several important model aspects have come to light. A major difference with the present-day models of Chapter 3 is the nature of the lower mantle viscosity. The tomography used for the present-day models results in smooth, broad high-viscosity features. In contrast, advected slabs in a convection model remain much sharper with higher viscosities. Depending on the morphology of the slab remnants, these sharply defined features in the lower mantle can add significant slab pull to the subducting plate when they are narrow and steeply dipping, such as beneath Peru. They can also act as brakes on subduction when the slab has folded back onto itself, forming an anchor in the lower mantle, much like the broad features in the present-day models. This suggests that the details of the lower mantle structure, and therefore parameter choices in the time-dependent models, strongly affect outcomes of these instantaneous models. In the models presented here, the lower mantle structures dominate the model dynamics, such that relatively small changes in plate boundary configurations do not significantly affect plate motions. Similarly, these stationary features anchor the overall flow, including the plates, allowing little motion of the surface with respect to the lower mantle (i.e., a small net rotation).

The amount of coupling within slabs and between slabs and plates is directly affected by the age and therefore the thickness of the subducted slab: older, thicker slabs such as the

Farallon slab connect lower mantle structure to plates more strongly than younger, thinner ones such as Izanagi. The coupling of slabs with the surrounding mantle depends on slab morphology and the ambient viscosity: in the upper mantle with a relatively low viscosity, the flow affected by thin slabs is limited in its spatial extent. This implies that the descending slabs in the Izu-Bonin-Marianas and Tonga-Kermadec subduction zones are not likely to be responsible for the slowdown of the sub-Pacific mantle, as was suggested by *Whittaker et al.* (2007).

We do not observe the extension of the overriding plate following initiation of the IBM subduction zone that was predicted by *Hall et al.* (2003) to explain inferred catastrophic boninitic volcanism associated with the subduction initiation. This extension in the overriding plate is however not expected to be seen in global dynamic models, as these regional models are time dependent and there is a strong feedback between the slab and development of spreading on the overriding plate.

Potential improvements to the instantaneous dynamic models could be made by using time dependent models for the mantle structure that have fewer slab remnants in the lower mantle. If a plate model instead of a half-space cooling model is used such that the subducting slab age is truncated at 80 Ma (see, e.g., *Steinberger and Torsvik* (2010)), slab thickness and therefore the lifespan of slabs in the lower mantle would be reduced. This would promote overall flow in the mantle, and could possibly increase the ability of slabs to subduct into the lower mantle more easily. In addition, the higher-viscosity lithospheric drips underneath the continents possibly add resistance to motion of the plates in the form of basal drag; their removal by, e.g., implementing a more realistic continental age distribution could enhance overall plate speeds and fit to predicted plate motions. Furthermore, it would be instructive to compute a dynamic model prior to the slab break-off at the East Asia subduction zone (at, e.g., 65 Ma), such that

the effect of the presence of slabs and slab break-off on global plate motions and state of stress can be studied more closely. Another interesting topic for further investigation is the evolution of the net surface rotation and its discrepancy between the dynamic plate motion models, the plate reconstruction model, and the reconstructions by *Torsvik et al.* (2010).

4.6 Conclusions

We computed high-resolution dynamic global convection models at 55 and 45 Ma in order to study the plate reorganization taking place around 50 Ma. These instantaneous models are constructed using the result of lower-resolution time-dependent models to populate mantle structure. Slab remnants in the lower mantle are abundant and sharply defined with high viscosities, and strongly influence plate motions and flow in the mantle interior. While modeled plate motions do not show a good fit to reconstructed plate motions, it has become apparent that slab age is an important factor in slab pull, through coupling between plates and slabs and between upper and lower mantle sections of slabs. We further find that subducting slabs are not capable of affecting lateral flow in the upper mantle on a large scale, and therefore we conclude that it is unlikely that the slabs in the western Pacific are responsible for the slowing of sub-Pacific flow after the initiation of their subduction.

Acknowledgements

We would like to thank Kara Matthews for her work on the `GPlates` plate reconstructions resulting in the plate boundary weak zones, Maria Seton for the age grid reconstructions, and Dan Bower and Nico Flament for making their `CitcomS` convection models available. Discussions with Dietmar Müller and Trond Torsvik were also highly beneficial. This work

was partially supported by the NSF PetaApps program (OCI-0749334, OCI-0748898), NSF Earth Sciences (EAR-0426271, EAR-0810303), and the Caltech Tectonics Observatory (by the Gordon and Betty Moore Foundation). Computing resources on TACC Lonestar and Spur systems were provided through the NSF TeraGrid under grant number TG-MCA04N026. The figures were produced using Generic Mapping Tools (GMT) and Paraview.

Chapter 5

Summary and Outlook

5.1 Summary

In this thesis, I have addressed the modeling of mantle convection with plates, utilizing adaptive mesh refinement techniques so that small-scale features such as plate boundaries and localized deformation in plates and slabs can be resolved. In this chapter, the main findings are summarized and put into context of our current understanding of mantle dynamics.

The rheology of plates, slabs, and the surrounding mantle The models presented in this thesis indicate that model constraints such as plate motions and plateness are best met when plates and slabs are strong, with a viscosity of $\sim 10^{24}$ Pa s. Localized strain-rate weakening reduces the viscosity to $\sim 10^{22}$ Pa s or less in plate hinges. The spatial extent and amount of this weakening depends on slab morphology and motion, and on the rheology (specifically the yield stress and stress exponent). Plate boundaries have a low viscosity of $\sim 10^{18}$ Pa s, so that they effectively decouple plates from one another. The (de)coupling between plates is an important aspect of these models: local changes in plate boundary strength significantly affect the plate motions and surface state of stress in a much larger area. For example, increasing the plate boundary strength in Peru affects stress orientations in the entire South America

and Nazca plates. This behavior illustrates the highly nonlinear nature of the models, and demonstrates that the spatial variation of plate boundary strength is an important future avenue of research.

The debate in literature of weak versus strong slabs is partly the result of differences between linear and nonlinear rheology: studies using a linear rheology effectively only assess the average viscosity of slabs, whereas nonlinear rheology allows for localized weakening in otherwise strong slabs.

Coupling between plates, slabs, and the surrounding mantle The strong plates and slabs in the convection models are able to act as highly effective stress guides. Coupling between surrounding mantle and slabs is high, given that the velocity field is continuous from the slabs to the surrounding mantle. Changes in yield stress and stress exponent directly affect the velocity magnitude in plates, slabs, and asthenosphere, but these in turn affect the entire mantle flow. The distribution of energy dissipation in the mantle is also indicative of coupling between mantle, slabs, and plates. Pointwise, the dissipation is highest in bending plates, which is also indicated by the significant strain-rate weakening there. By volume, the majority of dissipation takes place in the lower mantle. This is in contrast to earlier studies where the bending dissipation was viewed as the dominant process.

The importance of lower mantle structure for plate tectonics Lateral viscosity variations in the lower mantle can affect plate motions, depending on whether high-viscosity structures are directly beneath (and connected with) subducting slabs. Generally, subducting slabs are slowed by the presence of broad, high-viscosity, lower mantle features which act as a “braking force”. Stresses are transmitted upward from the lower mantle structures or the tip of the subducting slabs into the plates, and therefore these lower mantle structures affect surface ve-

locities. In contrast, overriding slabs are sped up by increased lower mantle viscosity variation due to the added buoyancy in the convective system. This behavior fits the hypothesis of strong coupling throughout the convective domain. It is therefore essential to include lower mantle lateral viscosity variation in mantle convection models. Consequently the details of tomography models affect model results, especially for the mid-mantle, as the continuity between the slab and underlying anomaly is very important. For example, the tomography model used for the convection model does not contain a section of the Sandwich slab below $\sim$ 300 km depth, resulting in trench rollback that is significantly slower than observations indicate.

Regional dynamics in globally consistent convection models In order to model regional dynamics, it is important to include the global mantle flow, especially when a nonlinear rheology is used. Depending on choices in rheology, the global models are able to reproduce observed details in surface motions, such as trench rollback and microplate motion. Flow around subducting slabs is mostly trench-perpendicular, indicating that it is mainly driven by the downgoing motion of the slab. The models do not display significant trench-parallel flow components and therefore do not match simple predictions from seismic anisotropy studies. The only trench-parallel flow in our models is around the edges of slabs, and in areas where the proximity of multiple slabs creates complex flow patterns. The velocity orientation and magnitude, as well as yielding in slabs, are linked to slab morphology and dip, plate motion, trench rollback, and the presence and continuity with lower mantle structure beneath the slab.

The effect of regional geometry versus rheology on modeled quantities Plate velocity is predominantly governed by the amount of negative buoyancy attached to the plate in the form of subducting slabs, modulated by the amount of deformation determined by the rheology. Microplates are more significantly affected by stress exponent as they require a very strong de-

coupling from other plates. The state of stress and the direction of plate motions are primarily governed by plate and slab geometry; variation in rheology does not result in consistent trends in either quantity.

Causes of rapid plate reorganizations in the geologic past In light of the previous conclusions, it is to be expected that both mantle flow and temporal changes in plate tectonics play a part in reorganizations; they are necessarily strongly coupled phenomena. The model dynamics are dominated by the size, morphology, and strength of slab remnants in the lower mantle, such that rapid changes in surface motions have proven difficult to reproduce. The additional uncertainties in plate reconstructions and mantle structure make modeling in the geologic past even more challenging than for the present. For example, there are significant discrepancies in the net rotation among different paleo plate reconstructions, and details of the mantle structure in the past are virtually unknown.

5.2 Outlook

The advances in mantle convection modeling described in this thesis open up various avenues of future work. First of all, the problem of reproducing rapid changes in the motion of major plates in a dynamic flow model remains. Much could be learned from experimenting with various time-dependent models used to construct the mantle structure, especially ones with different slab lifespans. Additionally, the inclusion of active upwellings in both present-day models and in the historic models would allow for study of the effects of plumes and their interaction with ridges on plate motions. A major question still open is the effect of variation in plate boundary strength on plate motions, which could be studied in more detail in a systematic manner. This could be coupled with local tectonic indicators of plate boundary

strength, for instance in areas where ridges are being subducted. Furthermore, time-dependent convection models would allow time evolution of weakening and would pose an additional constraint on rheology, given that plates and slabs must be able to retain their strength over significant intervals of time. Such time-dependent models would also provide a more realistic way to model plate reorganizations, including features such as temporal plume-ridge interaction.Because the paleo plate reconstructions are the only global means currently at hand to structurally verify these convection models, it is paramount that improvements to the reconstructions continue being made, especially with respect to the net rotation.

Appendix A

Benchmarks

Submitted as:

Burstedde, C., Stadler, G., Alisic, L., Wilcox, L. C., Tan, E., Gurnis, M., & Ghattas, O. Large-scale adaptive mantle convection simulation, *Geophysical Journal International*.

A.1 Abstract

A new-generation, parallel adaptive-mesh mantle convection code, `Rhea`, is described and benchmarked. `Rhea` targets large-scale mantle convection simulations on parallel computers, and thus has been developed with a strong focus on computational efficiency and parallel scalability of both mesh handling and numerical solvers. `Rhea` builds mantle convection solvers on a collection of parallel octree-based adaptive finite element libraries that support new distributed data structures and parallel algorithms for dynamic coarsening, refinement, rebalancing, and repartitioning of the mesh. In this study we demonstrate scalability to 122,880 compute cores and verify correctness of the implementation. We present the numerical approximation and convergence properties using 3D benchmark problems and other tests for variable-viscosity Stokes flow and thermal convection.

A.2 Introduction

Solid earth dynamics are governed by processes that occur over a wide range of time and length scales. A classic example is plate tectonics, where the large-scale motion of plates over time scales of millions of years and length scales of thousands of kilometers intimately couples to seismic processes that occur at time scales of minutes and less over lengths scales generally under 100 km. The upwellings associated with mantle convection are also typified by a wide range of length scales with large super plumes 1000s of km across with small plumes detaching from their periphery that have thermal and mechanical boundary layers 100s of meters in thickness. Many of the transport processes that occur in mantle convection are thermo-chemical where chemical boundaries (for example next to subducted oceanic crust) can be sharp over sub-meter length scales.

The advent of petascale computing promises to make multiscale simulations of mantle convection and plate tectonics possible. Still, capturing global convection processes at realistic Rayleigh numbers requires resolution down to faulted plate boundaries. A uniform discretization of the mantle at, for instance, 1 km resolution would result in meshes with nearly a trillion elements, which is far beyond the capacity of the largest available supercomputers. An alternative is to employ adaptive mesh refinement and coarsening (AMR) methods that can reduce the number of unknowns drastically by placing resolution only where needed. Thus, AMR has the potential to enable high-resolution global mantle convection simulations, and to reduce the simulation wallclock time for many mantle convection problems significantly. Unfortunately, the added complexity of AMR methods can also impose significant overhead, in particular on highly parallel computing systems, due to the need for frequent re-adaptation and repartitioning of the mesh over the course of the simulation. Several recent studies have applied AMR

methods to mantle convection, including *Davies et al.* (2007); *Stadler et al.* (2010); *Leng and Zhong* (2011); *Davies et al.* (2011).

Here, we present the numerical strategies behind and verification of `Rhea`, a new generation adaptive mantle convection code that scales to hundreds of thousands of processors and has negligible overhead for all operations related to mesh adaptation. `Rhea` builds solvers for mantle convection problems on a collection of new libraries for parallel dynamic AMR (*Burstedde et al.*, 2008a). It integrates parallel finite elements with forest-of-octrees-based mesh adaptivity algorithms and includes support for dynamic coarsening, refinement, rebalancing, and parallel repartitioning of the mesh. `Rhea` implements a parallel variable-viscosity nonlinear Stokes solver, based on Krylov solution of the (stabilized) Stokes system (*Burstedde et al.*, 2009b), with preconditioning carried out by approximate block factorization and algebraic multigrid (AMG) V-cycle approximation of the inverse of the viscous and pressure Schur complement operators.

`Rhea` has been used previously to compute lithospheric and mantle flow models with resolutions below 1 km near fault and subduction zones, and generally in areas where strain-weakening is observed; see *Stadler et al.* (2010) and *Alisic et al.* (2010). Here the parallel capabilities of `Rhea` have been essential to routinely perform simulations using $\mathcal{O}(10^4)$ compute cores. In this paper, we discuss the parallel adaptive mesh capabilities, as well as the solvers used in `Rhea` in more detail. To verify the correctness of the implementation and to study convergence of the solution we use problems for which the exact solution is known, as well as benchmark problems previously used in the literature. Furthermore, we demonstrate that for problems of high Rayleigh number, adaptive meshes yield smaller errors compared to uniform meshes of the same element count, and report significant savings in the number of degrees of freedom and the overall run time compared to highly resolved uniform meshes.

A.3 Mantle Convection Equations

The dynamics of mantle convection are governed by the equations of balance of mass, linear momentum, and energy. Under the Boussinesq approximation for a mantle with uniform composition and the assumption that the mantle deforms as a viscous medium, the nondimensionalized version of these equations reads (e.g., *McKenzie et al.* (1974); *Zhong et al.* (2000)):

$$\nabla \cdot \mathbf{u} = \mathbf{0}, \tag{A.1}$$

$$\nabla p - \nabla \cdot \left[\mu(T, \mathbf{u}) \left(\nabla \mathbf{u} + \nabla \mathbf{u}^{\top}\right)\right] = \mathrm{Ra}\, T\, \mathbf{e}_r, \tag{A.2}$$

$$\frac{\partial T}{\partial t} + \mathbf{u} \cdot \nabla T - \nabla^2 T = \gamma, \tag{A.3}$$

where $\mathbf{u}$, $\mathbf{p}$, μ, and T are the velocity, pressure, temperature- and strain-rate-dependent viscosity, and temperature, respectively; γ is the rate of internal heat generation; $\mathbf{e}_r$ is the unit vector in the radial direction; and Ra is the Rayleigh number that controls the vigor of convection and is defined as $\mathrm{Ra} = \alpha\rho_0 g \Delta T D^3/(\kappa\mu_0)$. Here α, ρ_0, μ_0, and κ are the reference coefficients of thermal expansion, density, viscosity, and thermal diffusivity, respectively; ΔT is the temperature difference across a mantle with thickness D, and g is the gravitational acceleration. We use top and bottom radii $r_t = 1$, $r_b = 0.55$ throughout, which determines $D = 0.45$. The boundary conditions (not shown) specify zero normal velocities and zero tangential traction at both the free surface and the core-mantle boundary, and impose fixed boundary temperature values.

Equations (A.1) and (A.2) are instantaneous and need to be satisfied at all times. Together they describe a nonlinear Stokes system of partial differential equations that needs to be solved for velocity and pressure. The energy equation (A.3) captures the evolution of the mantle and

needs to be integrated forward in time, which is done after space discretization transforms it into a system of ordinary differential equations. Consequently, the numerical solution methods for these two systems as discussed in the next section are substantially different.

A.4 Discretization and Solvers

For the discretization of the temperature, velocity, and pressure in (A.1)–(A.3), we use (tri-) linear finite elements on locally refined hexahedral meshes. These meshes are adapted to resolve features of the velocity, pressure, or viscosity fields. Practical challenges, as well as the technical details required for parallel adaptive simulations, are discussed in Section A.5. In this section, we focus on the discretization and on the solvers used in `Rhea`. Due to the large size of the matrices that result from the discretization, linear systems cannot be solved using direct factorization-based solvers but have to be solved using iterative solution algorithms.

A.4.1 Variational Formulation of Stokes Equations

The finite element discretization is based on the weak form of the system of partial differential equations derived from (A.1) and (A.2) by multiplication with admissible test functions $\mathbf{v}$ and q (omitting the differentials $\mathrm{d}\boldsymbol{x}$, etc., for brevity),

$$\int_\Omega \Big[\nabla\cdot\Big(p\mathbf{I}-\mu(\nabla\mathbf{u}+\nabla\mathbf{u}^\top)\Big)-\mathbf{f}\Big]\cdot\mathbf{v}=0 \quad \text{for all } \mathbf{v}, \tag{A.4a}$$

$$\int_\Omega (\nabla\cdot\mathbf{u})\,q=0 \quad \text{for all q}, \tag{A.4b}$$

and integration by parts which yields

$$A(\mathbf{u},\mathbf{v}) + B(\mathbf{v},p) + E(p,\mathbf{u},\mathbf{v}) = F(\mathbf{v}) \quad \text{for all } \mathbf{v}, \tag{A.5a}$$

$$B(\mathbf{u},q) = 0 \qquad \text{for all } q, \tag{A.5b}$$

where we use the definitions

$$A(\mathbf{u},\mathbf{v}) = \int_\Omega \frac{\mu}{2}(\nabla\mathbf{u} + \nabla\mathbf{u}^\top) : (\nabla\mathbf{v} + \nabla\mathbf{v}^\top), \tag{A.6a}$$

$$B(\mathbf{u},q) = -\int_\Omega (\nabla\cdot\mathbf{u})\, q, \qquad F(\mathbf{v}) = \int_\Omega \mathbf{f}\cdot\mathbf{v}, \tag{A.6b}$$

$$E(p,\mathbf{u},\mathbf{v}) = \int_{\partial\Omega} \Big[\Big(p\mathbf{I} - \mu(\nabla\mathbf{u} + \nabla\mathbf{u}^\top)\Big)\,\mathbf{n}\Big]\cdot\mathbf{v}, \tag{A.6c}$$

and $\mathbf{f} = \mathrm{Ra}\,T\,\mathbf{e}_r$ denotes the volume force. When we impose free-slip boundary conditions on $\partial\Omega$, namely

$$\mathbf{u}\cdot\mathbf{n} = 0, \qquad \mathbf{v}\cdot\mathbf{n} = 0, \tag{A.7a}$$

$$\mathbf{t}\cdot\Big[\Big(p\mathbf{I} - \mu(\nabla\mathbf{u} + \nabla\mathbf{u}^\top)\Big)\,\mathbf{n}\Big] = \mathbf{0}, \tag{A.7b}$$

for an outside normal vector $\mathbf{n}$ and any tangential vector $\mathbf{t}$, we see that the term in (A.6c) vanishes.

The discrete Stokes problem can then be written as the following saddle point system of equations:

$$\boldsymbol{Q}\begin{pmatrix}\hat{\mathbf{u}}\\ \hat{\mathbf{p}}\end{pmatrix} = \begin{pmatrix}\hat{\mathbf{f}}\\ \mathbf{0}\end{pmatrix} \qquad \text{with} \qquad \boldsymbol{Q} = \begin{pmatrix}\boldsymbol{A} & \boldsymbol{B}^\top\\ \boldsymbol{B} & -\boldsymbol{C}\end{pmatrix}, \tag{A.8}$$

where $\hat{\mathbf{u}}$, $\hat{\mathbf{p}}$, $\hat{\mathbf{f}}$ denote the nodal values of the finite element approximations of $\mathbf{u}$, p, $\mathbf{f}$, respec-

tively, and the matrices $\boldsymbol{A}$, $\boldsymbol{B}$, $\boldsymbol{C}$ are defined by inserting the subset of finite element shape functions $\{\phi_n\}_n$ that satisfy the boundary conditions (A.7a) into the corresponding bilinear forms $A(\cdot\,,\cdot)$, $B(\cdot\,,\cdot)$, and $C(\cdot,\,\cdot)$. The purpose of the contribution

$$C(p,q) = \sum_{\Omega_e} \int_{\Omega_e} (p - \Pi p)(q - \Pi q) \tag{A.9}$$

is to stabilize the linear system (A.8). Here, Ω_e for $e = 1, 2, \ldots$ denote the finite elements and Π the L^2-projection onto the space of element-wise constant functions. This stabilization is necessary since linear elements for velocity and pressure do not satisfy the inf-sup condition for stability of numerical methods for saddle point problems; we refer to *Elman et al.* (2005); *Bochev et al.* (2006); *Dohrmann and Bochev* (2004) for details. The blocks $\boldsymbol{A}$ and $\boldsymbol{C}$ are symmetric and positive and, thus, (A.8) is an indefinite symmetric system.

The solution for the pressure is unique only up to a constant, which we address by penalizing the integral of the pressure over the domain. Concerning the velocity, all rigid-body rotations are non-trivial solutions to the homogeneous Stokes equations in a spherical geometry with free-slip boundary conditions. We remove this ambiguity by transforming the velocity field after each solve to a zero angular momentum state, as is done in *Zhong et al.* (2008).

A.4.2 Boundary Terms and Topography

The above derivation of the discrete Stokes system incorporates the free-slip boundary conditions, but at the same time removes information on the boundary traction from the formulation. Since the normal component of the traction vector,

$$s = \mathbf{n} \cdot \left[\left(p\mathbf{I} - \mu(\nabla \mathbf{u} + \nabla \mathbf{u}^\top) \right) \mathbf{n} \right], \tag{A.10}$$

is an important ingredient in determining the topography, we include a brief description of how it can be recovered in a postprocessing step.

Assuming a Stokes solution $(\mathbf{u}, p)$ that satisfies the boundary condition (A.7b), we can simplify the boundary term

$$E(p, \mathbf{u}, \mathbf{v}) = \int_{\partial\Omega} (\mathbf{v} \cdot \mathbf{n}) s. \tag{A.11}$$

Note that this term can also be introduced as part of a Lagrangian functional to enforce (A.7a) in a variational form; in this case the normal traction s is identified with the Lagrange multiplier for the normal velocity component.

Equations (A.5a) and (A.11) hold for arbitrary velocity fields $\mathbf{v}$, in particular those not satisfying $\mathbf{v} \cdot \mathbf{n} = 0$. We can exploit this fact by constructing a discretization of the normal field on the boundary,

$$\mathbf{v}(\boldsymbol{x}) = \sum_{n | \boldsymbol{x}_n \in \partial\Omega} \nu_n \mathbf{n}_n \phi_n(\boldsymbol{x}), \tag{A.12}$$

defined by a coefficient vector $\bar{\boldsymbol{\nu}} = \{\nu_n\}_n$ whose index n loops over the subset of finite element shape functions ϕ_n on the boundary, and $\bar{\mathbf{n}} = \{\mathbf{n}_n\}_n$ denotes the vector that contains the normals of all boundary nodes $\boldsymbol{x}_n$. Inserting this function $\mathbf{v}$ into (A.5a) and rearranging in terms of the coefficient vector $\bar{\boldsymbol{\nu}}$, we obtain a system of equations for the discretized normal traction $s = \sum_n s_n \phi_n$ with nodal values $\bar{\mathbf{s}} = \{s_n\}_n$,

$$\bar{\boldsymbol{M}} \bar{\mathbf{s}} = \left(\bar{\mathbf{f}} - \bar{\boldsymbol{A}} \hat{\mathbf{u}} - \bar{\boldsymbol{B}}^\top \hat{\mathbf{p}} \right) \cdot \bar{\mathbf{n}}. \tag{A.13}$$

Here the bar notation denotes matrices and vectors whose leading dimension corresponds to the boundary degrees of freedom, and the dot product is understood to collapse three

coefficients into one independently at each node. The surface mass matrix $\bar{\boldsymbol{M}}$ with entries

$$\bar{M}_{mn} = \int_{\partial\Omega} \phi_n(\boldsymbol{x})\phi_m(\boldsymbol{x})\mathrm{d}x \tag{A.14}$$

derives from the boundary integral in (A.11), with indices m, n restricted to the boundary nodes. In our numerical experiments we use a lumped version, that is a diagonal approximation, of $\bar{\boldsymbol{M}}$ that is easily invertible.

This procedure to obtain the normal traction is equivalent to the consistent boundary flux (CBF) described in *Zhong et al*. (1993). Note that the method can be modified to compute tangential tractions for problems with prescribed flow at the boundaries, as is the case when plate motions are imposed.

A.4.3 Stokes Solver

Since the coefficient matrix $\boldsymbol{Q}$ is symmetric and indefinite, we employ the preconditioned minimum residual iterative method (MINRES) for its numerical solution. MINRES (*Paige and Saunders*, 1975) is a generalization of the conjugate gradient method to indefinite systems. Each MINRES iteration requires one application of the matrix $\boldsymbol{Q}$ to a vector and two inner products. The overall number of vectors stored does not increase with the number of MINRES iterations, thus the memory footprint is small. For a comprehensive discussion of the approach used in `Rhea` see *Burstedde et al*. (2009b); for alternative approaches see *Elman et al*. (2005); *May and Moresi* (2008); *Geenen et al*. (2009).

To obtain a mesh-independent (or almost mesh-independent) number of iterations, i.e., a constant number of iterations as the problem size increases, one needs to employ a suitable preconditioner for (A.8). MINRES requires a symmetric and positive definite preconditioner.

The block factorization

$$\begin{pmatrix} \boldsymbol{A} & \boldsymbol{B}^\top \\ \boldsymbol{B} & -\boldsymbol{C} \end{pmatrix} = \begin{pmatrix} \boldsymbol{I} & \boldsymbol{0} \\ \boldsymbol{B}\boldsymbol{A}^{-1} & \boldsymbol{I} \end{pmatrix} \begin{pmatrix} \boldsymbol{A} & \boldsymbol{0} \\ \boldsymbol{0} & -(\boldsymbol{B}\boldsymbol{A}^{-1}\boldsymbol{B}^\top + \boldsymbol{C}) \end{pmatrix} \begin{pmatrix} \boldsymbol{I} & \boldsymbol{A}^{-1}\boldsymbol{B}^\top \\ \boldsymbol{0} & \boldsymbol{I} \end{pmatrix} \tag{A.15}$$

shows that $\boldsymbol{Q}$ is congruent to a block diagonal matrix. Neglecting the off-diagonal terms $\boldsymbol{B}\boldsymbol{A}^{-1}$ and $\boldsymbol{A}^{-1}\boldsymbol{B}^\top$ motivates the use of the symmetric and positive definite matrix

$$\boldsymbol{P} = \begin{pmatrix} \boldsymbol{A} & \boldsymbol{0} \\ \boldsymbol{0} & \boldsymbol{S} \end{pmatrix}, \qquad \text{with} \qquad \boldsymbol{S} = \boldsymbol{B}\boldsymbol{A}^{-1}\boldsymbol{B}^\top + \boldsymbol{C} \tag{A.16}$$

as preconditioner. However, since the Schur complement $\boldsymbol{S}$ involves $\boldsymbol{A}^{-1}$, systems of the form $\boldsymbol{P}\hat{\mathbf{z}} = \hat{\mathbf{r}}$ cannot be solved easily which makes $\boldsymbol{P}$ unsuitable as a preconditioner. Thus, we replace the Schur complement $\boldsymbol{S}$ by a lumped mass matrix weighted with the inverse viscosity μ^{-1}. For instance, in *Elman et al.* (2005) it is shown that in the case of constant viscosity the resulting diagonal matrix is spectrally equivalent to $\boldsymbol{S}$. For varying viscosity and interface Stokes problems, similar results are obtained in *Grinevich and Olshanskii* (2009). Note that, when lumped, the pressure stabilization matrix $\boldsymbol{C}$ drops out. This is due to the fact that at the element level, constants are in the null space of $\boldsymbol{C}$. The resulting diagonal matrix reflects the local element size as well as the local viscosity. This is essential for favorable scalability of the MINRES iterations as the problem grows, and is particularly important for adaptively refined meshes.

While a solve with the lumped mass matrix is trivial, the viscous block $\boldsymbol{A}$ is obtained from a discretization on highly heterogeneous meshes with large variations in the viscosity μ (up to six orders of magnitude). To approximately calculate $\boldsymbol{A}^{-1}\hat{\mathbf{r}}$ for a given residual $\hat{\mathbf{r}}$, we use one V-cycle of an algebraic multigrid (AMG) method (see, e.g., *Briggs et al.* (2000)).

Compared to geometric multigrid, AMG can have advantages due to its ability to account for variations in viscosity and adaptively refined meshes in the grid hierarchy. AMG requires a setup phase, in which a coarse grid hierarchy and corresponding restriction and interpolation operators are constructed. Parallel implementations of AMG require significant communication for this setup step. Generally, there is a trade-off between increased time/memory and the effectiveness of the coarse grid hierarchy. `Rhea` interfaces to two different parallel implementations of AMG, either to `BoomerAMG` from the `hypre` package (*The Hypre Team*, 2007; *De Sterck et al.*, 2006; *Falgout*, 2006), or to the smoothed aggregation implementation `ML` from the `Trilinos` project (*Gee et al.*, 2006). Both packages are available under open source licenses and allow the user to choose among various coarsening strategies, and to set parameters that influence the complexity of the coarse grid hierarchy and the interpolation and restriction operators.

A.4.4 Advection-Diffusion Solver

When the advection-diffusion equation (A.3) is discretized with Galerkin finite elements, the transport term can give rise to spurious oscillations of the numerical solution. Among various stabilization methods, the streamline upwind Petrov-Galerkin (SUPG) approach can be formulated by multiplying the residual of (A.3),

$$R(T) = \gamma - \frac{\partial T}{\partial t} - \mathbf{u} \cdot \nabla T + \nabla^2 T, \tag{A.17}$$

with the modified test function $W + \tau \mathbf{u} \cdot \nabla W$, where τ is a stabilization parameter:

$$\int_\Omega R(T) \left(W + \tau \mathbf{u} \cdot \nabla W \right) = 0. \tag{A.18}$$

The value of τ is derived from the element Peclet number, that is the relation between advection, diffusion, and element size (*Brooks and Hughes*, 1982). Integration by parts and invoking Dirichlet boundary conditions for the test space, $W|_{\partial\Omega} = 0$, yields bilinear forms

$$M(T, W) = \int_\Omega T(W + \tau \mathbf{u} \cdot \nabla W), \tag{A.19a}$$

$$G(T, W) = \int_\Omega (\mathbf{u} \cdot \nabla T) W, \tag{A.19b}$$

$$K(T, W) = \int_\Omega \nabla T \cdot (\mathbf{I} + \tau \mathbf{u} \otimes \mathbf{u}) \cdot \nabla W, \tag{A.19c}$$

which give rise to the nonsymmetric extended mass matrix $\tilde{\boldsymbol{M}}$ and advection matrix $\mathbf{G}$ and the extended stiffness matrix $\tilde{\boldsymbol{K}}$, respectively. Thus, the SUPG stabilization can be interpreted as the introduction of artificial diffusion along the streamlines of the velocity field, and the semi-discrete energy equation becomes

$$\mathbf{R}(\mathbf{T}) = \mathbf{g} - \tilde{\boldsymbol{M}} \frac{\partial \mathbf{T}}{\partial t} - \left(\mathbf{G} + \tilde{\boldsymbol{K}} \right) \mathbf{T} = \mathbf{0}, \tag{A.20}$$

where $\mathbf{g}$ is the discretization of the heat generation rate γ in (A.3). This system of ordinary differential equations is integrated in time by an iterative α-predictor-corrector method that operates on pairs of vectors $(\dot{\mathbf{T}}, \mathbf{T})$. For each time step k, the first iteration $i = 0$ is initialized by

$$\dot{\mathbf{T}}_k^0 = 0, \qquad \mathbf{T}_k^0 = \mathbf{T}_k + \Delta t (1 - \alpha) \dot{\mathbf{T}}_k. \tag{A.21}$$

The iterations proceed from i to $i+1$,

$$\boldsymbol{M}^* \Delta \dot{\mathbf{T}} = \mathbf{R}(\mathbf{T}_k^i), \tag{A.22a}$$

$$\dot{\mathbf{T}}_k^{i+1} = \dot{\mathbf{T}}_k^i + \Delta \dot{\mathbf{T}}, \tag{A.22b}$$

$$\mathbf{T}_k^{i+1} = \mathbf{T}_k^i + \alpha \Delta t \Delta \dot{\mathbf{T}}. \tag{A.22c}$$

We use three iterations per time step and $\alpha = \frac{1}{2}$, which provides second order accuracy in the (implicit) limit $i \to \infty$. The matrix $\boldsymbol{M}^*$ in (A.22a) can be understood as a preconditioner that may be approximate; we choose the diagonally lumped standard mass matrix which avoids an implicit solve. At the beginning of the simulation we obtain the time derivative $\dot{\mathbf{T}}$ by executing one zero-length time step with the initial value of $\mathbf{T}$. The spherical mantle convection code `CitcomS` (*Zhong et al.*, 2008) uses a similar time integration scheme. The method is described in detail in *Hughes* (2000); see also *Cottrell et al.* (2009).

The velocity field $\mathbf{u}$ enters the energy equation, and we update $\mathbf{u}$ by a Stokes solve between each two time steps, thus decoupling it from the time integration. This amounts to an explicit, first-order splitting with respect to the velocity. The is also means that the size of the time step is bounded by a CFL condition that is dominated by the advection limit in the problems considered here.

A.5 Adaptivity

Our goal is to simulate global mantle convection while taking into account the effects of faulted plate boundaries, trenches, and other tectonic features. These features require a spatial resolution of approximately 1 km (*Stadler et al.*, 2010). However, covering the volume of the mantle (which is of the order 10^{12} km^3) with an appropriately spaced grid would require

roughly a trillion mesh elements, which is still beyond the storage capacity of even large supercomputers. Furthermore, significant over-resolution would be created in areas such as the lower mantle, and any computation on this many elements would take an unacceptably long time.

We address this problem by adaptive mesh refinement (AMR), i.e., we cover the mantle with elements of different sizes depending on the local resolution requirements. Since the number of elements per volume scales with the third power of the resolution, large savings in element number are possible. In our computations we are able to achieve sub-km resolution of lithospheric features with less than 10^9 elements globally; this amounts to savings of three orders of magnitude.

Various approaches to AMR exist, differing in the type of the elements (tetrahedra, hexahedra, prisms), their organization in space (unstructured or hierarchical), and the refinement pattern (conforming or non-conforming); see, for example, *Flaherty et al*. (1997); *Berger and LeVeque* (1998). Compared to a uniform mesh approach, AMR adds significant topological and mathematical complexity. Implementing AMR efficiently on large parallel computers is challenging, due to the irregularity of element ordering schemes and communication patterns, and the requirement to distribute the computational work equally between all processors (parallel partitioning). Solving a stationary equation with a coarse-to-fine sweep of subsequently refined meshes, or evolving a dynamic problem with moving features in time, both call for frequent re-adaptation and re-partitioning of the mesh over the course of the simulation. Ideally, the time needed for all AMR components should remain small compared to solver time, so that the gains accrued for having fewer degrees of freedom are not offset by inefficiencies of the algorithms for adaptivity (*Luitjens et al.*, 2007; *Burstedde et al.*, 2010). For Rhea we have chosen a hierarchical non-conforming approach based on a forest of octrees that satisfies all

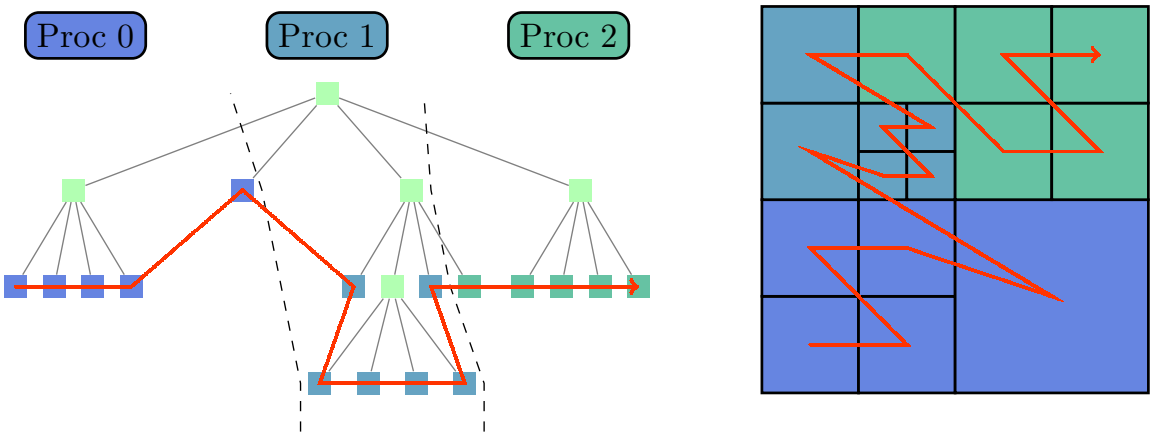

Figure A.1. A 2D cartoon of an octree on the left and the corresponding mesh on the right. The leaves of the octree, also called octants, correspond one-to-one to the elements of the mesh. A traversal of the leaves as indicated by the red curve (left) establishes a total ordering of the mesh elements in space (right), also called z-order due to its shape. Cutting this space filling curve into equal-sized pieces creates a parallel partition of the elements, in this example between the three processors 0, 1, and 2.

of the above requirements, described below.

A.5.1 Parallel Adaptive Meshes Based on a Forest of Octrees

The term octree refers to a logical tree structure where each node is either a leaf or has eight child nodes. The recursive tree structure can be identified with a subdivision of a cubic volume, obtained by splitting the volume into eight similar child elements and applying these splits recursively where higher resolution is desired. The leaves of the octree, also called octants, then correspond bijectively to the mesh elements; see Figure A.1.

After defining a fixed ordering sequence for any eight elements created in a split, traversing the hierarchical tree structure left-to-right establishes a total ordering of all elements. This so-called space-filling curve is depicted in Figure A.1. Due to the shape of the curve, this particular child sequence is also called z-order. We use the total ordering not only to establish the storage sequence of elements and associated degrees of freedom, but also to determine the partition of the mesh into processor domains that have equal numbers of elements, which

is essential for parallel load balancing. Additionally, the locality properties of the space filling curve allow near-optimal cache efficiency when looping over the elements in this order.

Efficient implementations of parallel adaptive octrees have been developed recently (*Tu et al.*, 2005; *Sundar et al.*, 2008). However, a single cube allows only a very restrictive set of computational domains. To lift this restriction, we decompose the domain into multiple octrees, conveniently called a forest of octrees, that are topologically equivalent to a hollow sphere. As an extension of the so-called cubed sphere approach we use 24 octrees, grouped into 6 caps of 2×2 octrees each, to achieve a roughly uniform aspect ratio (see Figure A.2). The space-filling curve is first connected through all 24 octrees and then split into pieces of equal length, which extends the z-order parallel partitioning scheme to the forest of octrees. An octree may be split between multiple processors, and a processor may store parts of more than one octree, depending on the number of processors and elements. In the `Rhea` code we interface to the scalable parallel forest-of-octree AMR implementation `p4est` (*Burstedde et al.*, 2011) that provides all mesh management operations.

We analytically map the forest of octrees into the spherical shell by a smooth transformation. A necessary condition for this map is the preservation of aspect ratio. Since an octree is a perfect cube, we demand that each octant is transformed into a mesh element of similar width and height. To reconcile this criterion with the fact that the domain is spherical, and the surface area of the core-mantle boundary is smaller than the outside surface area of the earth, we implement an exponential grading of the mesh with the radius. The mapping from the octree coordinates $\xi, \eta \in$ [-1, 1], $\zeta \in$ [0, 1] (which reflects the construction from a 2×2 octree) to the cap oriented in $+z$ direction is given by:

$$z = \frac{(R/R_{\mathrm{CMB}})^{\zeta-1}}{\sqrt{\tan^2(\pi\xi/4) + \tan^2(\pi\eta/4) + 1}},$$
$$x = z\tan(\pi\xi/4), \qquad y = z\tan(\pi\eta/4).$$

The 5 remaining caps are created by permuting x, y, and z and changing signs as appropriate. The grading in radial direction is derived as the solution of a one-dimensional ordinary differential equation that relates the octree-ζ-component to the non-dimensionalized radius. We abbreviate this transformation as $\boldsymbol{x} = \boldsymbol{x}(\boldsymbol{\xi})$. An illustration of the discretization of the mantle by this mapped forest of octrees is shown in Figure A.2.

A.5.2 Handling of Nonconforming Meshes

`Rhea` uses a continuous trilinear finite element discretization to represent all variables. A field such as the temperature is approximated by a linear combination of basis functions that in our case are trilinear, i.e., defined as tensor products of linear functions in the three space dimensions. Our meshes are nonconforming, which means that adjacent elements can have different sizes and the endpoints of neighboring faces or edges need not coincide; see Figure A.3. This results in nodes that are "hanging," i.e., that do not correspond to element basis functions on all adjacent elements. To enforce global continuity of finite element functions, the space of element-local basis functions must be restricted to a continuous subset. This can be done through algebraic constraints as outlined next.

Let us introduce local basis functions on each element e, denoted by $\psi_i^e(\boldsymbol{x}), i \in \{1, \dots 8\}$. We choose nodal basis functions that assume the value 1 at exactly one of the eight nodes $\boldsymbol{x}_j^e$ of the element, $\psi_i^e(\boldsymbol{x}_j^e) = \delta_{ij}$. These element-local basis functions are zero outside of

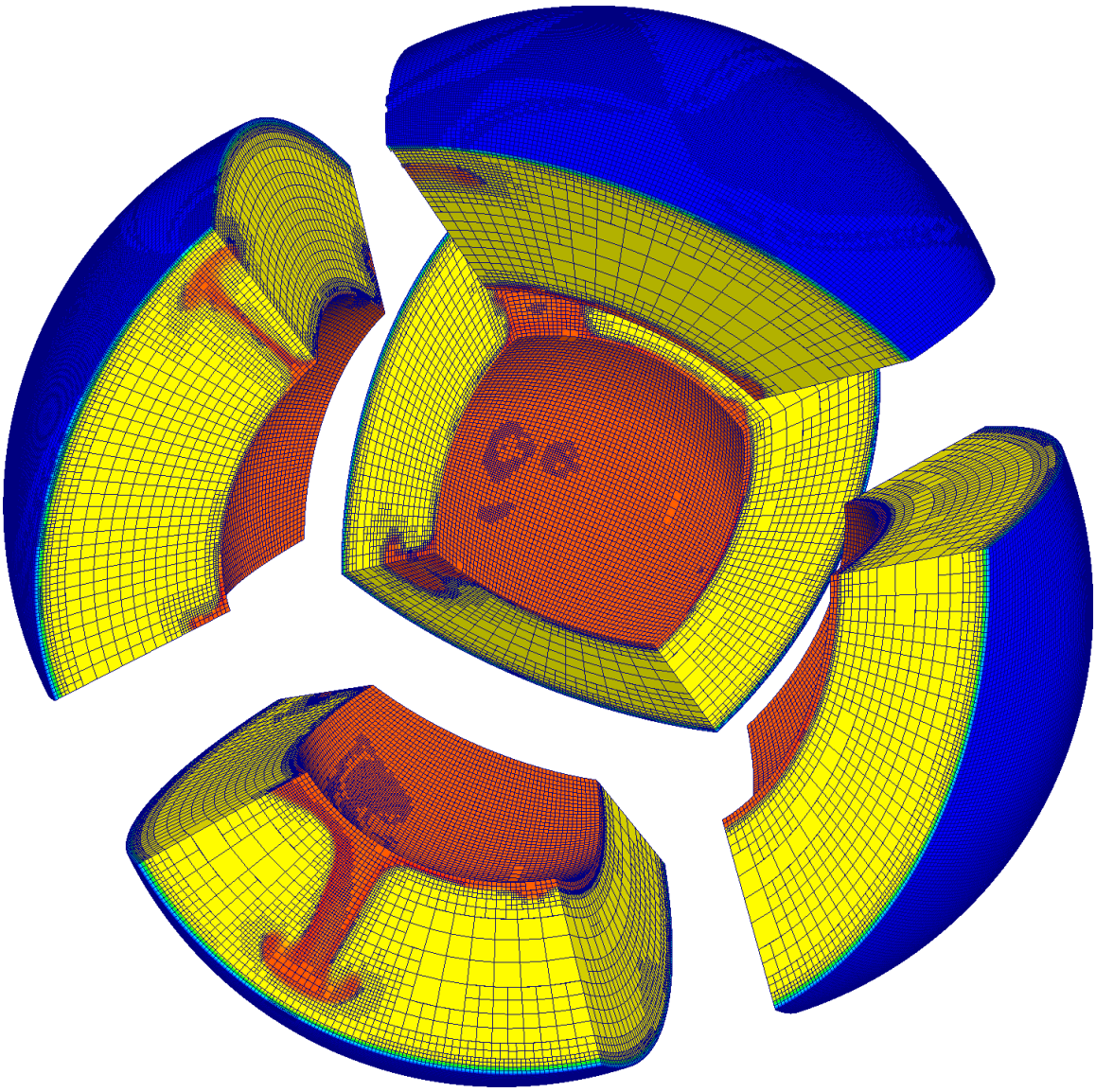

Figure A.2. Illustration of adaptive discretization of the mantle. Shown are five of the six caps of the cubed sphere. Each cap consists of 2×2 appropriately mapped octrees that are adaptively subdivided into octants (the mesh elements). The connectivity between the overall 24 octrees and the parallel distribution of elements is managed by the forest-of-octree library `p4est` (*Burstedde et al.*, 2011).

the element. A function that is trilinear on each element but possibly discontinuous between elements can be represented by element-local coefficients c_i^e as $f(\boldsymbol{x}) = \sum_{e,i} c_i^e \psi_i^e(\boldsymbol{x})$.

To fully specify the element-local basis functions $\psi_i^e(\boldsymbol{x})$ we take into account both the transformation from the octree coordinates $\boldsymbol{\xi} = (\xi, \eta, \zeta)^\top$ into physical coordinates $\boldsymbol{x}(\boldsymbol{\xi})$ and the scaled shift $\boldsymbol{\xi} = \boldsymbol{\xi}_e(\boldsymbol{r})$ from the reference element $\boldsymbol{r} = (r, s, t)^\top \in [-1, 1]^3$ into the octant that corresponds to element e, covering a cubic subvolume V_e of octree coordinate space. Combined with a tensor-product ansatz for three space dimensions this yields

$$\psi_i^e(\boldsymbol{x}) = \psi_i^e(\boldsymbol{x}(\boldsymbol{\xi}_e(\boldsymbol{r}))) = \ell_{1,i}(r)\ell_{2,i}(s)\ell_{3,i}(t) = \left(\prod\nolimits_d \ell_{d,i}\right)(\boldsymbol{r}).$$

The linear basis functions $\ell_{d,i}$ are 1 at one end of the reference interval and zero on the other, based on the coordinate direction d and the corner number i.

Adaptive refinement and coarsening produces non-conforming meshes where nodes of one element are not necessarily nodes of a neighboring element, but may instead be hanging (see Figure A.3). Continuity of the trilinear representation can be enforced by identifying only the non-hanging nodes with global independent degrees of freedom g_n, where $n \in \{1, \ldots, N\}$ and N is the number of independent nodes, and generating the element-local coefficients through an interpolation matrix S,

$$c_i^e = \sum_n S_{in}^e g_n.$$

The matrix S is sparse and thus never assembled or stored; instead the submatrix $\boldsymbol{S}_e = (S_{in}^e) \in \mathbb{R}^{8\times N}$ is applied for an element e. Through the identification

$$f(\boldsymbol{x}) = \sum_{e,i} c_i^e \psi_i^e(\boldsymbol{x}) = \sum_{e,i} \sum_n S_{in}^e g_n \psi_i^e(\boldsymbol{x}) = \sum_n g_n \phi_n(\boldsymbol{x})$$

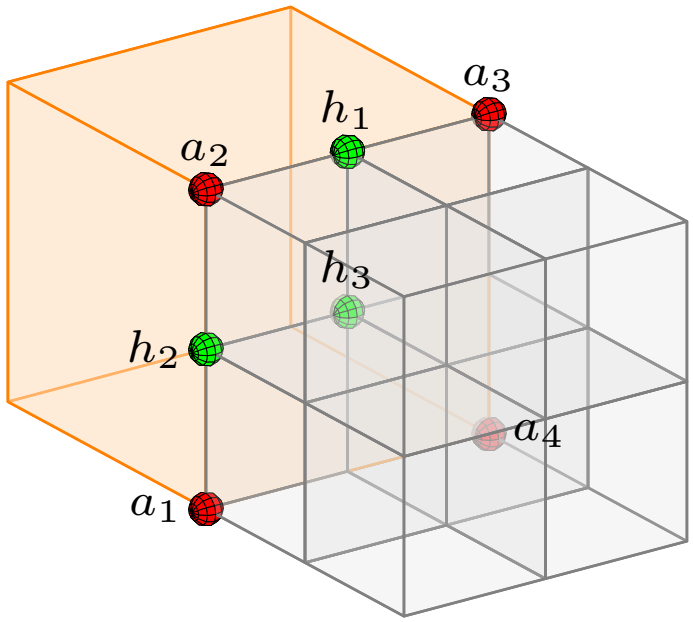

Figure A.3. Illustration of a hanging face in a nonconforming adaptive discretization. The values of a variable field at the hanging nodes h_1, h_2, h_3 are computed from the values at a_1, a_2, a_3, a_4 through interpolation. For instance, for the edge-hanging node h_1 the value is given by the mean of the values at a_2 and a_3; similarly, the value at the face-hanging node h_3 is given by the mean of a_1, a_2, a_3, a_4.

we define global basis functions $\phi_n = \sum_{e,i} S^e_{in} \psi^e_i$ that are locally supported and continuous by construction.

For parallel computation we distribute the global degrees of freedom among the processors. Hanging nodes are always understood as processor-local and their values are interpolated when needed from associated independent nodes (Figure A.3). We assign ownership of an independent node to the lowest-numbered processor whose elements touch it. Given local copies of one layer of off-processor elements (so-called ghost elements) each processor can determine the hanging status and processor ownership of all nodes touching any of its elements without further communication. To determine a globally unique numbering of all degrees of freedom, each processor counts its owned independent nodes and shares this number with all other processors. Every processor then offsets its owned node indices by the number of independent nodes owned by all lower-numbered processors.

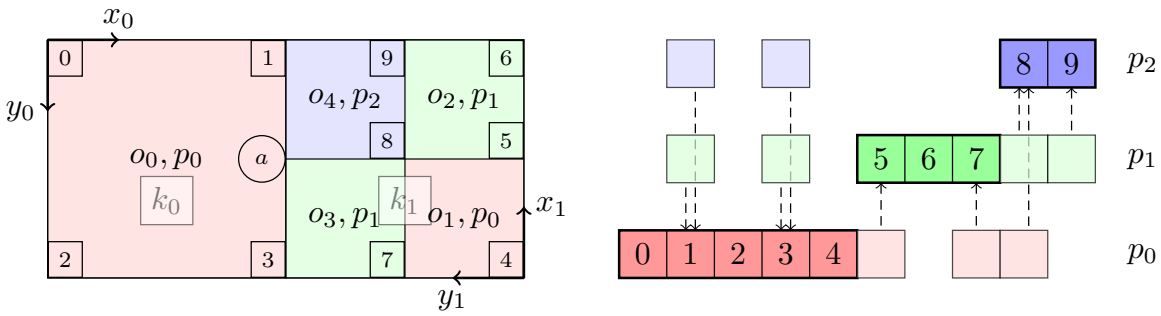

Figure A.4. Globally unique node numbering and parallel sharer lists on an example mesh consisting of two octrees partitioned between three processors. On each processor the owned nodes are numbered in z-order with respect to the octree coordinate systems (see also Figure A.1). Sharing processors arise due to independent nodes on processor boundaries and due to the hanging node a that depends on independent node values for interpolation (numbers 1 and 3 in this case).

The values of an independent node may be needed on other processors than its owner, either through an independent node on the processor boundary or through referral by an off-processor hanging node that depends on its value for interpolation. Thus, for each independent node we maintain a list of sharing processors. Most independent nodes are away from inter-processor boundaries due to the surface-to-volume ratio of the parallel partition; these have no sharers. Those on a processor boundary usually have a small and bounded number of sharers due to the locality properties of the space filling curve.

The authoritative value for a degree of freedom is stored on its owner processor; we use the sharer lists to send its value to other processors, and to receive updates when necessary. The algorithms for creation of the ghost layer and the trilinear node numbering for a forest-of-octree mesh are detailed in *Burstedde et al.* (2011). Figure A.4 illustrates the global node numbering and sharer lists.

While all finite element variables are stored as global degrees of freedom it is more convenient to apply discretized operators, such as mass or stiffness matrices, using the element-local formulation. With the definitions introduced above we decompose, for example, the mass ma-

trix $\boldsymbol{M} = (M_{mn}) \in \mathbb{R}^{N \times N}$ as follows,

$$M_{mn} = \int_\Omega \phi_n(\boldsymbol{x}) \phi_m(\boldsymbol{x}) \mathrm{d}\boldsymbol{x} = \sum_{e,i,j} \int_{\Omega_e} S^e_{in} \psi^e_i(\boldsymbol{x}) S^e_{jm} \psi^e_j(\boldsymbol{x}) \mathrm{d}\boldsymbol{x}$$

or, equivalently in matrix notation,

$$\boldsymbol{M} = \sum_e \boldsymbol{S}_e^\top \boldsymbol{M}_e \boldsymbol{S}_e \quad \text{with} \quad M^e_{ji} = \int_{\Omega_e} \psi^e_i(\boldsymbol{x}) \psi^e_j(\boldsymbol{x}) \mathrm{d}\boldsymbol{x}. \tag{A.23}$$

Here, Ω is the whole domain and Ω_e the part occupied by element e. The element-local mass matrix $\boldsymbol{M}_e = (M^e_{ji}) \in \mathbb{R}^{8 \times 8}$ is then evaluated using the transformation theorem,

$$M^e_{ji} = \int_{[-1,1]^3} V_e \left| \frac{\partial \boldsymbol{x}}{\partial \boldsymbol{\xi}} \right|_{\boldsymbol{\xi}_e(\boldsymbol{r})} \left(\prod\nolimits_d \ell_{d,i} \right)(\boldsymbol{r}) \left(\prod\nolimits_d \ell_{d,j} \right)(\boldsymbol{r}) \mathrm{d}\boldsymbol{r},$$

where V_e is the volume fraction of the octant within its octree. In `Rhea` we approximate the volume integral by the tensor product of three third-order Gauss integration rules, one for each coordinate direction, thus using eight integration points on the reference element.

A matrix-vector product is computed in parallel by looping over all processor-local elements and applying (A.23), or rather the analogous expression for any of the specific matrices introduced in Section A.4, using shared degrees of freedom when necessary. Shared entries of the result are sent to all sharing processors, and contributions to local shared or owned degrees of freedom are received and added. This process yields identical results for independent nodes on all of their respective sharers.

A.5.3 Criteria for Mesh Adaption

There are various scenarios in which adaptively refined meshes are beneficial. Adapted meshes may be needed, for instance, to resolve boundary layers, sharp temperature or viscosity gradients, and narrow weak zones near plate boundaries. In simulations for which it is known a priori where the largest mesh resolution is necessary, an appropriately refined mesh can be chosen as part of the preprocessing. Often, such prior knowledge is not available and an adequate mesh adaptation depends on properties of the solution. This so-called solution adaptivity usually requires solving the problem on a sequence of meshes. After each solution, an error indicator is used to help decide where the mesh should be refined or coarsened.

As is the case with solution adaptivity for stationary problems, time-dependent simulations also require that the mesh is adapted while the simulation is running. We denote this capability "dynamic AMR," which implies that the mesh needs to be repartitioned after each adaptation and all finite element fields must be transferred from the old to the new mesh. This is a particularly challenging problem arising with parallel computation. Example mantle convection problems that require dynamic AMR are those featuring rising plumes or a rheology law that produces localized features, as, for instance, rheologies that accommodate yielding under high strain rates. To keep the number of elements small in dynamically refined AMR problems, meshes also have to be coarsened wherever high resolution is no longer necessary. The algorithmic framework for dynamic adaptivity used in `Rhea` is described in *Burstedde et al.* (2008a).

Accurate element-based error indicators are essential for effective solution adaptivity. Various choices for such error indicators are summarized next.

Physics-based error indicators. Often, physical intuition can be used to devise an indicator for adapting the mesh to the problem: simple examples are element-wise temperature gradients for the energy equation and viscosity gradients or numerical velocity divergence for the Stokes equation.

Residual-based error indicators. For some problems error indicators are available that can be proven to provide bounds for the actual error. These indicators (also called error estimators) involve element equation residuals and jumps of the solution derivatives across element faces, or they require a reconstruction of the solution over a patch consisting of several elements (*Ainsworth and Oden*, 2000).

Goal-oriented error indicators. Often, one is not interested in minimizing the global discretization error, but in obtaining high accuracy in a certain quantity of interest, for instance the solution in a part of the domain or its mean. Goal-oriented error indicators (*Becker and Rannacher*, 2001; *Ainsworth and Oden*, 2000; *Oden and Prudhomme*, 2001) lead to meshes that target maximal accuracy in the quantity of interest. However, they require the solution of an adjoint problem, which makes them comparably costly (*Burstedde et al.*, 2009b).

Having an error indicator at hand, it remains to decide which elements to refine and coarsen. Several strategies can be used, for instance to coarsen/refine elements with an error indicator under/above a certain threshold. Alternatively, one can coarsen and refine a certain percentage of elements, since it is often desirable to control the size of the simulation. This approach relies on choosing appropriate refinement/coarsening thresholds to obtain a target number of elements. In a parallel simulation environment, these thresholds can be determined by the iterative bisection algorithm `MarkElements` described in *Burstedde et al.* (2008b). For

most time-dependent simulations we use the latter strategy to keep the number of elements constant throughout the simulation.

A.5.4 Mesh Adaptation for Time-Dependent Problems

Simulation of the energy transport of mantle convection (A.3) often reveals the creation and disappearance of localized features, and a motion of plumes and other structures through space. Thus, the mesh needs to be adapted dynamically to resolve physics that evolve with time. While adaptation after each time step is technically possible, in practice it is sufficient to only adapt the mesh after a time interval corresponding to a fixed number of time steps (e.g., 10–50 steps). To obtain a properly adapted mesh for such a time interval, we determine the maximum in time of an error indicator separately for each element. Implementing this strategy naively, however, would allow features that move from a finely resolved into a coarsely resolved area during the same interval, resulting in a loss of information. This risk can be eliminated by a multi-pass algorithm, as described in *Sun and Wheeler* (2004). Here, one or more passes for estimation can be executed to gather the error information, which is then used to create a new mesh and run the simulation pass starting from a checkpoint that was saved previously. Our adaptation of this process is illustrated in Figure A.5 and has been described in *Burstedde et al.* (2008b) in more detail.

The numerical result of the estimation pass is discarded after mesh adaptation and can thus be approximate. For the simulation of mantle convection, where solving the Stokes systems consumes the majority of computation time, we hold the flow solution constant for the error estimation pass to avoid solving the Stokes equation at each estimation time step.

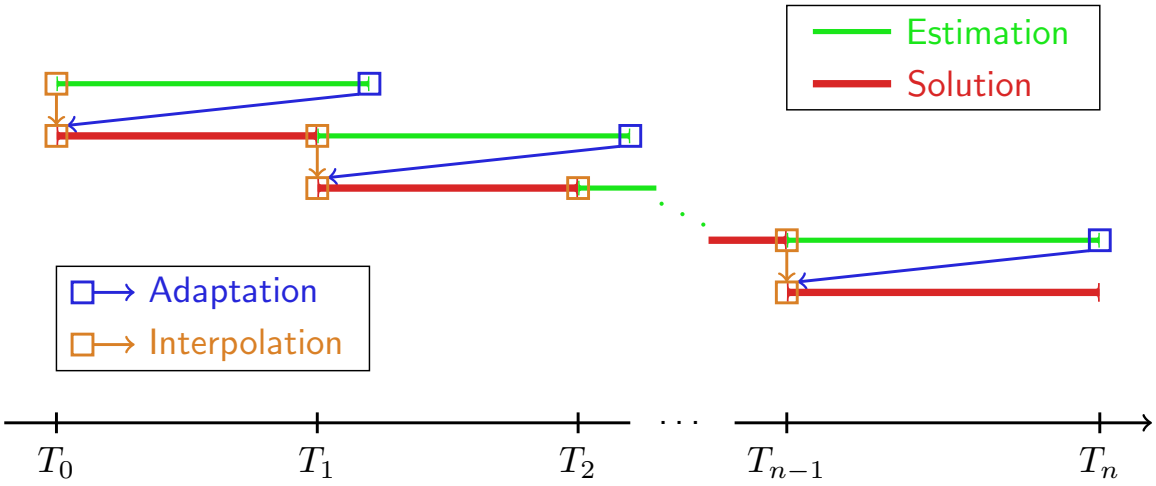

Figure A.5. Interval-based adaptation over time. The estimation pass (green) is used to compute the average error information throughout one interval and adapt the mesh accordingly at the end (blue arrows). The initial condition has been saved and is transferred to the new mesh (orange arrows). The simulation pass (red) then executes on a mesh that is well adapted for this interval. It can be chosen shorter than the estimation pass in case the time integration does not accumulate sufficient error information towards the end of an interval. The cost of multiple passes through the same interval can be reduced by using a less expensive numerical solution method for estimation.

A.6 Tests and Benchmarks

The purpose of this section is twofold: First, we provide evidence for the correctness of the `Rhea` code by comparing numerical against analytical solutions and studying convergence rates. Second, we analyze the potential of adaptively refined meshes for typical mantle convection benchmarks and discuss for which scenarios adaptive mesh capabilities are most beneficial.

A.6.1 Analytical Solutions for the Stokes Equations

Analytical solutions can be employed effectively to demonstrate the correctness of the implementation and to verify convergence rates for finite element discretizations of partial differential equations. However, it is generally not possible to construct an analytical solution for a given right-hand-side $\mathbf{f}$. What is possible, in contrast, is to postulate velocity and pressure

fields and to insert them into the system of equations to derive an appropriate $\mathbf{f}$ that is used as forcing for the simulation. The postulated and computed velocity and pressure can then be compared. This approach is often called the method of manufactured solutions. It can reveal errors in the implementation and deliver precise convergence rates of numerical approximations. In this section we present two manufactured solutions, namely a polynomial and a trigonometric formulation.

A.6.1.1 Polynomial Solution Benchmark

We begin by postulating a simple polynomial solution for the Stokes equations (*Dohrmann and Bochev*, 2004),

$$\mathbf{u} = \begin{pmatrix} x + x^2 + xy + x^3 y \\ y + xy + y^2 + x^2 y^2 \\ -2z - 3xz - 3yz - 5x^2 yz \end{pmatrix}, \tag{A.24a}$$

$$p = xyz + x^3 y^3 z - 5/32, \tag{A.24b}$$

which is divergence free. Inserting this solution into the momentum equation with a given viscosity μ, we obtain the right-hand-side forcing:

$$\mathbf{f} = -\nabla p + \mu \begin{pmatrix} -2 - 6xy \\ -2 - 2x^2 - 2y^2 \\ 10yz \end{pmatrix} - \mu_x \begin{pmatrix} 2 + 4x + 2y + 6xy \\ x + x^3 + y + 2xy^2 \\ -3z - 10xyz \end{pmatrix} - \mu_y \begin{pmatrix} x + x^3 + y + 2xy^2 \\ 2 + 2x + 4y + 4x^2y \\ -3z - 5x^2z \end{pmatrix} - \mu_z \begin{pmatrix} -3z - 10xyz \\ -3z - 5x^2z \\ -4 - 6x - 6y - 10x^2y \end{pmatrix}. \quad \text{(A.25)}$$

We also impose exact velocity boundary conditions derived from (A.24). Then we solve the Stokes equations with `Rhea` and compute the L^2-norm of the difference between numerical and exact solutions $(\mathbf{u}_h, p_h)$ and $(\mathbf{u}, p)$, respectively,

$$||\mathbf{u} - \mathbf{u}_h||_{L^2} := \left(\int_\Omega (\mathbf{u}_h - \mathbf{u})^2 \, dx \right)^{1/2}, \quad \text{(A.26a)}$$

$$||p^\star - p_h||_{L^2} := \left(\int_\Omega (p_h - p)^2 \, dx \right)^{1/2}. \quad \text{(A.26b)}$$

In Table A.1 we summarize the convergence results for constant viscosity $\eta \equiv 1$ on a $45^\circ \times 45^\circ$ portion of the spherical shell as well as the global mantle geometry, for which the radius has been scaled to 1. Additionally we show the number of MINRES iterations to achieve a drop in the residual by a factor of 10^8. Analogous results for a spatially smoothly varying viscosity

$$\mu = \exp(1 - 4(x(1-x) + y(1-y) + z(1-z))) \quad \text{(A.27)}$$

are included in Table A.2.

As expected from the theory (*Dohrmann and Bochev*, 2004), with each uniform mesh

mesh	$\|\|u^\star - u_h\|\|_{L^2}$	$\|\|p^\star - p_h\|\|_{L^2}$	#iter
8^3	8.08e-4	3.85e-2	47
16^3	2.25e-4	1.15e-2	47
32^3	5.84e-5	3.43e-3	54
64^3	1.46e-5	1.03e-3	54
24×4^3	1.53e-2	2.66e-1	75
24×8^3	4.40e-3	8.95e-2	50
24×16^3	1.16e-3	2.98e-2	57
24×32^3	2.94e-4	1.01e-2	67

Table A.1. Polynomial solution example: Error between exact and numerical solution for constant viscosity $\mu \equiv 1$ for a $45°\times 45°$ portion of the spherical shell (upper part) and the full mantle geometry (lower part). The number of MINRES iterations is reported in the rightmost column.

mesh	$\|\|u^\star - u_h\|\|_{L^2}$	$\|\|p^\star - p_h\|\|_{L^2}$	#iter
16^3	2.75e-4	1.03e-1	51
32^3	6.94e-5	3.80e-2	58
64^3	1.72e-5	1.28e-2	55
24×16^3	8.56e-3	1.70e+3	179
24×32^3	2.19e-3	4.55e+2	122

Table A.2. Polynomial solution example: Error between exact and numerical solution for variable viscosity given in (A.27). For the $45°\times 45°$ portion of the spherical shell (top), the viscosity varies by a factor of about 300, and for the global mantle geometry (bottom) by about 10^6. The MINRES iteration is terminated if a relative drop in the residual of, respectively, 10^8 or 10^9 is achieved. The difference in the number of iterations can be explained by the fact that the coarser mesh cannot fully resolve the viscosity variations.

refinement (that halves the mesh size) the velocity error decreases by a factor of 4, and thus the convergence rate is of order 2. For the pressure error, finite element theory only predicts a decrease of linear order for a uniform refinement. However, our numerical tests yield a better value of approximately 1.6, which is also observed in *Dohrmann and Bochev* (2004). Note that the number of iterations required to solve the problems is almost constant across different refinement levels. Such a mesh-independent convergence rate of solvers is necessary to obtain optimal scalability when problems become very large, and constitutes the main motivation to employ multigrid-type preconditioners.

A.6.1.2 Diverging Flow Stokes Example

We now use an example that models diverging flow that has similarities to the mantle flow found at a mid-ocean ridge. The viscosity μ and the forcing $\mathbf{f}(r,\theta,\varphi) = (f_r, f_\theta, f_\varphi)$ are, in spherical coordinates, given as follows:

$$\mu = r^2, \tag{A.28a}$$

$$\begin{aligned} f_r \;&= \frac{8(1+4r^5)(1-\tanh(\frac{\varphi}{\phi_0})^2)}{5\varphi_0 r^2} \\ &\quad - \frac{2(1-r^5)(1-\tanh(\frac{\varphi}{\phi_0})^2)(3\tanh(\frac{\varphi}{\phi_0})^2-1)}{5\varphi_0^3 r^2\sin(\theta)^2} \\ &\quad + 2r\sin(\theta)\sin(3\varphi) - \frac{\theta^3}{r^2}, \end{aligned} \tag{A.28b}$$

$$f_\theta = \frac{2r^3\cos(\theta)(1-\tanh(\frac{\varphi}{\phi_0})^2)}{\varphi_0\sin(\theta)} + r\cos(\theta)\sin(3\varphi) + 3\frac{\theta^2}{r^2}, \tag{A.28c}$$

$$\begin{aligned} f_\varphi \;&= \frac{2(4+r^5)(1-\tanh(\frac{\varphi}{\phi_0})^2)\tanh(\frac{\varphi}{\phi_0})}{5\varphi_0^2 r^2\sin(\theta)} \\ &\quad - 14r^3\sin(\theta)\tanh(\frac{\varphi}{\phi_0}) + 3r\cos(3\varphi). \end{aligned} \tag{A.28d}$$

Above, the parameter $\varphi_0 > 0$ controls the smoothness of the ridge. The smaller φ_0, the faster and more localized is the radial flow under the ridge; see Figure A.6. It can be verified that the solution $(\mathbf{u}, p) = (u_r, u_\theta, u_\varphi, p)$ to the ridge Stokes flow problem is given by

$$u_r = \frac{(1-r^5)(1-\tanh(\frac{\varphi}{\phi_0})^2)}{5\varphi_0 r^2}, \tag{A.29a}$$

$$u_\theta = 0, \tag{A.29b}$$

$$u_\varphi = r^3\sin(\theta)\tanh(\frac{\varphi}{\phi_0}), \tag{A.29c}$$

$$p = r^2\sin(\theta)\sin(3\varphi) + \frac{\theta^3}{r^2}. \tag{A.29d}$$

mesh	$\frac{\|\|u^\star - u_h\|\|_{L^2}}{\|\Omega\|}$	$\frac{\|\|p^\star - p_h\|\|_{L^2}}{\|\Omega\|}$	#iter
8^3	2.75e-2	6.18e-1	42
16^3	7.42e-3	1.92e-1	42
32^3	1.91e-3	5.91e-2	46
64^3	4.80e-4	1.86e-2	42
16^3	3.02e-1	8.74e0	38
32^3	8.20e-2	1.00e0	43
64^3	2.35e-2	3.22e-1	40
128^3	6.08e-3	8.73e-2	42
256^3	1.54e-3	2.39e-2	44
512^3	3.85e-4*	5.66e-3*	49

Table A.3. Ridge example: L^2-errors between exact and numerical solution for parameters $\varphi_0 = 0.5$ (upper table) and $\varphi_0 = 0.05$ (lower table). The last column shows the number of iterations to obtain a drop in residual by 10^{-7} (the errors marked by * are obtained after a drop in residual by 10^{-9}).

To study the accuracy of our numerical method, we set the velocity on the boundary to the exact solution and then solve the Stokes problem for the forcing given above. Again, we report the L^2-norm of the difference between numerical and exact solution $(\mathbf{u}_h, p_h)$ and $(\mathbf{u}, p)$, respectively; see Table A.3. Note that for the same mesh, for large φ_0 the numerical solution is a better approximation of the exact solution. This can be explained by the fact that for small φ_0 the solution becomes less smooth, which makes the numerical solution of the problem harder.

Furthermore, note that the number of iterations remains stable as the mesh is refined, enabling the efficient solution of large-scale problems.

A.6.2 Benchmarks for Stokes Solver

We now use a common Stokes benchmark problem (see, e.g., *Zhong et al.* (2008); *Choblet et al.* (2007)) to verify the flow solution of the Stokes solver, as well as the computation of surface and CMB topography. The problem uses constant viscosity, the Rayleigh number is unity, and the temperature is specified as a delta function at a radius r_0 in the radial direction

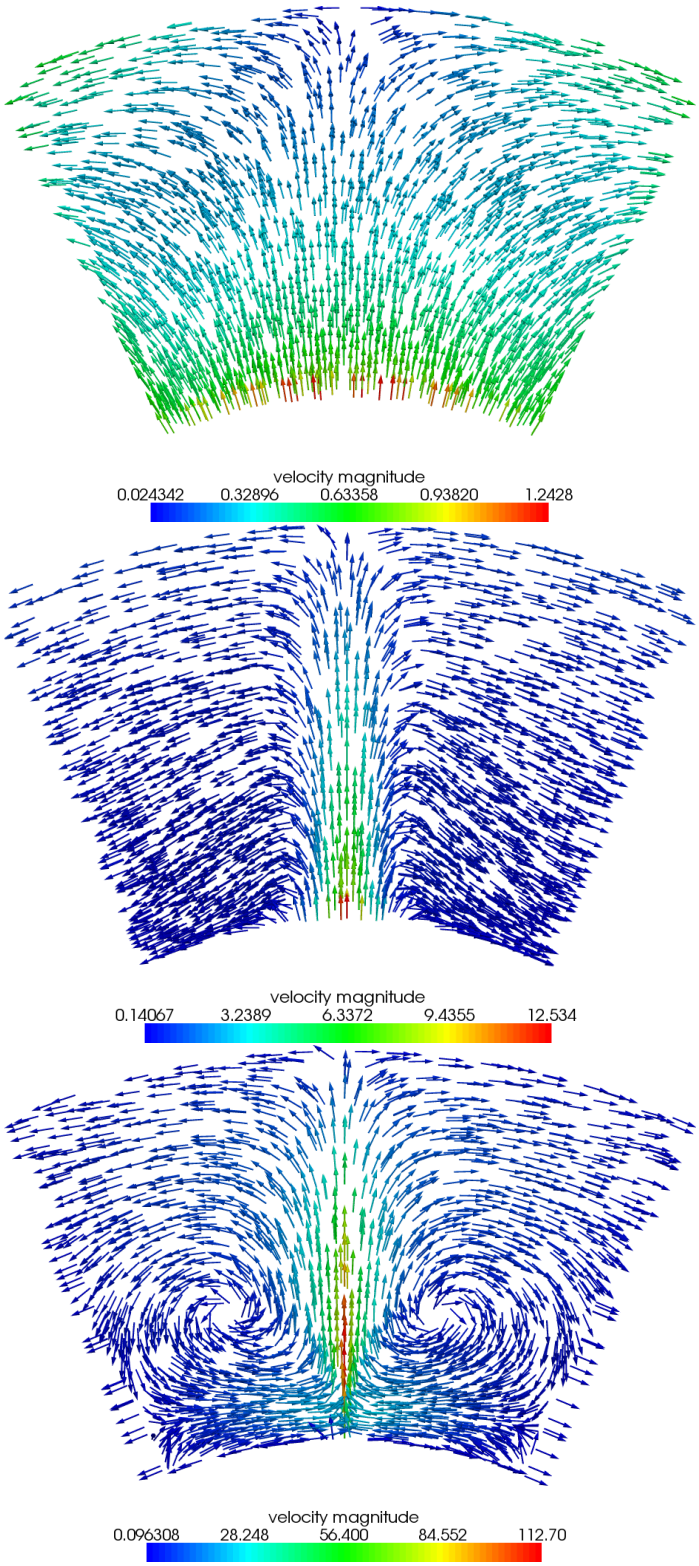

Figure A.6. Slice ($\theta = 0$) through flow field for exact ridge example solution for parameters $\varphi_0 = 0.5$ (top), $\varphi_0 = 0.05$ (middle), and $\varphi_0 = 0.01$ (bottom).

#cores	#elem/ core	#elem	#iter	setup time [s]	matvecs time [s]	V-cycle time [s]
120	5,800	700K	24	1.39	2.75	2.88
960	4,920	4.72M	22	2.30	3.94	2.89
7,680	4,805	36.9M	23	4.07	3.99	5.72
61,440	5,145	316M	21	34.2	4.60	9.03
122,880	5,135	631M	26	112.48	6.29	8.39

Table A.4. Weak scaling with approximately 5,000 elements per core for the mid-ocean ridge Stokes example, obtained on the Jaguar supercomputer. The mesh contains elements of three different sizes determined by a strain rate error indicator and the viscosity varies over one order of magnitude. Reported are the number of MINRES iterations to decrease the residual by a factor of 10^4, the time for the AMG setup (using `ML` from `Trilinos`), the overall time for matrix-vector and inner products, and for the V-cycles in MINRES. `ML` employs the recursive coordinate bisection (RCB) repartitioning algorithm from `ZOLTAN` to improve the parallel efficiency of the multigrid hierarchy.

and a spherical harmonic function Y_l^m of degree l and order m in the tangential directions, i.e.,

$$T(r, \varphi, \theta) = \delta(r - r_0) Y_l^m(\varphi, \theta). \tag{A.30}$$

The δ-function in the radial direction is approximated by a triangle with unit area:

$$\delta(r - r_0) = \begin{cases} \dfrac{n_{er}}{r_t - r_b} & \text{if } r = r_0, \\ 0 & \text{otherwise,} \end{cases} \tag{A.31}$$

where n_{er} is the number of elements in the radial direction in a uniform mesh. The spherical harmonic function is described by

$$Y_l^m(\varphi, \theta) = \cos(m\varphi) p_{lm}(\theta). \tag{A.32}$$

The normalized associated Legendre polynomial p_{lm} is related to the associated Legendre polynomial P_{lm} by:

$$p_{lm}(\theta) = \sqrt{\frac{(2l+1)(l-m)!}{2\pi(1+\delta_{m0})(l+m)!}}\, P_{lm}(\theta). \tag{A.33}$$

The usual free-slip boundary conditions are used. Due to properties of the spherical harmonics functions, this setting allows the computation of the Stokes flow by solving numerically an ordinary differential equation for the coefficient of the spherical harmonic; see *Hager and Richards* (1989). This semi-analytical solution is used to compare with the finite element-based solution obtained in `Rhea`.

As in *Hager and Richards* (1989); *Zhong et al*. (2008); *Choblet et al*. (2007), we report the responses of flow and topography at the top surface and the CMB when changing the radius r_0, at which the force is imposed; see Figure A.7. The mesh size is varied from 2^3 to 2^6 elements. We perform a detailed error analysis for the various resolutions (Figure A.8). The errors in response functions with respect to the semi-analytical solution decrease quadratically with increasing resolution, as expected. The error increases with increasing spherical harmonic degree as the complexity of the forcing is made larger. Additionally, the error decreases with increasing forcing depth. Due to the spherical geometry of the domain, elements have smaller dimensions at larger depth and therefore errors with respect to the semi-analytical solution are smaller. These results are in agreement with those of *Zhong et al*. (2008).

We use this benchmark problem to assess parallel scalability as we simultaneously increase the problem size and the number of processing cores. A breakdown of different components of `Rhea` by runtime is presented in Table A.4. We observe that the number of iterations remains essentially constant over a three-orders-of-magnitude increase in problem size and number of processor cores. Thus we observe algorithmic scalability out to 123,000 cores and 631M elements (which corresponds to roughly 2.5B degrees of freedom). Parallel scalability can be assessed by observing the growth in CPU time of the dominant components of the Stokes solver: AMG setup at the beginning of each Stokes solve, the matrix-vector product time for each Krylov iteration, and the V-cycle time associated with the application of the AMG

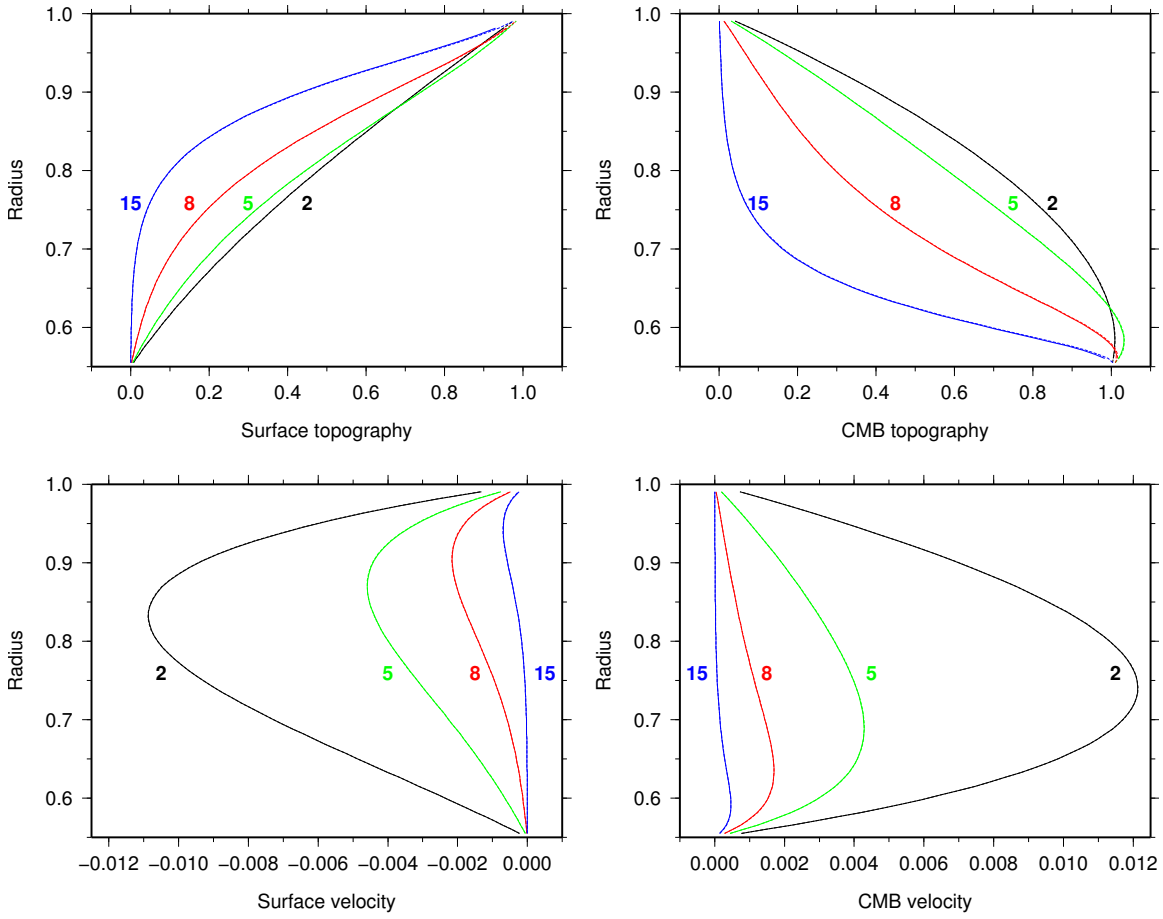

Figure A.7. Response functions for surface topography, CMB topography, velocity at the surface, and velocity at the CMB, for spherical harmonic degrees 2, 5, 8, and 15 in a sphere with uniform viscosity. The solid lines show the `Rhea` solution, the dashed lines the semi-analytical solution.

preconditioner at each Krylov iteration. As can be seen, the latter two times remain relatively stable over the thousandfold increase in problem size and number of cores (for perfect weak scaling, they would not grow at all). However, the AMG setup time experiences large growth above 10^4 processor cores. This is understandable, given the large communication induced in the AMG setup, and is rarely a problem in practice, since even at 123,000 cores, the AMG setup time is still dominated by the total time taken (across Krylov iterations) in matrix-vector products and V-cycle applications; moreover, the AMG setup can often be reused for several Stokes solves.

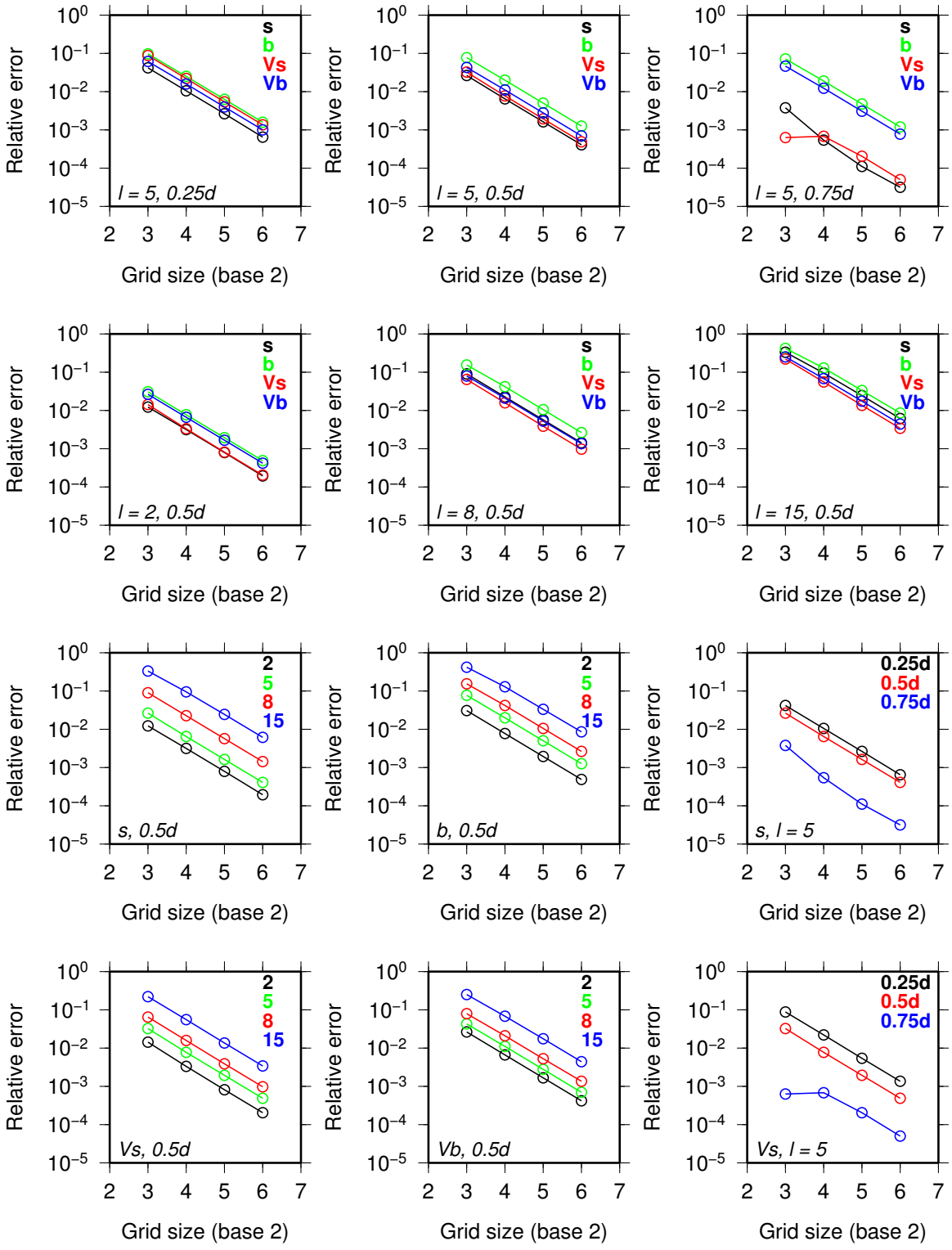

Figure A.8. Errors in response functions with respect to the semi-analytical solution for surface topography (s), CMB topography (b), velocity at the surface (V_s), and velocity at the CMB (V_b), for spherical harmonic degrees 2, 5, 8, and 15 in a sphere with uniform viscosity. Three forcing depths are shown left to right, namely $0.25d$, $0.5d$, and $0.75d$.

A.6.3 Time-Dependent Benchmark

The time-dependent solver in `Rhea` is benchmarked using a spherical harmonic temperature perturbation, superimposed onto a conductive profile in a shell. The temperature field is defined as follows:

$$T(r,\theta,\varphi) \quad = \quad \frac{r_b(r-r_t)}{r(r_b-r_t)} \; + \; \big(\epsilon_c \cos(m\varphi) \; + \; \epsilon_s \sin(m\theta)\big) p_{lm}(\theta) \sin\frac{\pi(r-r_b)}{(r_t-r_b)}, \quad \text{(A.34)}$$

where p_{lm} is given by (A.33). The parameters ϵ_c and ϵ_s are set to 0.01, and the degree l and order m are 3 and 2, respectively. The viscosity is given by:

$$\mu = \exp[E(0.5-T)], \quad \text{(A.35)}$$

where the viscosity variation within the model is determined by the activation energy E. Cases with $\Delta\mu = 1$ (isoviscous) and $\Delta\mu = 20$ are run. These cases have also been reported by *Bercovici et al.* (1989) and *Zhong et al.* (2000) for $\Delta\mu = 1$, and by *Ratcliff et al.* (1996); *Yoshida and Kageyama* (2004); *Stemmer et al.* (1996) for $\Delta\mu = 1$, 20. *Zhong et al.* (2008) showed results for a wide range of viscosities from $\Delta\mu = 1$ to 10^7. We use a Rayleigh number of 7.6818×10^4. The mesh is uniform at level 5, corresponding to 32 elements in the radial direction, which is comparable to that of *Zhong et al.* (2008).

The resulting temperature field in steady state has tetrahedral symmetry for the viscosity ranges tested here. The steady-state temperature field shows four well-defined plume-like upwellings, and a set of interconnected downwelling sheets (Figure A.9). The time series of average temperature, average root mean square velocity, and Nusselt numbers at the top and bottom of the mantle reproduce results described by, e.g., *Zhong et al.* (2008) (Figure A.10).

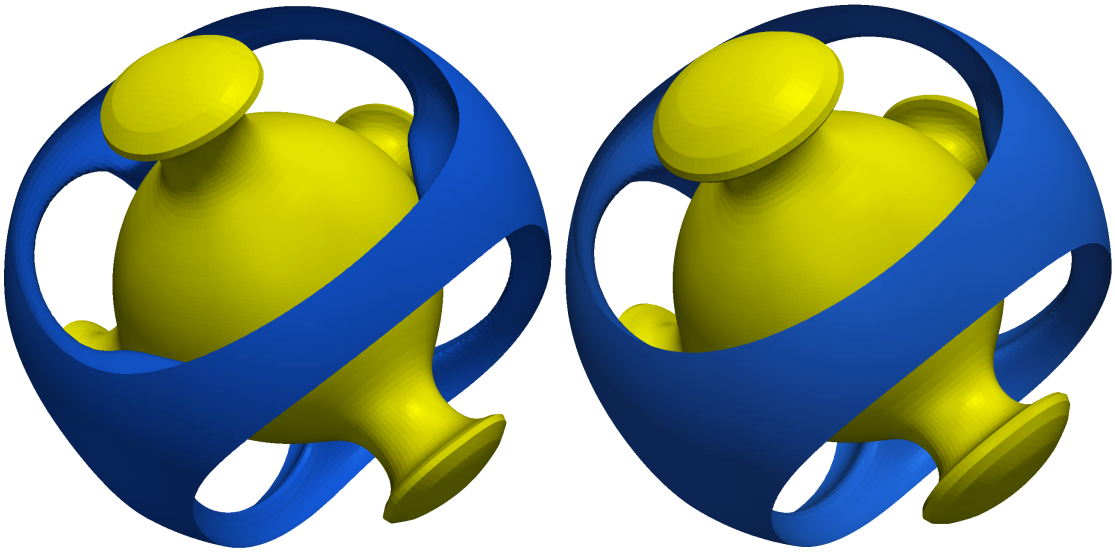

Figure A.9. Temperature field at steady state for the time-dependent benchmark. Shown are contours at temperatures 0.05 (blue) and 0.5 (yellow). Left: isoviscous model. Right: model with viscosity variation of factor 20.

A.6.4 Adaptive Resolution of Rising Plume

In the final benchmark presented here, we illustrate the effectiveness of mesh adaptation. We compute plume models in a $45° \times 45°$ section of a spherical shell, with an initial temperature field given by

$$T(\boldsymbol{x}) = T_0 + \exp\left(-\frac{1}{2\sigma^2}\|\boldsymbol{x} - \boldsymbol{x}_0\|^2\right), \tag{A.36}$$

where $\sigma = 1/20$ determines the extent of the anomaly and $\boldsymbol{x}_0$ denotes its center, situated $D/10$ below the core-mantle boundary (which is outside of the domain, but still has an effect in the lower mantle). A thermal boundary layer is used at the bottom of the domain for $r < r_b + w_{\mathsf{TBL}}$ with w_{TBL} chosen to cover the bottom-most 500 km. This temperature profile is described using an error function:

$$T_0 = 1.0 - 0.5\,\mathrm{erf}\frac{(r - r_b)}{w_{\mathsf{TBL}}/2}. \tag{A.37}$$

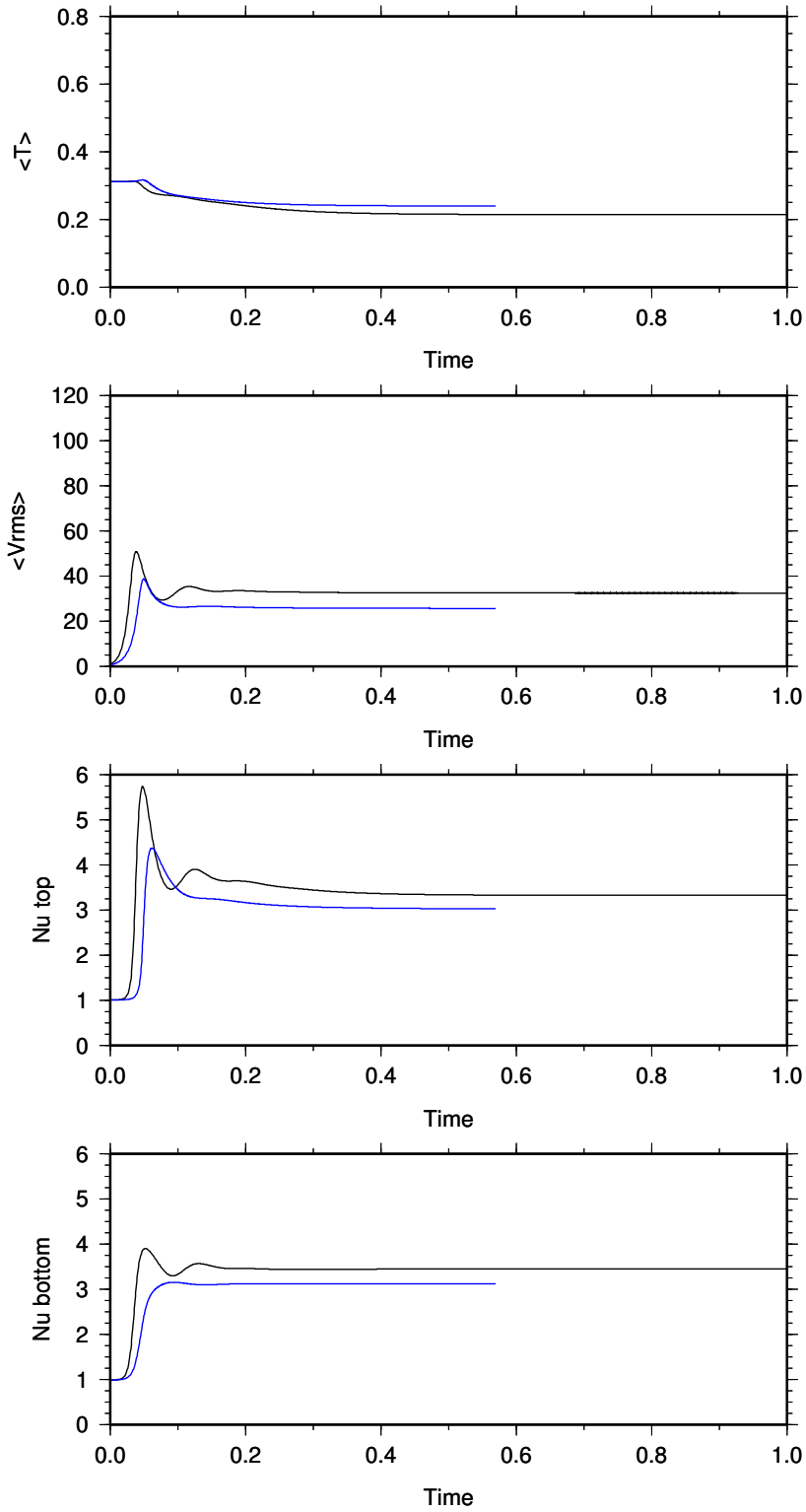

Figure A.10. Measured quantities in time-dependent convection models with a temperature perturbation of degree 4 and order 0. Shown are the average temperature, root mean square velocity, and Nusselt numbers at top and bottom of the mantle. Black: isoviscous model. Blue: model with viscosity variation of factor 20.

$\mathrm{Ra}, \mathrm{t}_{\mathrm{model}}$	Level	# elements	# cores	t_{comp}(s)	V_{rms} error
10^4, 8.0×10^{-2}	Level 7 uniform	2^{21} ($= 128^3$)	192	1.6268×10^7	-
	Level 7 coarsened	2^{18}	96	2.1181×10^6	0.029
	Level 6 uniform	2^{18} ($= 64^3$)	24	9.1380×10^5	0.044
	Level 7 coarsened	2^{16}	24	3.2419×10^5	0.083
	Level 7 coarsened	2^{15}	24	2.0125×10^5	0.159
	Level 5 uniform	2^{15} ($= 32^3$)	8	6.0709×10^4	0.226
10^6, 5.0×10^{-4}	Level 8 uniform	2^{24} ($= 256^3$)	1536	5.7819×10^7	-
	Level 8 coarsened	2^{21}	768	7.1220×10^6	0.019
	Level 7 uniform	2^{21} ($= 128^3$)	192	5.5831×10^6	0.249
	Level 8 coarsened	2^{19}	192	1.7953×10^6	0.272
	Level 8 coarsened	2^{18}	192	1.0900×10^6	0.279
	Level 6 uniform	2^{18} ($= 64^3$)	192	4.9778×10^6	0.800

Table A.5. Comparison of the time evolution of a rising plume on static uniform and dynamically adapted meshes. The first column lists the Rayleigh number and the nondimensional model time at which errors are assessed. The second column indicates the mesh level at the start of the simulation, while the third column contains the number of elements after adaptive meshing. The fourth column shows the number of cores used for the computation. The fifth column shows the total compute time $\mathrm{t}_{\mathrm{comp}}$, computed as the overall run time in seconds times the number of cores used for the computation. The last column shows the relative error in V_{rms} compared with the highest resolution uniform mesh case.

Elsewhere, the background temperature T_0 is 0.5. The Rayleigh number is set to 10^4 and 10^6, respectively (Figure A.11). The viscosity is given by (A.35), with $E = 7.0$. The solutions for meshes with various amounts of coarsening are compared to the solution obtained on a uniform mesh. We start with a static uniform mesh in both cases, using mesh level 7 (2^{21} elements) for the model with $\mathrm{Ra} = 10^4$, and mesh level 8 (2^{24} elements) for the model with $\mathrm{Ra} = 10^6$. Time series of the average temperature, average root mean square velocity, and Nusselt numbers at the top and bottom of the mantle are computed. We then decrease the number of elements using dynamic adaptive coarsening in consecutive model runs (Table A.5), but only allow a maximum decrease in resolution of two mesh levels. These coarsened models are then compared to models with uniform meshes with the same total number of elements.

The time series show that in the case with Rayleigh number 10^4, a steady state develops

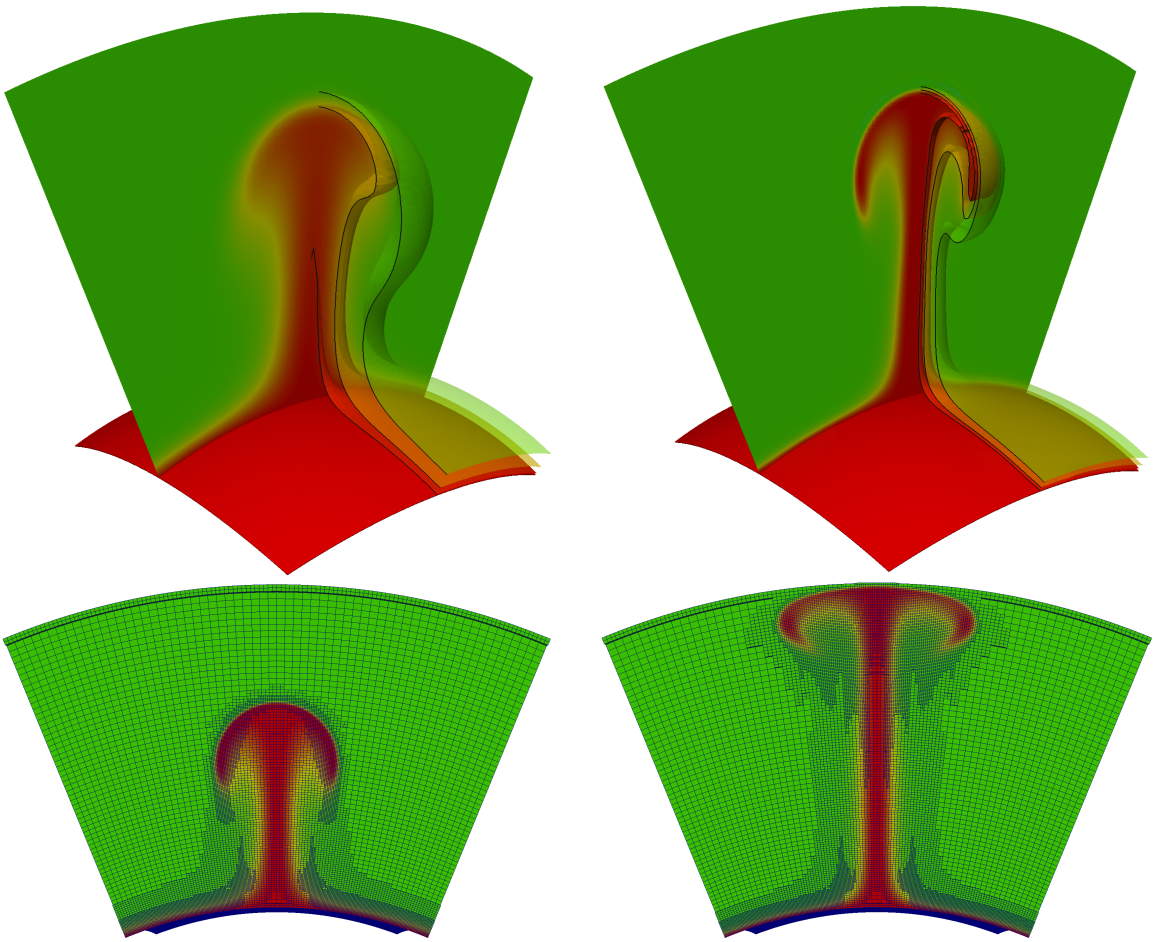

Figure A.11. Temperature field for plume models. Shown are contours at temperatures 0.6, 0.8, and 0.95. Top left: Model with uniform mesh at level 6 (2^{18} elements) and Rayleigh number 10^4 at $t = 6.95 \times 10^{-3}$. Top right: Model with uniform mesh at level 7 (2^{21} elements) and Rayleigh number 10^6 at $t = 7.54 \times 10^{-5}$. Bottom: Cross-sections showing temperature and mesh of a model with coarsening from level 8 to 2^{21} elements and $Ra = 10^6$, at $t = 5.91 \times 10^{-5}$ (left) and at $t = 1.24 \times 10^{-4}$ (right).

(Figure A.12). Quantitative comparisons are provided in Table A.5. The models with 2^{18} elements reproduce the results of the uniform high-resolution mesh (2^{21} elements) well, and the adaptive better than the uniform. The model with 2^{18} elements coarsened from level 7 has a smaller V_{rms} error than the model with uniform mesh at level 6, as does the coarsened model with 2^{15} elements compared to the model with uniform mesh at level 5. Comparing the uniform high-resolution model with the adapted one at the same number of elements, it can be seen that adaptivity allows an overall 8x reduction in both elements and run time, only with a minor loss in accuracy. Choosing increasingly coarser models, the errors increase gradually, which is expected at this Rayleigh number: The temperature field is smooth and does not show sharp features.

The models with a Rayleigh number of 10^6 show a much increased sensitivity to mesh resolution. The plume is narrower, temperature gradients are sharper, and flow velocities are larger with increased Rayleigh number. In this model, no steady-state solution is achieved. The original plume is only stable up to $t_{\mathrm{model}} \sim 3 \times 10^{-4}$, and is then replaced with smaller, more ephemeral features for the duration of the model run. These features are harder to resolve than the original plume, and therefore a uniform reduction in the number of elements under-resolves the solution and eventually fails (see Figure A.12). In contrast, an adaptive coarsening from level 8 to 2^{21} elements reproduces the results from the uniform level 8 mesh (2^{24} elements) well in 8x less run time, and provides a 12x smaller error than the the model with a uniform level 7 mesh at the same number of elements (see again Table A.5). This adaptive model is the only lower cost variant that yields an acceptable error. Considering a further reduction of the problem size, the model with 2^{18} elements adaptively coarsened from a level 8 mesh has a much reduced error compared with a uniform level 6 mesh (also 2^{18} elements). These results indicate that adaptive coarsening can preserve high accuracy

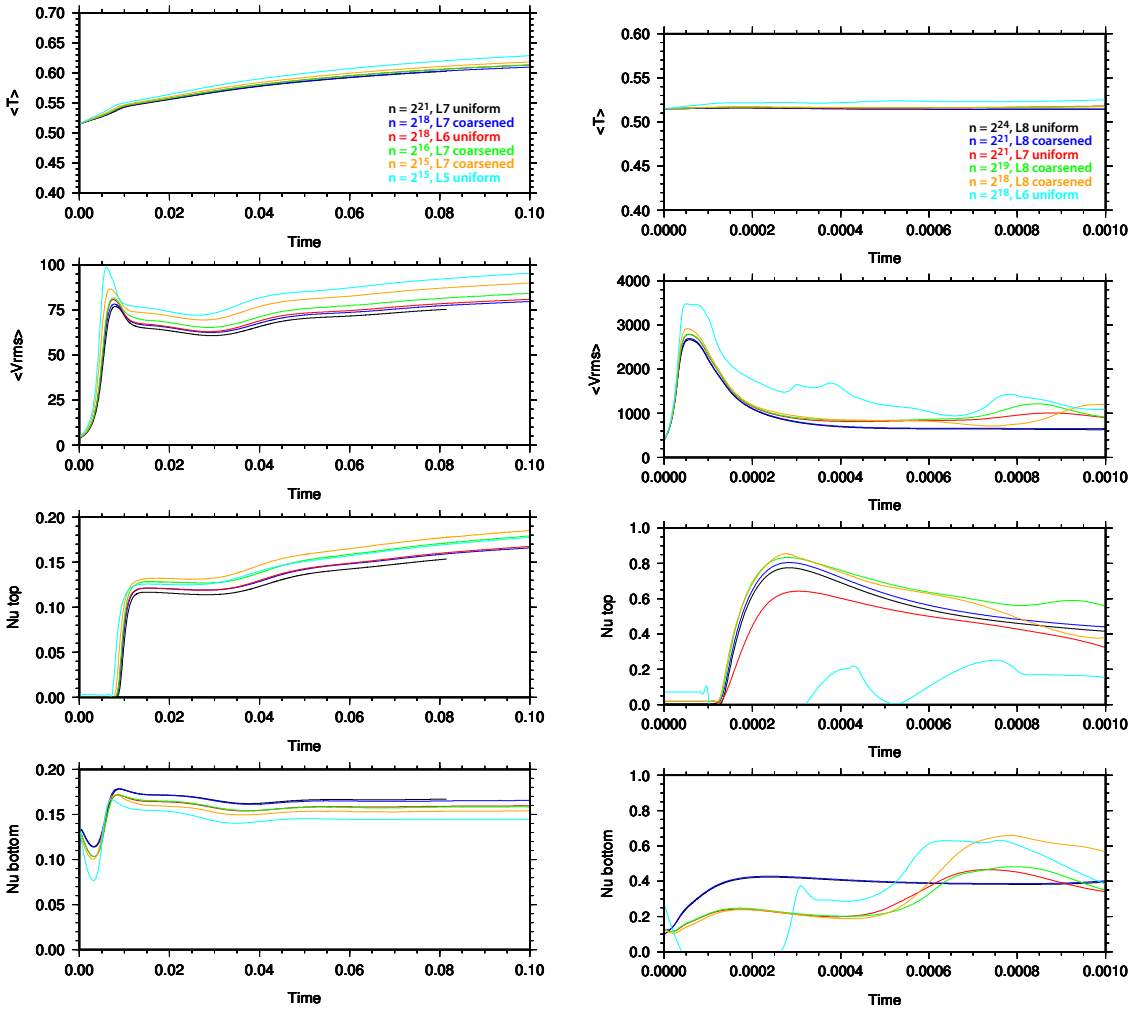

Figure A.12. Measured quantities in plume model, for decreasing number of elements. Shown are the average temperature, root mean square velocity, and Nusselt numbers at top and bottom of the mantle. Left: Rayleigh number 10^4. Right: Rayleigh number 10^6.

while providing a much faster time to solution. When Rayleigh numbers become large, the adaptive simulation becomes increasingly favorable compared to a uniform mesh simulation of the same element count.

A.7 Discussion and Conclusions

In this article we have presented the design and functionality of the `Rhea` code for instantaneous and time-dependent simulation of mantle convection. The uniqueness of `Rhea` lies in

the combination of dynamic adaptive mesh refinement capabilities that enable the resolution of multiple scales, and large-scale parallel scalability that enables efficient use of petaflop-class supercomputers. `Rhea` has been used previously to simulate global mantle convection to one-kilometer resolution, satisfactorily recovering the motion of plates and microplates. In this document we detail the choices made for the computational algorithms and numerical solvers, and the technical background for their implementation, and we discuss their performance and accuracy using problems with exact solutions, as well as community benchmarks. In all cases, our focus was on maximal algorithmic efficiency, which is reflected in the following considerations.

We cover the computational domain by what we call a forest of octrees — a collection of conforming mapped hexahedra, each of which is the root of an adaptive octree. This leads to logically cubic elements that feature hanging faces and edges when elements of different sizes meet. The main benefit of this approach is that it allows us to define a space filling curve that we exploit for fast mesh partitioning and search of element neighbors. In particular, we do not depend on external graph-partitioning software that would introduce additional overhead and complexity.

We choose continuous trilinear finite elements for both the velocity and the pressure. The introduction of an element-wise projection term in the pressure block stabilizes the Stokes system and allows us to handle all variables within the same fast finite element framework. Since this term can potentially introduce artificial compressibility, we are considering different-order velocity pressure pairings. However, higher-order finite elements for the velocity complicate the preconditioning of the Stokes operator.

To apply the inverse of the block-diagonal preconditioner we use an algebraic multigrid solver for the viscous operator and approximate the inverse of the pressure Schur complement

with an inverse-viscosity pressure mass matrix. This preconditioner is symmetric, as is the original Stokes system, and thus allows us to use the MINRES iterative solver that does not need to store a history of previous iterates as opposed to GMRES variants. Block-triangular preconditioners are interesting alternatives promising faster convergence at the cost of destroying the symmetry of the system. The viscosity-scaled mass matrix is a reasonable approximation of the Schur complement for smoothly varying viscosity. However, for extreme viscosity gradients, the approximation degrades, and convergence of the iterative solver can become slower.

The α-predictor-corrector iteration that we use for time integration is well established in elastodynamics and other finite element applications. While the early truncation of the iteration yields a rather small residual, it still implies that the method is not implicit and thus limits the time step by a Courant-Friedrich-Levy condition. Since we operate in the advection dominated regime, the quadratic dependence of the diffusion time step on the mesh size does not take effect and the linear dependence due to the advection component prevails. This situation may change at resolutions of roughly 10 m for a global run, which seems far beyond the accuracy of current tectonic models. Still, we may consider treating at least the diffusion term implicitly, or to switch to fully implicit time integrators. Another alternative is to consider an altogether different approach to solving the energy equation, for example using a discontinuous Galerkin method. Finally, the time step size limit may be considered separately for each element to avoid over-resolution in time for large elements. These are common challenges that will generally need to be addressed in future AMR simulations.

Having outlined the design principles of `Rhea`, we demonstrate its correctness by the method of manufactured solutions, and by solving a series of community benchmark problems both instantaneous and time-dependent. We argue that adaptivity has the potential to increase accuracy and reduce the computation time for high-Rayleigh-number simulations such

as presented by the Earth's geodynamics. We demonstrate the parallel efficiency of `Rhea` by scaling a variable-viscosity Stokes solve to 122,880 cores of the Jaguar supercomputer. Our results indicate that `Rhea` is indeed an accurate and scalable code for simulating global mantle convection and possibly other thermal convection scenarios.

Acknowledgments

The authors would like to thank Shijie Zhong for discussion and feedback. The NSF PetaApps program (OCI-0749334, OCI-0748898), TeraGrid allocation (TG-MCA04N026), and further grants (EAR-0426271, EAR-0810303, CCF-0427985, DMS-072474) are gratefully acknowledged, as well as funding by the DOE Office of Science (DE-FC02-06ER25782, DE-SC0002710) and support by the Caltech Tectonics Observatory (by the Gordon and Betty Moore Foundation). The Texas Advanced Computing Center (TACC) and Oak Ridge National Laboratories provided outstanding help and support for our use of the Ranger and Jaguar supercomputers, respectively.

Bibliography

Ainsworth, M., and J. T. Oden, *A posteriori error estimation in finite element analysis*, Pure and Applied Mathematics, John Wiley & Sons, New York, 2000.

Alisic, L., M. Gurnis, G. Stadler, C. Burstedde, L. C. Wilcox, and O. Ghattas, Slab stress and strain rate as constraints on global mantle flow, *Geophysical Research Letters*, *37*, L22,308, doi:10.1029/2010GL045312, 2010.

Alisic, L., M. Gurnis, G. Stadler, C. Burstedde, and O. Ghattas, Multi-scale dynamics and rheology of mantle flow with plates, *Journal of Geophysical Research*, submitted, 2012.

Alpert, L. A., T. W. Becker, and I. W. Bailey, Global slab deformation and centroid moment tensor constraints on viscosity, *Geochemistry, Geophysics, Geosystems*, *11*(12), Q12,006, doi:10.1029/2010GC003301, 2010.

Andersen, T. B., K. Mair, H. Austrheim, Y. Y. Podladchikov, and J. C. Vrijmoed, Stress release in exhumed intermediate and deep earthquakes determined from ultramafic pseudotachylyte, *Geology*, *36*(12), 995–998, doi:10.1130/G25230A.1, 2008.

Anderson, D. L., Top-down tectonics?, *Science*, *293*, 2016–2018, 2001.

Andrews, E. R., and M. I. Billen, Rheologic controls on the dynamics of slab detachment, *Tectonophysics*, *464*, 60–69, doi:10.1016/j.tecto.2007.09.004, 2009.

Argus, D. F., and R. G. Gordon, No-net-rotation model of current plate velocities incorporating plate motion model NUVEL-1, *Geophysical Research Letters*, *18*(11), 2039–2042, 1991.

Argus, D. F., R. G. Gordon, and C. DeMets, Geologically current motion of 56 plates relative to the no-net-rotation reference frame, *Geochemistry, Geophysics, Geosystems*, *12*(11), Q11,001, doi:10.1029/2011GC003751, 2011.

Austermann, J., Z. Ben-Avraham, P. Bird, O. Heidbach, G. Schubert, and J. M. Stock, Quantifying the forces needed for the rapid change of Pacific plate motion at 6 Ma, *Earth and Planetary Science Letters*, *307*, 289–297, doi:10.1016/j.epsl.2011.04.043, 2011.

Barker, P. F., Scotia Sea regional tectonic evolution: Implications for mantle flow and palaeocirculation, *Earth-Science Reviews*, *55*, 1–39, 2001.

Batchelor, G. K., *An Introduction to Fluid Dynamics*, Cambridge University Press, 1967.

Becker, R., and R. Rannacher, An optimal control approach to a posteriori error estimation in finite element methods, *Acta Numerica*, *10*, 1–102, 2001.

Becker, T. W., On the effect of temperature and strainrate dependent viscosity on global mantle flow, net rotation, and platedriving forces, *Geophysical Journal International*, *167*, 943–957, doi:10.1111/j.1365-246X.2006.03172.x, 2006.

Becker, T. W., and R. J. O'Connell, Predicting plate velocities with mantle circulation models, *Geochemistry, Geophysics, Geosystems*, *2*, 2001.

Bercovici, D., G. Schubert, G. A. Glatzmaier, and A. Zebib, 3-dimensional thermal-convection in a spherical shell, *Journal of Fluid Mechanics*, *206*, 75–104, 1989.

Berger, M. J., and R. J. LeVeque, Adaptive mesh refinement using wave-propagation algorithms for hyperbolic systems, *SIAM Journal on Numerical Analysis*, *35*(6), 2298–2316, 1998.

Bevis, M., Seismic slip and down-dip strain rates in Wadati-Benioff zones, *Science*, *240*(4857), 1317–1319, 1988.

Billen, M. I., Modeling the dynamics of subducting slabs, *Annual Reviews of Earth and Planetary Sciences*, *36*, 325–356, doi:10.1146/annurev.earth.36.031207.124129, 2008.

Billen, M. I., and M. Gurnis, Constraints on subducting plate strength within the Kermadec trench, *Journal of Geophysical Research*, *110*(B5), B05,407, doi:10.1029/2004JB003308, 2005.

Billen, M. I., and G. Hirth, Rheologic controls on slab dynamics, *Geochemistry, Geophysics, Geosystems*, *8*, Q08,012, doi:10.1029/2007GC001597, 2007.

Billen, M. I., and M. Jadamec, Origin of localized fast mantle flow velocity in numerical models of subduction, *Geochemistry, Geophysics, Geosystems*, *13*(1), Q01,016, doi:10.1029/2011GC003856, 2012.

Billen, M. I., M. Gurnis, and M. Simons, Multiscale dynamics of the Tonga-Kermadec subduction zone, *Geophysical Journal International*, *153*(2), 359–388, 2003.

Bird, P., An updated digital model of plate boundaries, *Geochemistry, Geophysics, Geosystems*, *4*, 1027, doi:10.1029/2001GC000252, 2003.

Bochev, P., C. Dohrmann, and M. Gunzburger, Stabilization of low-order mixed finite elements for the Stokes equations, *SIAM Journal on Numerical Analysis*, *44*, 82–101, 2006.

Bower, D. J., M. Gurnis, and M. Seton, High bulk modulus structures in the lower mantle from dynamic Earth models with paleogeography, in preparation, 2012.

Boyden, J. A., R. D. Müller, M. Gurnis, T. H. Torsvik, J. A. Clark, M. Turner, H. Ivey-Law, R. J. Watson, and J. S. Cannon, Next-generation plate-tectonic reconstructions using GPlates, in

Geoinformatics: Cyberinfrastructure for the Solid Earth Sciences, pp. 95–113, Cambridge University Press, 2011.

Briggs, W. L., V. E. Henson, and S. McCormick, *A Multigrid Tutorial*, 2nd ed., SIAM, 2000.

Brooks, A. N., and T. J. R. Hughes, Streamline upwind/Petrov–Galerkin formulations for convection dominated flows with particular emphasis on the incompressible Navier–Stokes equations, *Computer Methods in Applied Mechanics and Engineering*, *32*, 199–259, 1982.

Buffett, B. A., and D. B. Rowley, Plate bending at subduction zones: Consequences for the direction of plate motions, *Earth and Planetary Science Letters*, *245*(1-2), 359–364, doi:10.1016/j.epsl.2006.03.011, 2006.

Burstedde, C., O. Ghattas, M. Gurnis, E. Tan, T. Tu, G. Stadler, L. C. Wilcox, and S. Zhong, Scalable adaptive mantle convection simulation on petascale supercomputers, in *SC '08: Proceedings of the International Conference for High Performance Computing, Networking, Storage, and Analysis*, ACM/IEEE, 2008a.

Burstedde, C., O. Ghattas, G. Stadler, T. Tu, and L. C. Wilcox, Towards adaptive mesh PDE simulations on petascale computers, in *Proceedings of Teragrid '08*, 2008b.

Burstedde, C., M. Burtscher, O. Ghattas, G. Stadler, T. Tu, and L. C. Wilcox, ALPS: A framework for parallel adaptive PDE solution, *Journal of Physics: Conference Series*, *180*, 012,009, doi:10.1088/1742-6596/180/1/012009, 2009a.

Burstedde, C., O. Ghattas, G. Stadler, T. Tu, and L. C. Wilcox, Parallel scalable adjoint-based adaptive solution for variable-viscosity Stokes flows, *Computer Methods in Applied Mechanics and Engineering*, *198*, 1691–1700, doi:10.1016/j.cma.2008.12.015, 2009b.

Burstedde, C., O. Ghattas, M. Gurnis, T. Isaac, A. Klöckner, G. Stadler, T. Warburton, and L. C. Wilcox, Extreme-scale AMR, in *SC '10: Proceedings of the International Conference for High Performance Computing, Networking, Storage, and Analysis*, ACM/IEEE, 2010.

Burstedde, C., L. C. Wilcox, and O. Ghattas, `p4est`: Scalable algorithms for parallel adaptive mesh refinement on forests of octrees, *SIAM Journal on Scientific Computing*, *33*(3), 1103–1133, doi:10.1137/100791634, 2011.

Burstedde, C., G. Stadler, L. Alisic, L. C. Wilcox, E. Tan, M. Gurnis, and O. Ghattas, Large-scale adaptive mantle convection simulation, *Geophysical Journal International*, submitted, 2012.

Cande, S. C., and D. R. Stegman, Indian and African plate motions driven by the push force of the Réunion plume head, *Nature*, *475*, 47–52, doi:10.1038/nature10174, 2011.

Carminati, E., and P. Petricca, State of stress in slabs as a function of large-scale plate kinematics, *Geochemistry, Geophysics, Geosystems*, *11*(4), Q04,006, doi:10.1029/2009GC003003, 2010.

Choblet, G., O. Cadek, F. Couturier, and C. Dumoulin, OEDIPUS: a new tool to study the dynamics of planetary interiors, *Geophysical Journal International*, *170*(1), 9–30, 2007.

Christensen, U., Convection with pressure- and temperature-dependent non-newtonian rheology, *Geophysical Journal of the Royal Astronomical Society*, *77*, 343–384, 1984.

Cizkova, H., J. van Hunen, A. P. van den Berg, and N. J. Vlaar, The influence of rheological weakening and yield stress on the interaction of slabs with the 670 km discontinuity, *Earth and Planetary Science Letters*, *199*, 447–457, 2002.

Conrad, C. P., and M. D. Behn, Constraints on lithosphere net rotation and asthenospheric viscosity from global mantle flow models and seismic anisotropy, *Geochemistry, Geophysics, Geosystems*, *11*(5), Q05W05, doi:10.1029/2009GC002970, 2010.

Conrad, C. P., and B. H. Hager, Effects of plate bending and fault strength at subduction zones on plate dynamics, *Journal of Geophysical Research*, *104*(B8), 17,551–17,571, 1999a.

Conrad, C. P., and B. H. Hager, The thermal evolution of an earth with strong subduction zones, *Geophysical Research Letters*, *26*(19), 3041–3044, 1999b.

Conrad, C. P., and B. H. Hager, Mantle convection with strong subduction zones, *Geophysical Journal International*, *144*(2), 271–288, 2001.

Conrad, C. P., and C. Lithgow-Bertelloni, How mantle slabs drive plate tectonics, *Science*, *298*(5591), 207–209, 2002.

Conrad, C. P., and C. Lithgow-Bertelloni, The temporal evolution of plate driving forces: Importance of "slab suction" versus "slab pull" during the Cenozoic, *Journal of Geophysical Research*, *109*, B10,407, doi:10.1029/2004JB002991, 2004.

Cottrell, J. A., T. J. R. Hughes, and Y. Bazilevs, *Isogeometry Analysis*, John Wiley & Sons, Ltd., 2009.

Crowley, J. W., and R. J. O'Connell, An analytic model of convection in a system with layered viscosity and plates, *Geophysical Journal International*, *188*, 61–78, doi:10.1111/j.1365-246X.2011.05254.x, 2012.

Davies, D. R., J. H. Davies, O. Hassan, K. Morgan, and P. Nithiarasu, Investigations into the applicability of adaptive finite element methods to two-dimensional infinite Prandtl num-

ber thermal and thermochemical convection, *Geochemistry, Geophysics, Geosystems*, *8*(5), Q05,010, doi:10.1029/2006GC001470, 2007.

Davies, D. R., C. R. Wilson, and S. C. Kramer, Fluidity: A fully unstructured anisotropic adaptive mesh computational modeling framework for geodynamics, *Geochemistry, Geophysics, Geosystems*, *12*(6), Q06,001, 2011.

Davies, G. F., *Dynamic Earth: Plates Plumes and Mantle Convection*, Cambridge University Press, Cambridge, 1999.

De Sterck, H., U. M. Yang, and J. J. Heys, Reducing complexity in parallel algebraic multigrid preconditioners, *SIAM Journal on Matrix Analysis and Applications*, *27*(4), 1019–1039, doi:10.1137/040615729, 2006.

DeMets, C., R. G. Gordon, D. F. Argus, and S. Stein, Effect of recent revisions to the geomagnetic reversal time scale on estimates of current plate motions, *Geophysical Research Letters*, *21*(20), 2191–2194, 1994.

Dewey, J. F., Episodicty, sequence, and style at convergent plate boundaries, in *The Continental Crust and Its Mineral Deposits*, edited by D. W. Strangway, pp. 553–573, Geological Association of Canada, 1980.

Diachin, L. F., R. Hornung, P. Plassmann, and A. Wissink, Parallel adaptive mesh refinement, in *Parallel Processing for Scientific Computing*, edited by M. A. Heroux, P. Raghavan, and H. D. Simon, no. 20 in Software, Environments, and Tools, pp. 143–162, SIAM, 2006.

Dohrmann, C., and P. Bochev, A stabilized finite element method for the Stokes problem based on polynomial pressure projections, *International Journal for Numerical Methods in Fluids*, *46*, 183–201, doi:10.1002/fld.752, 2004.

Dziewonski, A. M., and D. L. Anderson, Preliminary reference earth model, *Physics of the Earth and Planetary Interiors*, *25*(4), 297–356, 1981.

Elman, H. C., D. J. Silvester, and A. J. Wathen, *Finite Elements and Fast Iterative Solvers with applications in incompressible fluid dynamics*, Oxford University Press, Oxford, 2005.

Elsasser, W. M., Convection and stress propagation in the upper mantle, in *The application of modern physics to the Earth and planetary interiors*, edited by S. Runcorn, Wiley-Interscience, 1969.

Enns, A., T. W. Becker, and H. Schmeling, The dynamics of subduction and trench migration for viscosity stratification, *Geophysical Journal International*, *160*, 761–775, doi:10.1111/j.1365-246X.2005.02519.x, 2005.

Faccenda, M., L. Burlini, T. V. Gerya, and D. Mainprice, Fault-induced seismic anisotropy by hydration in subducting oceanic plates, *Nature*, *455*, 1097–1101, doi:10.1038/NGEO656, 2008.

Faccenna, C., A. Heuret, F. Funiciello, S. Lallemand, and T. W. Becker, Predicting trench and plate motion from the dynamics of a strong slab, *Earth and Planetary Science Letters*, *257*, 29–36, 2007.

Faccenna, C., T. W. Becker, S. Lallemand, and B. Steinberger, On the role of slab pull in the Cenozoic motion of the Pacific plate, *Geophysical Research Letters*, *39*, L03,305, doi:10.1029/2011GL050155, 2012.

Falgout, R., An introduction to algebraic multigrid, *Computing in Science and Engineering*, *8*, 24–33, 2006.

Flaherty, J. E., R. M. Loy, M. S. Shephard, B. K. Szymanski, J. D. Teresco, and L. H. Ziantz, Adaptive local refinement with octree load balancing for the parallel solution of three-dimensional conservation laws, *Journal of Parallel and Distributed Computing*, *47*(2), 139–152, doi:10.1006/jpdc.1997.1412, 1997.

Forte, A., Constraints on seismic models from other disciplines – Implications for mantle dynamics and composition, in *Treatise on Geophysics, vol. 1: Seismology and the Structure of the Earth*, edited by B. Romanowicz and A. Dziewonski, pp. 805–858, Elsevier, Amsterdam, 2007.

Fukao, Y., and M. Kikuchi, Source retrieval for mantle earthquakes by iterative deconvolution of long-period P-waves, *Tectonophysics*, *144*(1–3), 249–269, 1987.

Funiciello, F., C. Faccenna, A. Heuret, S. Lallemand, E. D. Giuseppe, and T. W. Becker, Trench migration, net rotation and slabmantle coupling, *Earth and Planetary Science Letters*, *271*, 233–240, doi:10.1016/j.epsl.2008.04.006, 2008.

Gee, M. W., C. M. Siefert, J. J. Hu, R. S. Tuminaro, and M. G. Sala, ML 5.0 smoothed aggregation user's guide, *Tech. Rep. SAND2006-2649*, Sandia National Laboratories, 2006.

Geenen, T., M. ur Rehman, S. P. MacLachlan, G. Segal, C. Vuik, A. P. van den Berg, and W. Spakman, Scalable robust solvers for unstructured FE geodynamic modeling applications: Solving the Stokes equation for models with large localized viscosity contrasts, *Geochemistry, Geophysics, Geosystems*, *10*, Q09,002, doi:10.1029/2009GC002526, 2009.

Gordon, R., and S. Stein, Global tectonics and space geodesy, *Science*, *256*, 333–342, doi:10.1126/science.256.5055.333, 1992.

Gordon, R. G., and D. M. Jurdy, Cenozoic global plate motions, *Journal of Geophysical Research*, *91*, 12,389–12,406, 1986.

Gordon, R. G., C. DeMets, and J.-Y. Royer, Evidence for long-term diffuse deformation of the lithosphere of the equatorial Indian Ocean, *Nature*, *395*, 370–374, doi: 10.1038/26463, 1998.

Grevemeyer, I., N. Kaul, J. L. Diaz-Naveas, H. W. Villinger, C. R. Ranero, and C. Reichert, Heat flow and bending-related faulting at subduction trenches: Case studies offshore of Nicaragua and Central Chile, *Earth and Planetary Science Letters*, *236*, 238–248, doi:10.1016/j.epsl.2005.04.048, 2005.

Grinevich, P. P., and M. A. Olshanskii, An iterative method for the Stokes-type problem with variable viscosity, *SIAM Journal on Scientific Computing*, *31*(5), 3959–3978, 2009.

Gripp, A. E., and R. G. Gordon, Current plate velocities relative to the hotspots incorporating the NUVEL1 global plate motion model, *Geophysical Research Letters*, *17*, 1109–1112, 1990.

Gripp, A. E., and R. G. Gordon, Young tracks of hotspots and current plate velocities, *Geophysical Journal International*, *150*, 321–361, 2002.

Gudmundsson, O., and M. Sambridge, A regionalized upper mantle (RUM) seismic model, *Journal of Geophysical Research*, *103*(B4), 7121–7136, 1998.

Gurnis, M., and B. Hager, Controls on the structure of subducted slabs, *Nature*, *335*, 317–321, 1988.

Gurnis, M., J. Ritsema, H.-J. van Heijst, and S. Zhong, Tonga slab deformation: The influence

of a lower mantle upwelling on a slab in a young subduction zone, *Geophysical Research Letters*, *27*(16), 2373–2376, 2000a.

Gurnis, M., S. Zhong, and J. Toth, On the competing roles of fault reactivation and brittle failure in generating plate tectonics from mantle convection, *Geophysical Monograph*, *121*, 73–94, 2000b.

Gurnis, M., C. Hall, and L. Lavier, Evolving force balance during incipient subduction, *Geochemistry, Geophysics, Geosystems*, *5*(7), Q07,001, doi:10.1029/2003GC000681, 2004.

Gurnis, M., D. J. Bower, and N. Flament, Assimilating lithosphere and slab history in 4-D dynamic Earth models, in preparation, 2012a.

Gurnis, M., et al., Plate tectonic reconstructions with continuously closing plates, *Computers & Geosciences*, doi:10.1016/j.cageo.2011.04.014, 2012b.

Hager, B. H., and R. J. O'Connell, A simple global model of plate dynamics and mantle convection, *Journal of Geophysical Research*, *86*, 4843–4867, 1981.

Hager, B. H., and M. A. Richards, Long-wavelength variations in Earth's geoid: physical models and dynamical implications, *Philosophical Transactions of the Royal Society of London. Series A, Mathematical and Physical Sciences*, *328*, 309–327, 1989.

Hall, C. E., M. Gurnis, M. Sdrolias, L. L. Lavier, and R. D. Müller, Catastrophic initiation of subduction following forced convergence across fracture zones, *Earth and Planetary Science Letters*, *212*, 15–30, 2003.

Hebert, L. B., P. Antoshechkina, P. Asimow, and M. Gurnis, Emergence of a low-viscosity channel in subduction zones through the coupling of mantle flow and thermodynamics, *Earth and Planetary Science Letters*, *278*, 243–256, doi:10.1016/j.epsl.2008.12.013, 2009.

Hirth, G., and D. Kohlstedt, Rheology of the upper mantle and the mantle wedge: a view from the experimentalists, *Geophysical Monograph*, *138*, 83–105, 2003.

Holt, W., Flow fields within the Tonga slab determined from the moment tensors of deep earthquakes, *Geophysical Research Letters*, *22*(8), 989–992, 1995.

Hughes, T. J. R., *The Finite Element Method*, Dover, New York, 2000.

Isacks, B., and P. Molnar, Distribution of stresses in descending lithosphere from a global survey of focal mechanism solutions of mantle earthquakes, *Reviews of Geophysics and Space Physics*, *9*(1), 103–174, 1971.

Jadamec, M. A., and M. I. Billen, Reconciling surface plate motions with rapid three-dimensional mantle flow around a slab edge, *Nature*, *456*, 338–342, doi:10.1038/nature09053, 2010.

Jarrard, R. D., Relations among subduction parameters, *Reviews of Geophysics*, *24*(2), 217–284, 1986.

Judge, A. V., and M. K. McNutt, The relationship between plate convergence and elastic plate thickness: A study of the Peru-Chile trench, *Journal of Geophysical Research*, *96*(B10), 16,625–16,639, 1991.

Kanamori, H., and E. E. Brodsky, The physics of earthquakes, *Reports on Progress in Physics*, *67*, 1429–1496, doi:10.1088/0034-4885/67/8/R03, 2004.

Kanamori, H., D. L. Anderson, and T. H. Heaton, Frictional melting during the rupture of the 1994 Bolivian earthquake, *Science*, *279*(5352), 839–842, 1998.

Karato, S., and B. B. Karki, Origin of lateral variation of seismic wave velocities and densities in the deep mantle, *Journal of Geophysical Research*, *106*(B10), 21,771–21,783, 2001.

Karato, S., and P. Wu, Rheology of the upper mantle: A synthesis, *Science*, *260*(5109), 771–778, 1993.

Kikuchi, M., and H. Kanamori, The Shikotan earthquake of October 4, 1994: Lithosphere earthquake, *Geophysical Research Letters*, *22*, 1025–1028, 1995.

King, S. D., J. P. Lowman, and C. W. Gable, Episodic tectonic plate reorganizations driven by mantle convection, *Earth and Planetary Science Letters*, *203*, 83–91, 2002.

Kohlstedt, D. L., B. Evans, and S. J. Mackwell, Strength of the lithosphere: Constraints imposed by laboratory experiments, *Journal of Geophysical Research*, *100*(B9), 17,587–17,602, 1995.

Kreemer, C., Absolute plate motions constrained by shear wave splitting orientations with implications for hot spot motions and mantle flow, *Journal of Geophysical Research*, *114*, B10,405, doi:10.1029/2009JB006416, 2009.

Kreemer, C., W. E. Holt, and A. J. Haines, An integrated global model of present-day plate motions and plate boundary deformation, *Geophysical Journal International*, *154*, 8–34, 2003.

Kreemer, C., D. A. Lavallée, G. Blewitt, and W. E. Holt, On the stability of a geodetic no-net-rotation frame and its implication for the International Terrestrial Reference Frame, *Geophysical Research Letters*, *33*, L17,306, doi:10.1029/2006GL027058, 2006.

Lallemand, S., A. Heuret, and D. Boutelier, On the relationships between slab dip, back-arc stress, upper plate absolute motion, and crustal nature in subduction zones, *Geochemistry, Geophysics, Geosystems*, *6*(9), Q09,006, doi:10.1029/2005GC000917, 2005.

Leng, W., and S. Zhong, Constraints on viscous dissipation of plate bending from compressible mantle convection, *Earth and Planetary Science Letters*, *297*, 154–164, doi:10.1016/j.epsl.2010.06.016, 2010.

Leng, W., and S. Zhong, Implementation and application of adaptive mesh refinement for thermochemical mantle convection studies, *Geochemistry, Geophysics, Geosystems*, *12*, Q04,006, doi:10.1029/2010GC003425, 2011.

Li, C., R. D. van der Hilst, E. R. Engdahl, and S. Burdick, A new global model for p wave speed variations in earths mantle, *Geochemistry, Geophysics, Geosystems*, *9*(5), Q05,018, doi:10.1029/2007GC001806, 2008.

Lithgow-Bertelloni, C., and M. A. Richards, The dynamics of Cenozoic and Mesozoic plate motions, *Reviews of Geophysics*, *26*, 27–78, 1998.

Liu, L., and M. Gurnis, Simultaneous inversion of mantle properties and initial conditions using an adjoint of mantle convection, *Journal of Geophysical Research*, *113*, B08,405, doi:10.1029/2008JB005594, 2008.

Liu, L., and D. R. Stegman, Segmentation of the farallon slab, *Earth and Planetary Science Letters*, *311*, 1–10, doi:10.1016/j.epsl.2011.09.027, 2011.

Long, M. D., and T. W. Becker, Mantle dynamics and seismic anisotropy, *Earth and Planetary Science Letters*, *297*, 341–354, doi:10.1016/j.epsl.2010.06.036, 2010.

Long, M. D., and P. G. Silver, The subduction zone flow field from seismic anisotropy: A global view, *Science*, *319*, 315–318, doi:10.1126/science.1150809, 2008.

Long, M. D., and P. G. Silver, Mantle flow in subduction systems: The subslab flow field

and implications for mantle dynamics, *Journal of Geophysical Research*, *114*, B10,312, doi:10.1029/2008JB006200, 2009.

Luitjens, J., B. Worthen, M. Berzins, and T. C. Henderson, Scalable parallel AMR for the Uintah multiphysics code, in *Petascale Computing Algorithms and Applications*, edited by D. A. Bader, Chapman and Hall/CRC, 2007.

May, D. A., and L. Moresi, Preconditioned iterative methods for Stokes flow problems arising in computational geodynamics, *Physics of the Earth and Planetary Interiors*, *171*, 33–47, 2008.

McKenzie, D. P., J. M. Roberts, and N. O. Weiss, Convection in the Earth's mantle: Towards a numerical solution, *Journal of Fluid Mechanics*, *62*, 465–538, 1974.

Moresi, L., and M. Gurnis, Constraints on the lateral strength of slabs from three-dimensional dynamic flow models, *Earth and Planetary Science Letters*, *138*(1–4), 15–28, 1996.

Müller, R. D., M. Sdrolias, C. Gaina, and W. R. Roest, Age, spreading rates, and spreading asymmetry of the world's ocean crust, *Geochemistry, Geophysics, Geosystems*, *9*, Q04,006, doi:10.1029/2007GC001743, 2008.

Nothard, S., J. Haines, and J. Jackson, Distributed deformation in the subducting lithosphere at Tonga, *Geophysical Journal International*, *127*, 328–338, 1996.

Oden, J. T., and S. Prudhomme, Goal-oriented error estimation and adaptivity for the finite element method, *Computer Methods in Applied Mechanics and Engineering*, *41*, 735–756, 2001.

O'Neill, C., D. Müller, and B. Steinberger, On the uncertainties in hot spot reconstructions and

the significance of moving hot spot reference frames, *Geochemistry, Geophysics, Geosystems*, *6*, Q04,003, doi:10.1029/2004GC000784, 2005.

Paige, C. C., and M. A. Saunders, Solution of sparse indefinite systems of linear equations, *SIAM Journal on Numerical Analysis*, *12*(4), 617–629, 1975.

Parmentier, E. M., D. L. Turcotte, and K. E. Torrance, Studies of finite amplitude non-newtonian thermal convection with application to convection in the earth's mantle, *Journal of Geophysical Research*, *81*(11), 1839–1846, 1976.

Ranalli, G., *Rheology of the Earth, 2nd Edition*, Chapman & Hall, 1995.

Ranero, C., J. P. Morgan, K. McIntosh, and C. Reichert, Bending-related faulting and mantle serpentinization at the Middle America trench, *Nature*, *425*, 367–373, 2003.

Ratcliff, J. T., G. Schubert, and A. Zebib, Steady tetrahedral and cubic patterns of spherical-shell convection with temperature-dependent viscosity, *Journal of Geophysical Research*, *101*, 25,473–25,484, 1996.

Ribe, N. M., The dynamics of thin shells with variable viscosity and the origin of toroidal flow in the mantle, *Geophysical Journal International*, *110*, 532–552, 1992.

Ricard, Y., C. Doglioni, and R. Sabadini, Differential rotation between lithosphere and mantle: A consequence of lateral mantle viscosity variations, *Journal of Geophysical Research*, *96*, 8407–8415, 1991.

Richards, M. A., and C. Lithgow-Bertelloni, Plate motion changes, the Hawaiian-Emperor bend, and the apparent success adn failure of geodynamic models, *Earth and Planetary Science Letters*, *137*, 19–27, 1996.

Ritsema, J., H. van Heijst, and J. Woodhouse, Global transition zone tomography, *Journal of Geophysical Research*, *109*, B02,302, doi:10.1029/2003JB002610, 2004.

Ruff, L. J., Dynamic Stress Drop of Recent Earthquakes: Variations within Subduction Zones, *Pure and Applied Geophysics*, *154*, 409–431, 1999.

Schellart, W. P., Kinematics of subduction and subduction-induced flow in the upper mantle, *Journal of Geophysical Research*, *109*, doi: 10.1029/2004JB002970, 2004.

Schmandt, B., and E. Humphreys, Complex subduction and small-scale convection revealed by body-wave tomography of the western United States upper mantle, *Earth and Planetary Science Letters*, *297*, 435–445, doi:10.1016/j.epsl.2010.06.047, 2010.

Schubert, G., D. L. Turcotte, and P. Olson, *Mantle Convection in the Earth and Planets*, Cambridge University Press, 2001.

Seton, M., et al., Global continental and ocean basin reconstructions since 200 Ma, *Earth Science Reviews*, in press, 2012.

Sharp, W. D., and D. A. Clague, 50-Ma initiation of Hawaiian-Emperor Bend records major change in Pacific plate motion, *Science*, *313*, 1281–1284, doi:10.1126/science.1128489, 2006.

Spasojevic, S., M. Gurnis, and R. Sutherland, Mantle upwellings above slab graveyards linked to the global geoid lows, *Nature Geoscience*, *3*(6), 435–438, doi:10.1038/NGEO855, 2010.

Stadler, G., M. Gurnis, C. Burstedde, L. C. Wilcox, L. Alisic, and O. Ghattas, The dynamics of plate tectonics and mantle flow: From local to global scales, *Science*, *329*, 1033–1038, doi:10.1126/science.1191223, 2010.

Stegman, D. R., J. Freeman, W. Schellart, L. Moresi, and D. May, Influence of trench width on subduction hinge retreat rates in 3-d models of slab rollback, *Geochemistry, Geophysics, Geosystems*, *7*(3), Q03,012, doi:10.1029/2005GC001056, 2006.

Steinberger, B., and T. H. Torsvik, Toward an explanation for the present and past locations of the poles, *Geochemistry, Geophysics, Geosystems*, *11*(6), Q06W06, doi:10.1029/2009GC002889, 2010.

Steinberger, B., R. Sutherland, and R. J. O'Connell, Prediction of Emperor-Hawaii seamount locations from a revised model of global plate motion and mantle flow, *Nature*, *430*, 167–173, 2004.

Stemmer, K., H. Harder, and U. Hansen, A new method to simulate convection with strongly temperature-dependent and pressure-dependent viscosity in a spherical shell: Applications to the Earth's mantle, *Physics of the Earth and Planetary Interiors*, *157*, 223–249, 1996.

Stern, R. J., and S. H. Bloomer, Subduction zone infancy: Examples from the Eocene Izu-Bonin-Mariana and Jurassic California arcs, *Geological Society of America Bulletin*, *104*, 1621–1636, 1992.

Stoddard, P. R., and D. Abbott, Influence of the tectosphere upon plate motion, *Journal of Geophysical Research*, *101*, 5425–5434, 1996.

Sun, S., and M. F. Wheeler, Mesh adaptation strategies for discontinuous galerkin methods applied to reactive transport problems, in *Proceedings of the International Conference on Computing, Communication and Control Technologies*, edited by H.-W. Chu, M. Savoie, and B. Sanchez, pp. 223–228, 2004.

Sundar, H., R. Sampath, and G. Biros, Bottom-up construction and 2:1 balance refinement of linear octrees in parallel, *SIAM Journal on Scientific Computing*, *30*(5), 2675–2708, 2008.

Tan, E., E. Choi, P. Thoutireddy, M. Gurnis, and M. Aivazis, Geoframework: Coupling multiple models of mantle convection within a computational framework, *Geochemistry, Geophysics, Geosystems*, *7*(Q06001), 2006.

Tarduno, J., H. P. Bunge, N. Sleep, and U. Hansen, The Emperor seamounts: Southward motion of the Hawaiian hotspot plume in Earth's mantle, *Science*, *301*, 1064–1069, doi:10.1126/science.1086442, 2003.

Tarduno, J., H. P. Bunge, N. Sleep, and U. Hansen, The bent Hawaiian-Emperor hotspot track: Inheriting the mantle wind, *Science*, *324*, 50–53, doi:10.1126/science.1161256, 2009.

The Hypre Team, *hypre. High Performance Preconditioners, User's Manual*, Center for Applied Scientific Computing, Lawrence Livermore National Laboratory, 2007.

Torsvik, T. H., B. Steinberger, M. Gurnis, and C. Gaina, Plate tectonics and net lithosphere rotation over the past 150 My, *Earth and Planetary Science Letters*, *291*, 106–112, doi:10.1016/j.epsl.2009.12.055, 2010.

Tu, T., D. R. O'Hallaron, and O. Ghattas, Scalable parallel octree meshing for terascale applications, in *SC '05: Proceedings of the International Conference for High Performance Computing, Networking, Storage, and Analysis*, ACM/IEEE, doi:10.1109/SC.2005.61, 2005.

Uyeda, S., and H. Kanamori, Back-arc opening and the mode of subduction, *Journal of Geophysical Research*, *84*, 1049–1061, 1979.

van der Meer, D. G., W. Spakman, D. J. J. van Hinsbergen, M. L. Amaru, and T. H. Torsvik,

Towards absolute plate motions constrained by lower-mantle slab remnants, *Nature Geoscience*, *3*, 36–40, doi:10.1038/NGEO708, 2009.

van Hinsbergen, D. J. J., B. Steinberger, P. V. Doubrovine, and R. Gassmöller, Acceleration and deceleration of India-Asia convergence since the Cretaceous: Roles of mantle plumes and continental collision, *Journal of Geophysical Research*, *116*, B06,101, doi:10.1029/2010JB008051, 2011.

van Keken, P. E., B. Kiefer, and S. M. Peacock, High-resolution models of subduction zones: Implications for mineral dehydration reactions and the transport of water into the deep mantle, *Geochemistry, Geophysics, Geosystems*, *3*, 1056, 2002.

Vassiliou, M. S., and B. H. Hager, Subduction zone earthquakes and stress in slabs, *Pure and Applied Geophysics*, *128*(3–4), 547–624, 1988.

Vassiliou, M. S., B. H. Hager, and A. Raefsky, The distribution of earthquakes with depth and stress in subducting slabs, *Journal of Geodynamics*, *1*, 11–28, 1984.

Venkataraman, A., and H. Kanamori, Observational constraints on the fracture energy of subduction zone earthquakes, *Journal of Geophysical Research*, *109*, B05,302, doi:10.1029/2003JB002549, 2004.

Wang, S., and R. Wang, Current plate velocities relative to hotspots: Implications for hotspot motion, mantle viscosity and global reference frame, *Earth and Planetary Science Letters*, *189*, 133–140, 2001.

Wessel, P., and W. H. F. Smith, Free software helps map and display data, *EOS Transactions of the American Geophysical Union*, *72*, 441, 1991.

Wessel, P., Y. Harada, and L. W. Kroenke, Toward a self-consistent, high-resolution absolute plate motion model for the Pacific, *Geochemistry, Geophysics, Geosystems*, *7*(3), Q03L12, doi:10.1029/2005GC001000, 2006.

Whittaker, J. M., R. D. Müller, G. Leitchenkov, H. Stagg, M. Sdrolias, C. Gaina, and A. Goncharov, Major Australian-Antarctic plate reorganization at Hawaiian-Emperor Bend time, *Science*, *318*, 83–86, doi:10.1126/science.1143769, 2007.

Wiens, D. A., and J. J. McGuire, The 1994 Bolivia and Tonga Events - Fundamentally Different Types of Deep Earthquakes, *Geophysical Research Letters*, *22*(16), 2245–2248, 1995.

Wiens, D. A., and G. P. Smith, Seismological constraints on structure and flow patterns within the mantle wedge., in *Inside the Subduction Factory*, edited by J. Eiler, American Geophysical Union, 2003.

Wu, B., C. P. Conrad, A. Heuret, C. Lithgow-Bertelloni, and S. Lallemand, Reconciling strong slab pull and weak plate bending: The plate motion constraint on the strength of mantle slabs, *Earth and Planetary Science Letters*, *272*(1-2), 412–421, doi:10.1016/j.epsl.2008.05.009, 2008.

Yoshida, M., and A. Kageyama, Application of the Yin-Yang grid to a thermal convection of a Boussinesq fluid with infinite Prandtl number in a three-dimensional spherical shell, *Geophysical Research Letters*, *31*, L12,609, 2004.

Zhong, S., Role of ocean-continent contrast and continental keels on plate motion, net rotation of lithosphere, and the geoid, *Journal of Geophysical Research*, *106*, 703–712, 2001.

Zhong, S., and M. Gurnis, Towards a realistic simulation of plate margins in mantle convection, *Geophysical Research Letters*, *22*(5), 981–984, 1995.

Zhong, S., M. Gurnis, and G. Hulbert, Accurate determination of surface normal stress in viscous flow from a consistent boundary flux method, *Physics of the Earth and Planetary Interiors*, *78*, 1–8, 1993.

Zhong, S., M. Gurnis, and L. Moresi, Role of faults, nonlinear rheology, and viscosity structure in generating plates from instantaneous mantle flow models, *Journal of Geophysical Research*, *103*(B7), 15,255–15,268, 1998.

Zhong, S., M. T. Zuber, L. Moresi, and M. Gurnis, Role of temperature-dependent viscosity and surface plates in spherical shell models of mantle convection, *Journal of Geophysical Research*, *105*(B5), 11,063–11,082, doi:10.1029/2000JB900003, 2000.

Zhong, S., A. McNamara, E. Tan, L. Moresi, and M. Gurnis, A benchmark study on mantle convection in a 3-D spherical shell using CitcomS, *Geochemistry, Geophysics, Geosystems*, *9*, Q10,017, doi:10.1029/2008GC002048, 2008.